RAFAEL CARVALHO FIGUEIREDO

Ultrafast Electro-Optical Switching of Semiconductor Optical Amplifiers: Modeling and Experiments

CHAVEAMENTO ELETRO-ÓPTICO ULTRARRÁPIDO DE AMPLIFICADORES ÓPTICOS A SEMICONDUTOR: MODELAGEM E EXPERIMENTOS

Campinas

2015

UNIVERSIDADE ESTADUAL DE CAMPINAS

Faculdade de Engenharia Elétrica e de Computação

RAFAEL CARVALHO FIGUEIREDO

Ultrafast Electro-Optical Switching of Semiconductor Optical Amplifiers: Modeling and Experiments

CHAVEAMENTO ELETRO-ÓPTICO ULTRARRÁPIDO DE AMPLIFICADORES ÓPTICOS A SEMICONDUTOR: MODELAGEM E EXPERIMENTOS

Thesis presented to the School of Electrical and Computer Engineering of the University of Campinas in partial fulfillment of the requirements for the degree of Doctor in Electrical Engineering, in the area of Telecommunications and Telematics.

Tese apresentada à Faculdade de Engenharia Elétrica e de Computação da Universidade Estadual de Campinas como parte dos requisitos exigidos para a obtenção do título de Doutor em Engenharia Elétrica, na área de Telecomunicações e Telemática.

Advisor/*Orientador*: **Prof. Dr. Evandro Conforti**

Este exemplar corresponde à versão final da tese defendida pelo aluno Rafael Carvalho Figueiredo e orientada pelo Prof. Dr. Evandro Conforti.

Campinas

2015

Ficha catalográfica
Universidade Estadual de Campinas
Biblioteca da Área de Engenharia e Arquitetura
Luciana Pietrosanto Milla - CRB 8/8129

F469u

Figueiredo, Rafael Carvalho, 1982-
Ultrafast electro-optical switching of semiconductor optical amplifiers : modeling and experiments / Rafael Carvalho Figueiredo. – Campinas, SP : [s.n.], 2015.

Orientador: Evandro Conforti.
Tese (doutorado) – Universidade Estadual de Campinas, Faculdade de Engenharia Elétrica e de Computação.

1. Comunicações óticas. 2. Amplificadores óticos. 3. Chaveamento ótico. 4. Dispositivos optoeletrônicos. 5. Simulação computacional. I. Conforti, Evandro,1947-. II. Universidade Estadual de Campinas. Faculdade de Engenharia Elétrica e de Computação. III. Título.

Informações para Biblioteca Digital

Título em outro idioma: Chaveamento eletro-óptico ultrarrápido de amplificadores ópticos a semicondutor : modelagem e experimentos
Palavras-chave em inglês:
Optical communications
Optical amplifiers
Optical switching
Optoelectronic devices
Computational simulation
Área de concentração: Telecomunicações e Telemática
Titulação: Doutor em Engenharia Elétrica
Banca examinadora:
Evandro Conforti [Orientador]
Adaildo Gomes D'Assunção
Marcos Tavares de Melo
Rui Fragassi Souza
Cristiano de Mello Gallep
Data de defesa: 26-01-2015
Programa de Pós-Graduação: Engenharia Elétrica

COMISSÃO JULGADORA - TESE DE DOUTORADO

Candidato: Rafael Carvalho Figueiredo

Data da Defesa: 26 de janeiro de 2015

Título da Tese: "Ultrafast Electro-Optical Switching of Semiconductor Optical Amplifiers: Modeling and Experiments (Chaveamento Eletro-Óptico Ultrarrápido de Amplificadores Ópticos a Semicondutor: Modelagem e Experimentos"

Prof. Dr. Evandro Conforti (Presidente): _____

Prof. Dr. Adaildo Gomes D´Assunção: _____

Prof. Dr. Marcos Tavares de Melo: _____

Prof. Dr. Rui Fragassi Souza: _____

Prof. Dr. Cristiano de Mello Gallep: _____

Abstract

The performance of electro-optical space switches based on semiconductor optical amplifiers (SOA), including experiments and simulations using different formats of the electrical current injection pulses, is presented. Four SOAs with distinct physical characteristics are analyzed according to their switching behavior. Then, to improve the SOAs' electro-optical response, a new Multi-Impulse Step Injected Current (MISIC) technique is presented, achieving ultrafast switching time (115 ps) with low overshoot (< 30 %) and high optical contrast (30 dB). The results obtained might enable SOA applications, for example, as electro-optical switches in Data Center Networks, reducing switching latency between nodes and compensating signal's splitting losses. Furthermore, the equivalent circuits for three different SOAs (one chip-on-carrier and two encapsulated) are proposed. The models are validated by comparisons involving numerical and experimental results, with good correspondence. The modeling is carried out using circuit analysis software, requiring small computational resources and enabling the inclusion of parasitic elements of SOA devices' chip and microwave mounts.

Key-words: electro-optical switching; equivalent electrical circuit; optical switch; parameter extraction; parasitic element.

Resumo

O desempenho de chaves eletro-ópticas baseadas em amplificadores ópticos a semicondutor (SOA), incluindo experimentos e simulações usando diferentes formatos de pulso na injeção de corrente elétrica, é apresentado. Quatro SOAs com características físicas distintas são analisados de acordo com seu comportamento de chaveamento. Em seguida, com o intuito de melhorar a resposta eletro-óptica dos SOAs, uma nova técnica de injeção de multi-impulso (MISIC – *Multi-Impulse Step Injected Current*) é apresentada, alcançando tempo de subida ultrarrápido (115 ps) com baixo *overshoot* (< 30 %) e alto contraste óptico (30 dB). Os resultados obtidos podem permitir aplicações usando SOAs, por exemplo, como chaves eletro-ópticas em redes de *Data Centers*, reduzindo a latência de chaveamento entre os nós e compensando perdas por divisões do sinal. Além disso, os circuitos equivalentes para três diferentes SOAs (dois encapsulados e um sem encapsulamento) são propostos. Os modelos são validados através de comparações dos resultados numéricos e experimentais, com boa concordância. A modelagem é realizada em programas de análise de circuitos, exigindo pouco recurso computacional e possibilitando a inclusão dos elementos parasitas das montagens de micro-ondas e dos *chips* dos dispositivos.

Palavras-chave: chave óptica, chaveamento eletro-óptico; circuito equivalente, extração de parâmetro, parasita elétrico.

Contents

To my beloved wife.

Acknowledgements

I would like to express my sincere and deepest gratitude:

To my advisor, Prof. Dr. Evandro Conforti, for their constant enlightening guidance throughout the course of this work;

To Dr. Napoleão S. Ribeiro, for his crucial help in all stages of this work;

To Prof. Dr. Cristiano M. Gallep, for his invaluable support since I was an undergraduate student;

To the committee members, for their helpful comments and suggestions;

To Dr. Marcelo Ribeiro, for his always patient help with the experimental setups;

To Prof. Dr. Adriano Toazza, for the software to automate some measurements;

To my friends of Lapcom and APOGEEU;

To my students of ST.210 at FT-Unicamp (from 2010 to 2013);

To the staff of CPG-FEEC and to the managers of CePOF/FOTONICOM for the bureaucratic and administrative support;

To the Brazilian Agencies CAPES (*Coordenação de Aperfeiçoamento de Pessoal de Nível Superior*), CNPq (*Conselho Nacional de Desenvolvimento Científico e Tecnológico*), and FAPESP (*Fundação de Amparo a Pesquisa do Estado de São Paulo*), for the financial support;

To my wife, for her patience, love, care, and encouragement;

To my family;

And most of all, to my mother, to whom I owe my life.

List of Figures

List of Tables

Acronyms

AC	Alternating Current
ADS	Advanced Design System
ASE	Amplified Spontaneous Emission
CIP	Centre for Integrated Photonics
CIP-NL	Non-Linear SOA from CIP (model *NL-OEC-1550*)
CIP-XN	Ultra Non-Linear SOA from CIP (model *XN-OEC-1550*)
CIP-COC	COC-SOA from CIP (*model NL-1550*)
COC	Chip-on-Carrier
CW	Continuous Wave
DC	Direct Current
DCN	Data Center Network
DH	Double Heterostructure
EC	Equivalent Circuit
EMBH	Etched Mesa-Buried Heterostructure
EO	Electro-Optical

FP	Fabry-Perot
I-bias	SOA Injected Bias Current
I-V	Current versus Voltage
InGaAsP	Indium Gallium Arsenide Phosphide
InP	Indium Phosphide
InPhenix	Linear SOA from InPhenix, Inc. (model *IPSAD-1503*)
LabVIEW	Laboratory Virtual Instrument Engineering Workbench
Laser	Light amplification by stimulated emission of radiation
LC	Inductor-Capacitor
MISIC	Multi-Impulse Step Injected Current
MIS	Metal-Insulator-Semiconductor
MQW	Multiple Quantum Well
O-E-O	Optical-Electrical-Optical
p-i-n	positive-intrinsic-negative
PISIC	Pre-Impulse Step Injected Current
p-n	positive-negative
RC	Resistor-Capacitor
RF	Radio Frequency
RW	Ridge Waveguide
SOA	Semiconductor Optical Amplifier

SPICE	Simulation Program with Integrated Circuit Emphasis
ToR	Top-of-the-Rack
TW	Travelling Wave
UK	United Kingdom
VCSEL	Vertical-Cavity Surface-Emitting Laser
VOA	Variable Optical Attenuator

Symbols

a	Differential gain constant.
A_{nr}	Non-radiative recombination coefficient.
B	Radiative recombination coefficient.
C	Auger recombination coefficient.
C_{c1}	SOA's chip effective capacitance.
C_{c2}	SOA's chip parasitic capacitance.
C_d	Diffusion capacitance.
C_J	Capacitance associated to the layer adjacent to the active region.
C_L	Dopant-dependent capacitance from the p-InP layer.
C_{m1}, C_{m2}, C_{m3}	Standoff shunt capacitances from SOA's mount.
C_N	Capacitance associated to the MIS layer.
C_P	Standoff shunt capacitance from package.
C_{ph}	Capacitance modeling photons' storage.
C_S	Total diffusion capacitance.
C_{sc}	Space-charge capacitance.

$C_{sc(0)}$	Space-charge capacitance at zero applied voltage.
C_t	Effective capacitance.
E_1	Fundamental energy level.
E_2	Higher energy level.
E_g	Band gap.
f_c	Cutoff frequency.
f_r	Relaxation oscillation resonance frequency.
G	Net optical gain.
g	Small gain variation around the steady-state value.
G_0	Gain steady-state value.
G_m	Net rate of stimulated emission of the mth mode.
G_N	Gain as a function of the carrier density.
G_S	Gain as a function of the photon density.
h	Planck's constant.
I	Injection current.
i	Injection current AC term.
I_0	Injection current steady-state (DC) term.
I_A	Current at the active region.
I_L	Leakage current.
I_{off}	Low value bias current.

I_{on}	High value bias current.
I_S	Heterojunction saturation current.
i_s	Stimulated emission current for small-signal model.
I_{scr}	Current source.
I_{spon}	Spontaneous recombination current.
I_{stim}	Stimulated recombination current.
I_{tA}	Active region threshold current.
I_{th}	Threshold bias current.
k	Boltzmann constant.
L_{c1}	SOA's chip parasitic inductance.
L_{m1}, L_{m2}, L_{m3}	Bond-wire inductances from SOA's mount.
L_P	Bondwire inductance from package.
L_s	Inductance modeling photons' storage.
N	Carrier density.
n	Small carrier variation around the steady-state value.
N_0	Steady-state value for carriers.
N_e	Carrier density at equilibrium.
N_{tr}	Transparency carrier density.
P_{off}	Low value output power.
P_{on}	High value output power.

q	Electron charge.
R_1	Effective resistance.
R_{c1}	SOA's chip total series resistance.
R_d	Diffusion resistance.
R_{in}	Current source internal resistance.
R_J	Resistance associated to the layer adjacent to the active region.
R_{m1}-COC	Resistor from CIP-COC mount.
R_{m1}-$Pack$	Resistor from packaged SOAs' mount.
R_{m2}	Loss resistance from SOA's mount.
R_P	Bondwire resistance from package.
R_{ph}	Resistance modeling photons' loss.
R_{s1}	Gain compression resistance.
R_{s2}	Spontaneous emission's coupling factor resistance.
R_S	Total series resistance.
R_{SP}	Resistance from the interface with the metallic contact.
R_{SS}	Resistance from the substrate below the active region.
S	Photon density.
s	Small photons variation around the steady-state value.
$s\prime$	Normalized photon density.
S_0	Steady-state value for photons.

S_A	SOA's amplified signal (at the input carrier wavelength).
S_C	Forward noise added to SOA's signal (due to ASE).
S_{in}	SOA's input power.
S_m	Photon density of the mth mode.
s_n	Normalization constant for photon density.
S_{out}	Optical output power from SOA.
T	Temperature.
t	Time.
t_{on}	Turn-on delay.
V	Active region volume.
v	Frequency.
V_a	External voltage applied at the junction.
v_a	Small voltage variation around the steady-state value.
V_{a0}	Steady-state value for the external voltage applied at the junction.
V_{bi}	Built-in potential.
v_g	Group velocity.
V_{pp}	Peak-to-peak voltage
w	Junction grading coefficient.
α	Active region volume multiplied by the electron charge.
α_{int}	Absorption loss.

α_m	Mirror loss.
β	Fraction of spontaneous emission.
β_m	Fraction of spontaneous emission coupled into the mth mode.
γ	Differential gain parameter multiplied by the group velocity.
Γ	Confinement factor.
Γ_N	Decay rate of carriers.
Γ_R	Decay rate of relaxation oscillations.
Γ_S	Decay rate of photons.
ε	Gain compression factor.
η	Diode ideality factor.
τ_1	Relaxation oscillations' time constant.
τ_n	Carrier lifetime.
τ_p	Photon lifetime.
ω	Angular frequency.
ω_r	Relaxation oscillation frequency.

Chapter 1

Introduction

Modern data centers are at fast growing pace due to the exponential increase of network traffic as a consequence of speedy raising number of web services and applications [1, 2]. Data Center Network (DCN) servers can be interconnected according to a fault tolerant flat tree topology network, where the servers are connected through a Top-of-the-Rack (ToR) switch and these ToRs are further interconnected by clusters and aggregate switches [3]. The switching is there performed by electronic packet switches, at each level of the tree topology. In such topology, the flattening of the inter-cluster DCN can be implemented by photonics technologies, enabling optically transparent switching and interconnection, avoiding so the costly, high speed O-E-O (optical-electrical-optical) conversions and the electronic buffers.

One problem to be solved is the ToR switching latency between the nodes, which impacts the completion time in some applications. The semiconductor optical amplifier (SOA) can be a useful device to reduce this latency, since an N×N SOA switch can establish connections between ports in nanoseconds [4, 5]. Recently, an optical flat DCN based on scalable optical switch system with optical flow control, employing SOAs in 1×N switches, achieved an average latency less than 500 ns and an overall power consumption of 37.25 pJ/bit [6]. In addition, the amplification introduced by the SOA switch was used to compensate the splitting losses of the broadcast stage [7].

The overall DCN latency depends of many factors, such as link length, the control architecture, the packet guard times, and the optical flow control. However, the reduction of the SOA electro-optical (EO) switching time could further reduce the DCN latency [8].

The reduction of transit times in EO switches based on pre-distorted control signals was tested first for boosting the speed of laser-based switches [9]. Regarding the SOA – basically a laser with non-reflective edges – similar pre-distortion technique was first called "Pre-Impulse Step Injected Current", PISIC [8]. Such technique was later improved to achieve optical contrast above 25 dB, with *off-on* SOA switching time reduction from 2000 ps to 650 ps [10]. Spurious output power fluctuations that are inherent to the process and its minimization, with improved switching times, were analyzed further in [11]. In addition, this technique could also be applied to improve direct modulation of vertical-cavity surface-emitting lasers (VCSEL), which are widely used in optical interconnects [12].

In this context, this thesis presents experimental results of EO switching for diverse SOAs. Performances of four different devices are compared and possible influences from physical characteristics on switching speed are analyzed. Results show rise times ranging from 100 ps to 460 ps, overshoots from 7% to 480%, and optical contrasts from 1 dB to 17 dB. Also, electrical driven signal formats are evaluated in terms of switching time and spurious amplitude overshoots. The performed analyses might be useful in selecting the best devices for a particular application, and also to propose improvements in SOAs' fabrication, reducing parasitic elements from the package wires. After, a new technique employing Multi-Impulse Step Injected Current (MISIC) is presented to reduce the output power overshoots [11] and so avoid deterioration in switching windows. Using this technique, switching times below 115 ps were achieved with optical contrast around 30 dB and overall optical overshoot reduction of 50%.

Beyond the switching time reduction, the ongoing growth of SOA applications accentuates the importance of SOA steady-state and dynamic operations investigation. Such analysis can be performed analytically [13], numerically [14–17], by modeling the equivalent circuit [18–20], or even by combining such methods [21]. Analysis using equivalent circuit models

can be easily run via SPICE-based software requiring low computational resources. Furthermore, this approach enables parasitic elements' cascading and parameters' optimization, even giving indications for further improvement of devices fabrication.

Therefore, this thesis also proposes the equivalent electrical circuit modeling for three different SOAs. The model includes main parasitic leaks and it is validated comparing simulated results with experimental data, showing good agreement both in frequency and time domains. In previous works, relying on models developed by other authors for diode lasers [22–25], we proposed an equivalent electrical circuit modeling for a 2 mm-long chip-on-carrier (COC) SOA, (*CIP Technologies*, UK), called *CIP-COC* [26]. Later, the model was extended for two hermetically encapsulated SOAs [27]: the standard butterfly encapsulated version of the mentioned *CIP-COC* (model *NL-OEC-1550*), called *CIP-NL*, and a 650 μm long cavity device (*InPhenix Inc.*, model *IPSAD-1503*), called *InPhenix*. Improved extensions of the equivalent electrical circuits for those three travelling-wave (TW) SOAs are obtained in this thesis, including more precise tuning for circuit's parameters, based on experimental measurements of EO response. The new modeling enables more accurate analysis of the intrinsic parasitic leakages, due to the chip, mount, and encapsulation structures.

1.1 Objectives

This thesis consists of the study and analysis of electro-optical switches based on SOAs and, through experiments and modeling, it proposes possible improvements in the performance of this important application in optical networks. Initially, we test an optimum pulse format to switch the devices and we also analyze the influence of distinct SOAs characteristics in the performance of EO switching. Next we propose a new technique to improve the devices' switching, which achieved fast rise times, with high optical contrast and low overshoots. At last, we present an equivalent electrical circuit modeling for three different SOAs. Simulations employing the model might be used to study SOAs' behavior and to analyze possible improvements to

be implemented on those devices.

In summary, the main objective of this thesis is to achieve ultrafast electro-optical switching through two approaches: improvements on pulse formats to switch the SOAs and the design of a model that allows the simulation and study of SOAs in simple tools of circuits analysis.

1.2 Thesis structure

This first chapter presented the motivation and objectives of the work. The remaining of the thesis is organized as follows:

Chapter 2 presents the theoretical background for the major issues to be addressed in this thesis.

Chapter 3 presents details and results of the comparison performed with different SOAs employed as electro-optical switches.

Chapter 4 introduces a new technique to perform SOAs' switching: Multi-Impulse Step Injection Current (MISIC).

Chapter 5 presents the equivalent electrical circuit modeling for the SOAs and results obtained with the model.

Chapter 6 presents thesis conclusions and contributions, besides suggestions for future works.

Chapter 2

Theoretical Background

The semiconductor optical amplifier (SOA) is essentially a semiconductor laser with non-reflective coatings on its edges [28]. Thus, this chapter presents initially the theoretical background for semiconductor lasers, including the equivalent circuit modeling for those devices, followed by some considerations about SOAs.

2.1 Semiconductor Lasers

The semiconductor laser or laser diode may be briefly described as a medium responsible for the gain coupled to a resonant optical cavity. It is the most used optical source in current optical communications systems. Its advantages include wide operating range, narrow-linewidth and highly directional output, which allow an efficient light coupling to the optical fiber [29]. From this point on the semiconductor laser will be referred simply as laser, with properly indications when other types of lasers are mentioned.

2.1.1 Basic concepts

A simplified two-level atomic system is shown at Fig. 2.1 to illustrate the basic principle of light emission in lasers. E_1 represents the fundamental energy level and E_2 the higher energy

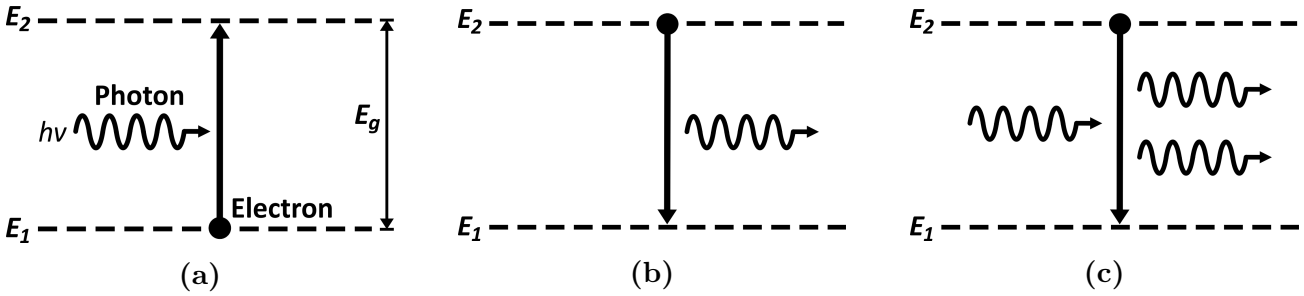

Figure 2.1: Fundamental processes in a two energy level system: (a) absorption, (b) spontaneous emission, and (c) stimulated emission.

level. The difference between the levels is called band gap (E_g): $E_g = E_2 - E_1$ [30].

In the electromagnetic energy absorption process, a photon (with energy = hv) from the incident light (with frequency v) is absorbed by the atom, raising the electron energy level from E_1 to E_2, and attenuating the incident light. In the spontaneous emission process, the electron – initially in higher energy excited state – returns to the level of lower energy, emitting a photon with random phase and spatial direction, i.e., generating incoherent radiation. In the stimulated emission, an incident photon stimulates the electron decay, resulting in an emitted photon with same energy, same phase and identical spatial direction of the incident photon. This stimulated coherent radiation is the fundamental process of light emission in lasers [30] and it was first formulated by Einstein approximately a century ago.

2.1.2 p-n junction

The p-n junction is the interface between a p-type and an n-type semiconductor material. Due to the different concentrations of carriers (electrons and holes) on the materials, they are unbalanced and their quasi-Fermi levels are misaligned. The balance is quickly established through the diffusion of carriers, i.e., electrons diffuse into the p region and holes into the n region. Such diffusion gives rise to the depletion region, where there are virtually no free carriers. The carriers diffusion remains until the equilibrium is reached by an electric field that appears in the opposite direction to the carriers flow, creating a barrier with built-in potential V_{bi} [31].

Applying an external voltage V_a to forward bias the junction, the built-in potential

barrier is reduced, allowing the drift of carriers across the junction. When the external source enables the population inversion – condition with more electron in high energy state than in lower state – the laser threshold condition is surpassed. Above threshold the stimulated emission overcomes spontaneous emission and absorption, amplifying the light at the p-n junction. However, in this type of junction, called homojunction, there is no confinement of carriers and high gain occurs in a small region. In addition, only the gain is not enough to the laser operation, which requires an optical feedback to turn the amplifier in an oscillator [30, 31]. Such problems could therefore be bypassed by changes in the device structure introduced in the early development of the laser, as detailed next.

2.1.3 Structures

In practice, lasers are not only constituted by the p-n junction: a thin layer of intrinsic material with smaller E_g is sandwiched between the p-type and n-type layers, forming a heterojunction. When forward biased, this double heterostructure (DH) confines carriers into the active region due to the band gap differences. This technique requires lower bias current and enables lasers to operate at room temperature. Furthermore, as a result of difference in refractive indices, the active region acts as a dielectric waveguide, where the number of optical modes can be controlled by the thickness of the active region [30, 31]. The development of such heterostructures, proposed in 1963, has made significant contributions in optoelectronics and high-speed applications, awarding the Nobel Prize for Physics to Zhores I. Alferov and Herbert Kroemer in 2000, along with Jack S. Kilby [32].

In telecommunications the active region should be thin enough ($\approx$0.2 μm) to support a single transverse mode. In broad-area lasers there is no light confinement in the lateral direction (parallel to the junction plane), diffusing the generated light by the entire width of the laser and making them unsuitable for optical communications. Such problem is solved by the gain-guided and index-guided lasers, which have mechanisms to lateral confinement of light. Gain-guided lasers (also know as stripe-geometry semiconductor lasers) solve the light-confinement problem

by limiting the injection of current to a narrow region, through the deposition of a dielectric over the p-layer with a central aperture to the electrical current injection, as illustrated at Fig. 2.2 (a) [30, 31].

In index-guided lasers, confinement is achieved by an index step at the lateral direction of the structure, forming a waveguide similar to the heterostructure formed in the transverse direction. These lasers are classified as weakly or strongly index-guided according to index step magnitude. An example of a weakly index-guided structure – ridge-waveguide (RW) laser – is shown in Fig. 2.2 (b). Figure 2.2 (c) shows an example of a strongly index-guided structure, in which the active region is buried on the device – know as etched-mesa buried heterostructure (EMBH) [30,31]. The tipical compound semiconductors used for emission in the spectral region of 1100 nm – 1650 nm are the Indium Phosphide (InP) and the Indium Gallium Arsenide Phosphide (InGaAsP) [25, 30, 31, 33, 34].

The equivalent circuit (EC) modeled in this work (detailed hereinafter) is based on an EC previously obtained for a strongly index-guided EMBH laser [24].

2.1.4 Rate equations

The laser rate equations describe the interaction between photons and electrons in an optical resonant cavity through the three fundamental processes describe before (see Fig. 2.1):

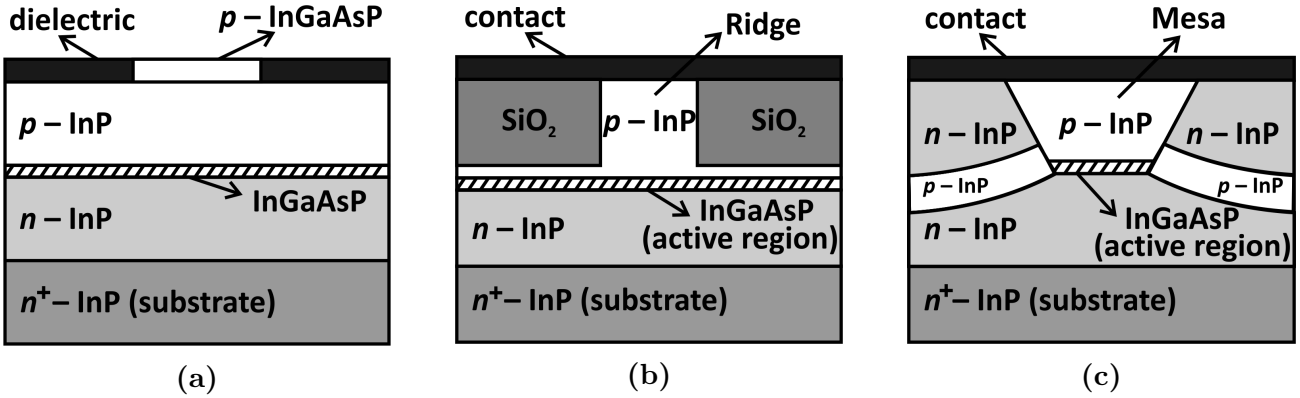

Figure 2.2: Cross sections of (a) gain-guided, (b) weakly index-guided, and (c) strongly index-guided semiconductor lasers structures (not to scale – redrawn from [30]).

absorption, spontaneous and stimulated emissions. The general multimode rate equations are given by [25]:

$$\frac{\partial S_m}{\partial t} = G_m S_m - \frac{S_m}{\tau_p} + \beta_m \frac{N}{\tau_n}, \tag{2.1}$$

$$\frac{\partial N}{\partial t} = \frac{I}{qV} - \frac{N}{\tau_n} - \sum_m G_m S_m, \tag{2.2}$$

where S_m is the photon density of the mth longitudinal mode; G_m is the net rate of stimulated emission of the mode; τ_p is the photon lifetime, whose decay rate is defined by $\tau_p = [v_g(\alpha_m + \alpha_{int})]^{-1}$, where v_g is the group velocity, α_m is the mirror loss, and α_{int} is the absorption loss; β_m is the fraction of spontaneous emission coupled into the mth mode; N is the carrier density; τ_n is the carrier lifetime; I is the injection current; q is the electron charge; and V is the active region volume. For a single-mode laser, the photon rate equation (Eq. 2.1) can be reduced to [25, 31]:

$$\frac{\partial S}{\partial t} = GS - \frac{S}{\tau_p} + \beta \frac{N}{\tau_n}. \tag{2.3}$$

At the transparency condition, the net optical gain (G) must compensate the losses due to photons leakage from cavity and other internal losses, i.e.:

$$G = \Gamma v_g a (N - N_{tr}), \tag{2.4}$$

where Γ is the optical confinement factor; a is differential gain constant; and N_{tr} is the carrier density at the transparency condition.

The carriers' rate equation for a single mode is reduced to:

$$\frac{\partial N}{\partial t} = \frac{I}{qV} - \frac{N}{\tau_n} - GS, \tag{2.5}$$

where the carriers lifetime is given by [31]:

$$\tau_n = \frac{1}{A_{nr} + BN + CN^2}, \tag{2.6}$$

where A_{nr} is the non-radiative recombination coefficient; B is the radiative recombination coefficient; and C is the Auger recombination coefficient, which is significant only at very high carrier density.

The rate equations will be addressed again in the equivalent circuit modeling, where many parameters are related to carriers' lifetime (Eq. (2.6)). Furthermore, some important characteristics of laser dynamics can be analyzed from the rate equations, namely the turn-on delay and the relaxation oscillations.

2.1.5 Transient response

If a laser is turned on by changing its injected current, the optical power response will be delayed by a time (t_{on}) and amplitude oscillations will occur at a certain decay rate before the steady state be reached [31, 35, 36]. This behavior is illustrated in Fig. 2.3 and detailed below.

Turn-on delay

When an injection current change from I_{off} to I_{on} (see Fig. 2.3), the photon density takes a time (t_{on}) to reach P_{on}. This delay time is determined by the carrier dynamics and can be calculated using the laser rate equations, considering whether the injection current I_{off} is below or above threshold (I_{th}) [35, 36].

Below I_{th} the carrier density N is smaller than the density at transparency (N_{tr}), yielding a net gaing G smaller than unity. Therefore, the photon density S is small and may be neglected in the carriers rate equation (Eq. (2.5)), yielding [36]:

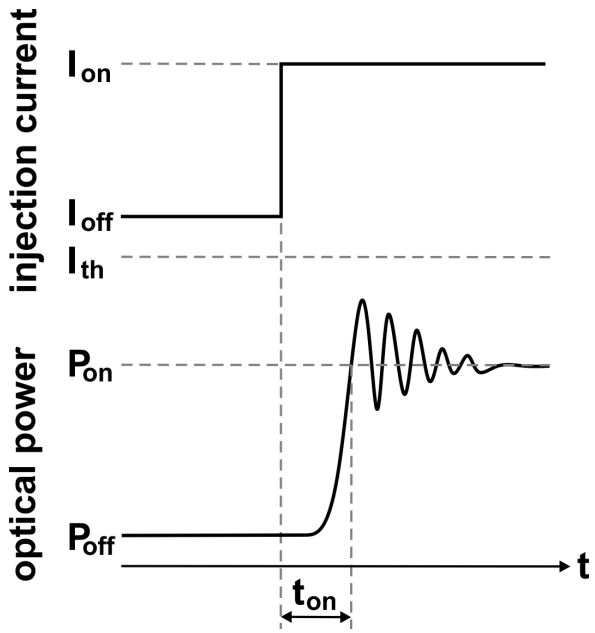

Figure 2.3: Optical output power for an ideal step-current pulse for a laser biased above threshold.

$$\frac{\partial N}{\partial t} = \frac{I - I_{th}}{qV} - \frac{N - N_{tr}}{\tau_n}, \qquad \text{for } N < N_{tr}. \tag{2.7}$$

If the current is switched on from I_{off} below I_{th} to I_{on}, a time different from zero elapses until the carrier density reach N_{tr}. This turn-on delay t_{on} is governed by the carrier lifetime τ_n and Eq. (2.7) yields [36]:

$$t_{on} = \tau_n \ln \frac{I_{on} - I_{off}}{I_{on} - I_{th}}, \qquad I_{off} < I_{th} < I_{on}. \tag{2.8}$$

Since τ_n is of the order of a few nanoseconds, the t_{on} of a laser biased below threshold have a similar order of magnitude, which is unacceptable for high bit rate transmission. Fortunately, this turn-on delay can be reduced to the order of picoseconds if the laser is biased above I_{th} [36].

Above threshold (as shown in Fig. 2.3), the photon density remains close to the bias level P_{off} and the carrier density remains close to N_{tr} within the time interval t_{on}. Then, the carrier recombination term can be neglected and the carrier rate equation (Eq. (2.5)) is

simplified to [36]:

$$\frac{\partial N}{\partial t} = \frac{I_{on} - I_{off}}{qV}, \qquad \text{for } 0 < t < t_{on}, \tag{2.9}$$

and it yields:

$$N - N_{tr} = \frac{I_{on} - I_{off}}{qV} t, \qquad 0 < t < t_{on}. \tag{2.10}$$

Now, for the photons rate equation (Eq. (2.3)), the small contribution from spontaneous emission shall be neglected. Then, considering the gain as a function of the carrier density, Eq. (2.3) can be simplified as [36]:

$$\frac{\partial S}{\partial t} = \frac{S}{\tau_p} \frac{\partial G}{\partial N} (N - N_{tr}), \qquad \text{for } 0 < t < t_{on}, \tag{2.11}$$

which, after insertion of Eq. (2.10), yields:

$$S = P_{off} \exp\left(\frac{\partial G}{\partial N} \frac{I_{on} - I_{off}}{qV} \frac{t^2}{2\tau_p} \right). \tag{2.12}$$

For $t = t_{on}$ the photon density $S = P_{on}$ is obtained yielding [36]:

$$t_{on} = \frac{\sqrt{2}}{\omega_r} \left[\ln\left(\frac{P_{on}}{P_{off}} \right) \right]^{1/2}, \tag{2.13}$$

where ω_r corresponds to the circular relaxation resonance frequency, to be detailed next.

Relaxation oscillations

As seen in Fig. 2.3, the laser output power presents damped periodic oscillations before level off. Those relaxations oscillations occur due to the energy exchanges between carrier and photons at the laser resonant cavity: an increasing in the carrier density raises the photon density above N_{tr} and the high number of photons increases the carrier consumption. Then,

the photon density decreases and the process repeats until the steady state be reached.

Considering linearized rate equations with small perturbations around a steady-state value, neglecting the quadratic and higher powers of these perturbations, assuming a dependence of G on the photon density S and a bias current above I_{tr}, the frequency of relaxation oscillations can be calculated as follow [31]:

$$\omega_r = \left[\left(G + G_S S_0\right) \left(G_N S_0\right) - \frac{\left(\Gamma_N - \Gamma_S\right)^2}{4} \right]^{1/2}, \tag{2.14}$$

where G_S is the gain as a function of the photon density; S_0 is steady-state value for photons; G_N is the gain as a function of the carrier density; Γ_N is the decay rate of carriers, given by $\Gamma_N = \tau_n^{-1} + G_N S_0$; and Γ_S is the decay rate of photons, given by $\Gamma_S = -G_S S_0$.

The decay rate of relaxation oscillations can then be calculated as [31]:

$$\Gamma_R = \frac{\left(\Gamma_N + \Gamma_S\right)}{2}. \tag{2.15}$$

Such relaxation oscillation is also observed in SOAs, but its physical origin is different: there is no laser cavity and resonance appears due to the waveguide internal loss – from waveguide scattering or free carrier absorption [37].

2.2 Lasers Equivalent Circuit Modeling

The laser dynamic behavior is fundamentally analyzed based on its rate equations. Such analysis can alternatively be accomplished through the equivalent electrical circuit modeling of the device, which allows the inclusion of gain compression and a precise examination of parasitic elements from device's chip and mount, among other advantages. This section depicts the laser equivalent circuit modeling, starting with the description of parasitic elements from EMBH lasers, including details of each circuit component, and closing with small-signal model for bias currents above and below the threshold. Such modeling is mainly based on previous work by

R. S. Tucker et al. [22–24, 35, 38–41].

2.2.1 Current-voltage characteristics

The current versus voltage properties (I-V) of a laser diode are expressed by the well-known Shockley equation [31]:

$$I = I_s \left[\exp\left(\frac{qV_{bi}}{\eta kT} \right) - 1 \right], \tag{2.16}$$

where I_s is the heterojunction saturation parameter (dependent on the diffusion coefficients related to the carriers); η is the diode ideality factor; k is the Boltzmann constant (1.38×10^{-23} J/K); and T is the temperature. For a light-emitting diode, the ideality factor η ranges between 1 and 2. The factor is equal to one for a ideal diode – when the electrical current is completely dominated by the diffusion mechanisms – and is equal to 2 when the generation and recombination mechanisms are dominant [42–44].

The carriers in a p-n junction are separated by a certain distance given by the depletion region, giving rise to a capacitance dependent on the voltage applied to the junction (V_a), called space charge capacitance (C_{sc}) and that can be expressed as [45]:

$$C_{sc} = C_{sc(0)} \left(1 - \frac{V_a}{V_{bi}} \right)^{-w}, \tag{2.17}$$

where $C_{sc(0)}$ is the space-charge capacitance at zero V_a, and w is the junction grading coefficient, which varies between 0.33 – for a linearly graded junction – and 0.5 – for an abrupt junction. Additionally, there is a diffusion capacitance (C_d) in parallel with C_{sc}, representing the capacitance from the minority carriers situated outside of the depletion region [45–47].

2.2.2 Electrical parasitic elements

In practice, there is a direct current (DC) leakage away from the laser active region, which can be represented by a shunt resistor. However, at high-speed modulation, there is shunt paths dependents on frequency and laser structures that cannot be described by a simple resistor [25]. Such electrical parasitics limit the extrinsic laser modulation bandwidth and are illustrated at Fig. 2.4, which shows the structural dependence of electrical parasitics in a cross-section of an EMBH laser (not to scale).

The resistance in series with the active region (R_{SP}) along with the resistance from substrate (R_{SS}) result in an intrinsic total series resistance $R_S = R_{SP}+R_{SS}$. At high frequencies, there are three main capacitive leakage that divert signal current away from the active region [24, 38]:

1. **MIS capacitance**: metal-insulator-semiconductor capacitance (C_N) distributed across the entire isolation layer of the chip in series with the C_L capacitance, forming the diffusion capacitance C_S.

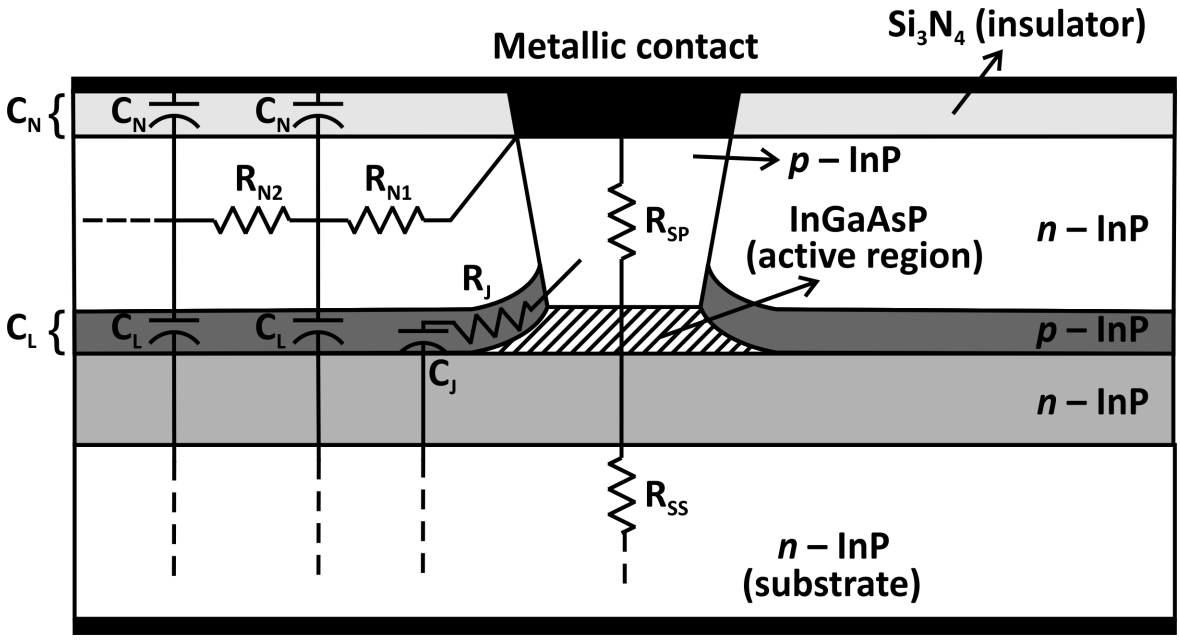

Figure 2.4: Cross-section of an EMBH laser highlighting its electrical parasitics (not to scale – redrawn from [24]).

2. **Reverse-biased capacitance**: A frequency-dependent leakage path in the n-InP region below the insulator, represented in Fig. 2.4 by a distributed RC network with coupling resistors R_{Ni}.

3. **Forward-biased capacitance**: Leakage path via the thin p-InP layer, represented by R_J and C_J, adjacent to the active region.

The principal factor limiting the laser bandwidth is the low-pass filter formed by the diffusion capacitance C_S and the series contact resistance R_S. The cutoff frequency is given by [25]:

$$f_c = \frac{1}{2\pi R_S C_S}. \tag{2.18}$$

Besides the intrinsic parasitic elements described above, there are also electrical parasitics from package, namely the standoff shunt capacitance (C_P), and the bondwire inductance (L_P) and resistance (R_P). Those elements are illustrated in Fig. 2.5, which also includes the electrical parasitics from chip (R_S and C_S), the space-charge capacitance (C_{sc}), the current source (I_{src}) and its internal resistance (R_{in}), the leakage current (I_L), and the current that effectively reaches the active region (I_A).

The next step is the active region modeling, which will be done for large and small signals, subdividing the latter case according to the bias current: above and below the threshold

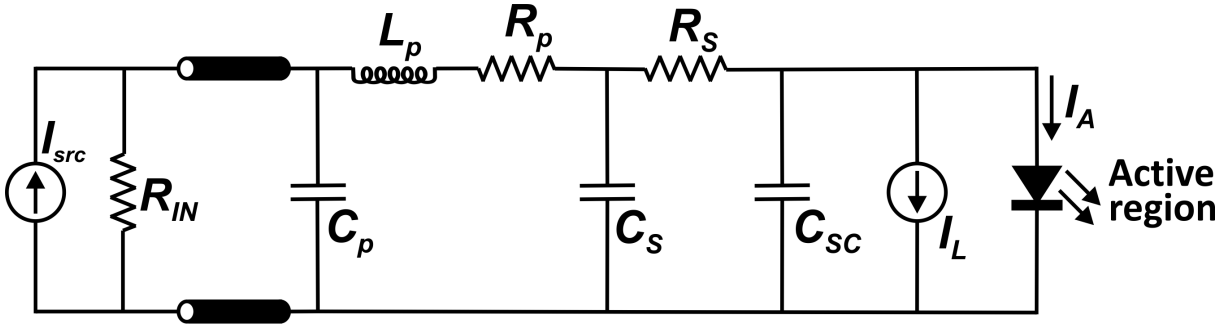

Figure 2.5: Equivalent electrical circuit including parasitic elements from package and chip (redrawn from [24, 25]).

value.

2.2.3 Large signal modeling

The large-signal equivalent circuit modeling is derived from the rate equations, translating laser's physical parameters (like photons and carriers) into electrical circuit parameters (like currents and voltages) [25]. The large signal model illustrated at Fig. 2.6, based on previous works by R. S. Tucker [24, 40], neglects high-level injection effects and is restricted to lasers biased close to or above I_{th}, condition in which the carriers density is almost constant.

The terms I_{spon} and I_{stim} model the spontaneous and the stimulated emissions at the active region, respectively. The term $s\prime$ represents the normalized photon density, given by [24]:

$$s\prime = \frac{s}{\Gamma s_n}, \tag{2.19}$$

where s_n is a normalization constant. The photon loss (R_{ph}) and the photon storage (C_{ph}) are expressed as [24]:

$$R_{ph} = \frac{\tau_p}{\alpha s_n}, \tag{2.20}$$

$$C_{ph} = \alpha s_n, \tag{2.21}$$

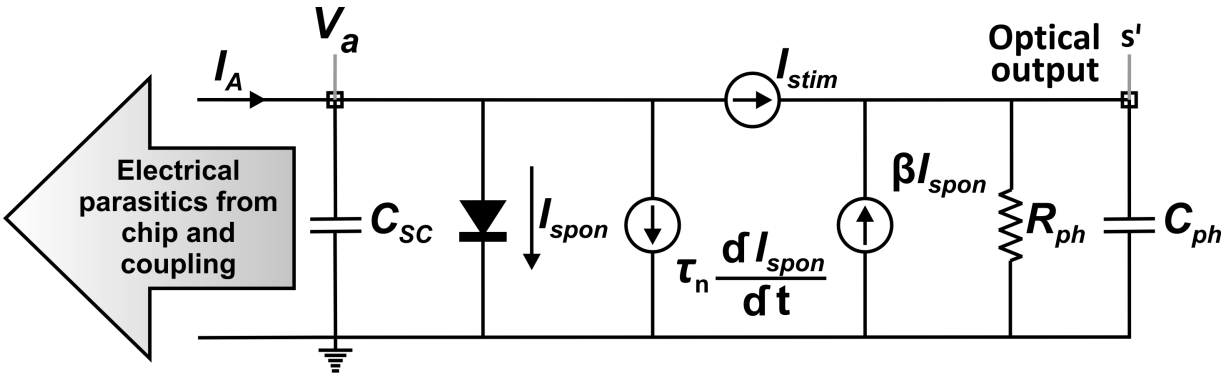

Figure 2.6: Laser large-signal circuit model (redrawn from [24, 25]).

where α is the electron charge multiplied by the active region volume (qV).

The output voltage ($s\prime$) is proportional to the large-signal light output intensity [24].

2.2.4 Small signal modeling

The small-signal model is obtained by linearizing the large-signal model and it is separated into models for below and above the electrical current threshold (I_{th}).

Below threshold model

The carrier rate equation below I_{th}, including the space-charge capacitance (C_{sc}), can be written as [25]:

$$\frac{\partial N}{\partial t} = \frac{I}{qV} - \frac{N}{\tau_n} - \frac{C_{sc}}{qV}\frac{\partial V_a}{\partial t}. \tag{2.22}$$

The small-signal model considers variations as perturbations around the steady-state value and the linearization is obtained by separating the time-dependent variables into DC and AC (alternating current) components. Then, taking the DC term I_0 and the small AC term i, we have:

$$\begin{aligned} I &= I_0 + ie^{j\omega t}, \\ N &= N_0 + ne^{j\omega t}, \\ V_a &= V_{a0} + v_a e^{j\omega t}, \end{aligned} \tag{2.23}$$

in which ω is the angular frequency. By substituting the terms of Eq. (2.23) into Eq. (2.22) a linearized expression can be written as:

$$i = \frac{n\alpha}{\tau_n} + j\omega\left(n\alpha + v_a C_{sc}\right). \tag{2.24}$$

The relationship between the carrier density and the voltage applied at the junction is obtained by using the Shockley equation [22]:

$$N = N_e \left[\exp\left(\frac{qV_a}{\eta kT} \right) - 1 \right], \tag{2.25}$$

where N_e is the carrier density at the equilibrium. Linearizing the relationship expressed at Eq. (2.25), we have:

$$n = \frac{v_a q N_0}{\eta kT}. \tag{2.26}$$

By substituting Eq. (2.26) into Eq. (2.24), the circuit equation is obtained:

$$i = v_a \left(\frac{1}{R_d} + j\omega \left(C_d + C_{sc} \right) \right). \tag{2.27}$$

The term C_{sc} is the space-charge capacitance expressed before at Eq. (2.17) and C_d is the diffusion capacitance of the active region, given by:

$$C_d = \frac{\tau_n}{R_d}. \tag{2.28}$$

The diffusion resistance of the heterojunction, R_d, can be derived from the Shockley's relationship:

$$\frac{\partial I}{\partial V_a} = \frac{I_s q}{\eta kT} \exp\left(\frac{qV_a}{\eta kT} \right). \tag{2.29}$$

Obtaining the differential resistor that represents the diode junction resistance, given by:

$$R_d = 1/\left(\frac{\partial I}{\partial V_a} \right) = \frac{\eta kT}{I_s q} \frac{1}{e^{\left(\frac{qV_a}{\eta kT} \right)}}. \tag{2.30}$$

Finally, the small-signal model (according to the circuit equation (2.24)) is illustrated at Fig. 2.7.

Above threshold model

Considering the space-charge capacitance C_{sc} and adding a term for the gain compression (ε) due to lateral diffusion of carriers, the carrier rate equations can be expressed as [23,25]:

$$\frac{\partial N}{\partial t} = \frac{I}{\alpha} - \frac{N}{\tau_n} - G\left(N\right)\left[1 - \varepsilon S\right] S - \frac{C_{sc}}{\alpha}\frac{\partial V_a}{\partial t}. \tag{2.31}$$

Similarly to the model below the threshold (see Eq. (2.23)), the variables are linearized by splitting them into DC and AC components:

$$\begin{aligned} S &= S_0 + s e^{j\omega t}, \\ G &= G_0 + g e^{j\omega t}. \end{aligned} \tag{2.32}$$

By substituting the small-signal values from Eq. (2.23) and Eq. (2.32) into the Eq.

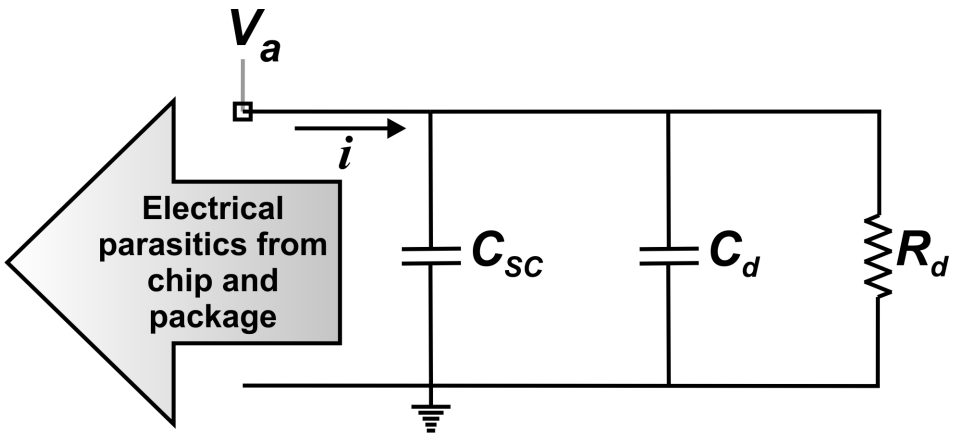

Figure 2.7: Active region small-signal circuit model for a laser operating below threshold (redrawn from [25]).

(2.31), we have:

$$\frac{\partial}{\partial t}\left(N_0 + ne^{j\omega t}\right) = \frac{\left(I_0 + ie^{j\omega t}\right)}{\alpha} - \frac{\left(N_0 + ne^{j\omega t}\right)}{\tau_n}$$
$$- \left(G_0 + ge^{j\omega t}\right)\left[1 - \varepsilon\left(S_0 + se^{j\omega t}\right)\right]\left(S_0 + se^{j\omega t}\right) - \frac{C_{sc}}{\alpha}\frac{\partial}{\partial t}\left(V_{a0} + v_a e^{j\omega t}\right). \quad (2.33)$$

Rearranging Eq. (2.33), we get:

$$j\omega n e^{j\omega t} = \left\{\frac{I_0}{\alpha} - \frac{N_0}{\tau_n} - \frac{C_{sc}}{\alpha}\frac{\partial V_{a0}}{\partial t} - G_0 S_0\left(1 - \varepsilon S_0\right)\right\} + \frac{ie^{j\omega t}}{\alpha} - \frac{ne^{j\omega t}}{\tau_n}$$
$$- \left(G_0 s e^{j\omega t} - 2\varepsilon S_0 G_0 s e^{j\omega t} + g S_0 e^{j\omega t} - \varepsilon g S_0^2 e^{j\omega t}\right) - \frac{C_{sc}}{\alpha} j\omega v_a e^{j\omega t}. \quad (2.34)$$

We assume that the DC steady-state terms inside the curly brackets in Eq. (2.34) satisfy:

$$\frac{\partial N_0}{\partial t} = \frac{I_0}{\alpha} - \frac{N_0}{\tau_n} - G\left(N_0\right)\left[1 - \varepsilon S_0\right] S_0 - \frac{C_{sc}}{\alpha}\frac{\partial V_{j0}}{\partial t} = 0. \quad (2.35)$$

By using Eq. (2.35), the Eq. (2.34) can then be reduced to:

$$\frac{i}{\alpha} = n\left(j\omega + \frac{1}{\tau_n}\right) + sG_0\left(1 - 2\varepsilon S_0\right) + \gamma n S_0\left(1 - \varepsilon S_0\right) + j\frac{C_{sc}}{\alpha}\omega v_a. \quad (2.36)$$

where γ is the differential gain parameter multiplied by the group velocity. Now, we consider that the term of stimulated emission current (i_s) includes the gain compression and it is approximately given by:

$$i_s = \left[\alpha G_0 s\left(1 - 2\varepsilon S_0\right)\right] \approx \alpha G_0 s, \quad (2.37)$$

and by substituting Eq. (2.26) into Eq. (2.36), we have:

$$i = \frac{\alpha v_a N_0 q}{\eta k T}\left(j\omega + \frac{1}{\tau_n}\right) + \gamma\frac{\alpha v_a N_0 q}{\eta k T} S_0\left(1 - \varepsilon S_0\right) + jC_{sc}\omega v_a + i_s. \quad (2.38)$$

By using the diffusion capacitance and resistance (see Eq. (2.28) and Eq. (2.30)), Eq. (2.38) can be rewritten as:

$$i = v_a \left[\left(\frac{1 + \tau_n \gamma \left(1 - \varepsilon S_0\right) S_0}{R_d} \right) + j\omega \left(C_d + C_{sc}\right) \right] + i_s. \tag{2.39}$$

Now we can define the effective capacitance C_t, given by the capacitance C_{sc} and C_d in parallel:

$$C_t = C_{sc} + C_d, \tag{2.40}$$

and the effective resistance R_1, given by:

$$R_1 = \frac{R_d}{1 + \tau_n \gamma \left(1 - \varepsilon S_0\right) S_0} \approx \frac{R_d}{1 + \tau_n \gamma S_0}. \tag{2.41}$$

Finally, the circuit equation for Eq. (2.31) can be expressed as:

$$i = v_a \left(\frac{1}{R_1} + j\omega C_t \right) + i_s, \tag{2.42}$$

which can be represented by the equivalent circuit (EC) illustrated at Fig. 2.8. At this point, the EC is practically equal to the model below threshold (see Fig. 2.7) converted into effective capacitance and resistance. This partial model corresponds only to the carrier dynamics above threshold, and now we proceed to the photons dynamics to conclude the small-signal model above threshold.

The photons' rate equation, including the gain compression term, is expressed by [23,25]:

$$\frac{\partial S}{\partial t} = GS\left(1 - \varepsilon S\right) - \frac{S}{\tau_p} + \beta \frac{N}{\tau_n}. \tag{2.43}$$

Proceeding in the same way as in the first part, the small-signal terms from Eq. (2.23)

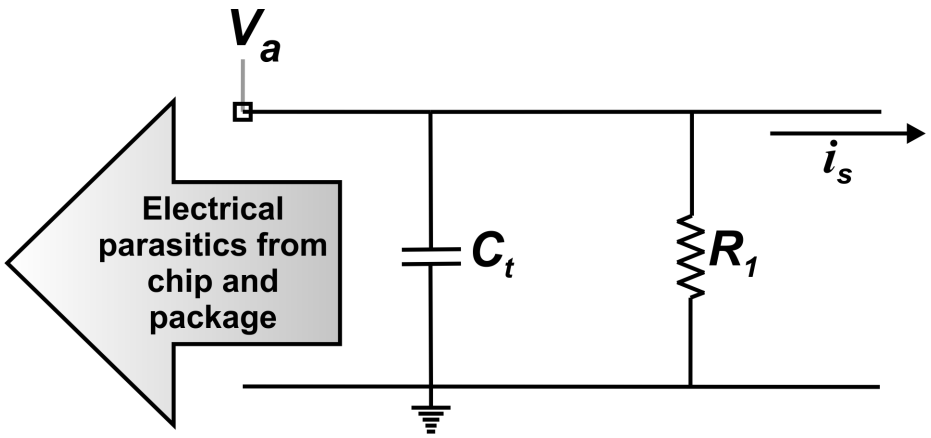

Figure 2.8: Partial small-signal circuit model related to the carriers dynamics for a laser operating above threshold (redrawn from [25]).

and Eq. (2.32) are replaced into Eq. (2.43) to obtain:

$$\frac{\partial}{\partial t}\left(S_0 + se^{j\omega t}\right) = \left(G_0 + ge^{j\omega t}\right)\left(S_0 + se^{j\omega t}\right)\left[1 - \varepsilon\left(S_0 + se^{j\omega t}\right)\right]$$
$$-\frac{\left(S_0 + se^{j\omega t}\right)}{\tau_p} + \beta\left(\frac{N_0 + ne^{j\omega t}}{\tau_n}\right). \tag{2.44}$$

By reorganizing Eq. (2.44), we get:

$$j\omega se^{j\omega t} = \left\{\left[G_0\left(1 - \varepsilon S_0\right) - \frac{1}{\tau_p}\right]S_0 + \beta\frac{N_0}{\tau_n}\right\} + gS_0e^{j\omega t}$$
$$+G_0se^{j\omega t} - g\varepsilon S_0^2e^{j\omega t} - 2\varepsilon G_0S_0se^{j\omega t} - \frac{se^{j\omega t}}{\tau_p} + \beta\frac{ne^{j\omega t}}{\tau_n}. \tag{2.45}$$

We assume once again that the DC steady-state terms inside the curly brackets in Eq. (2.45) satisfy:

$$\frac{\partial S_0}{\partial t} = \left[G_0\left(1 - \varepsilon S_0\right) - \frac{1}{\tau_p}\right]S_0 + \beta\frac{N_0}{\tau_n} = 0. \tag{2.46}$$

Eq. (2.45) can then be simplified into:

$$j\omega s = gS_0 + G_0s - g\varepsilon S_0^2 - \frac{s}{\tau_p} + \beta\frac{n}{\tau_n} - 2\varepsilon G_0S_0s. \tag{2.47}$$

By substituting Eq. (2.26) into Eq. (2.47), we have:

$$v_a \frac{N_0 q}{\eta \tau_n kT} \left[\beta + \gamma \tau_n S_0 \left(1 - \varepsilon S_0\right)\right] = \left(j\omega + 2\varepsilon S_0 G_0 - G_0 + \frac{1}{\tau_p}\right) s. \tag{2.48}$$

From the steady-state condition of Eq. (2.46), the following expression for photon lifetime is obtained:

$$\frac{1}{\tau_p} = \frac{\beta N_0}{S_0 \tau_n} - G_0 \varepsilon S_0 + G_0. \tag{2.49}$$

Now, by substituting Eq. (2.49) into Eq. (2.48), we get:

$$\begin{aligned} v_a \;\; = \;\; & \frac{\eta \tau_n kT}{N_0 q} \left(j\omega + 2\varepsilon G_0 S_0 - G_0 + \frac{\beta N_0}{S_0 \tau_n} - G_0 \varepsilon S_0 + G_0\right) \\ & \times \frac{s}{\left[\beta + \gamma \tau_n S_0 \left(1 - \varepsilon S_0\right)\right]}. \end{aligned} \tag{2.50}$$

Then, we arrive at:

$$v_a = \frac{R_d}{G_0 \left(1 - 2\varepsilon S_0\right) \left[\beta + \gamma \tau_n S_0 \left(1 - \varepsilon S_0\right)\right]} \left(j\omega + \varepsilon G_0 S_0 + \frac{\beta N_0}{S_0 \tau_n}\right) i_s. \tag{2.51}$$

Defining the circuit elements for Eq. (2.51) as [23, 25]:

$$\begin{aligned} L_s &= \frac{R_d}{G_0 \left(1 - 2\varepsilon S_0\right) \left[\beta + \gamma \tau_n S_0 \left(1 - \varepsilon S_0\right)\right]}, \\ R_{s1} &= \varepsilon G_0 S_0 L_s, \\ R_{s2} &= \frac{\beta N_0 L_s}{S_0 \tau_n}, \end{aligned} \tag{2.52}$$

we finally obtain the circuit equation given by:

$$v_a = \left(j\omega L_s + R_{s1} + R_{s2}\right) i_s. \tag{2.53}$$

The complete small-signal circuit model, comprising carrier and photon dynamics, is illustrated at Fig. 2.9. Regarding the physical meaning of the elements, the LC resonant circuit composed by the effective capacitance $(C_{sc}+C_d)$ and the inductance L_s models the laser oscillation relaxation, whose damping is modeled by the resistances: R_1 represents damping due to spontaneous and stimulated recombination; R_{s1} models the gain compression effect due to the diffusion of carriers; and R_{s2} provides the effect of spontaneous emission coupling factor β.

Approximations for circuit element expressions

Since, from Eq. (2.49), the following approximation can be applied:

$$\frac{1}{\tau_p} = \frac{\beta N_0}{S_0 \tau_n} - G_0 \varepsilon S_0 + G_0 \approx G_0, \tag{2.54}$$

and that carrier density is practically constant above threshold, the L_s inductor may be approximated by [24, 25]:

$$L_s = \frac{R_d}{G_0 \left(1 - 2\varepsilon S_0\right) \left[\beta + \gamma \tau_n S_0 \left(1 - \varepsilon S_0\right)\right]} \approx \frac{R_d \tau_p}{\gamma \tau_n S_0}. \tag{2.55}$$

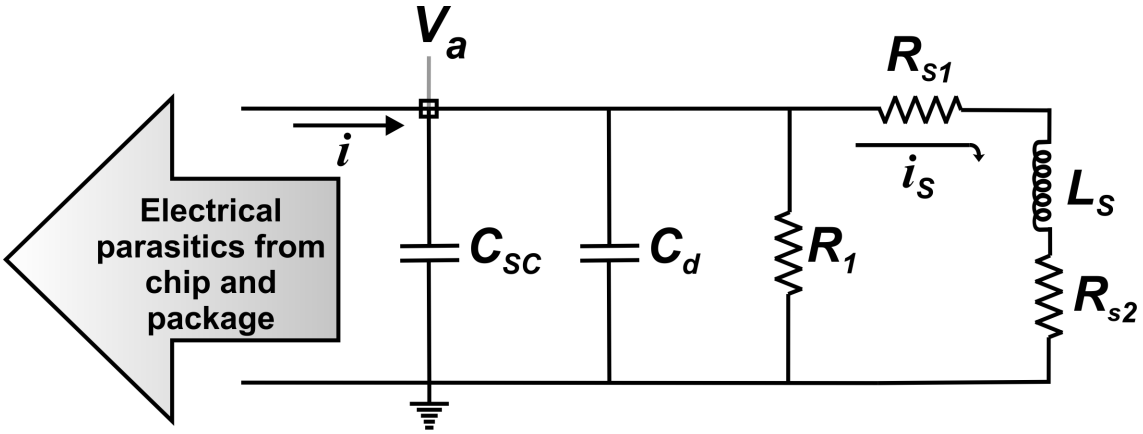

Figure 2.9: Complete small-signal circuit model for a laser operating above threshold (redrawn from [25]).

Then, by applying Eq. (2.55), the damping resistors can be expressed as:

$$R_{s1} = \varepsilon G_0 S_0 L_s \approx \frac{\varepsilon R_d}{\gamma \tau_n}, \tag{2.56}$$

$$R_{s2} = \frac{\beta N_0 L_s}{S_0 \tau_n} \approx \frac{\beta \Gamma R_d \tau_p I_{tA}}{\alpha \gamma \tau_n S_0^2}, \tag{2.57}$$

where I_{tA} is the active layer threshold current (internal current excluding the leakage current), given by [24]:

$$I_{tA} \approx \frac{\alpha \left(\dfrac{1}{\tau_p \Gamma \gamma} + N_{tr} \right)}{\tau_n}. \tag{2.58}$$

The photon density at steady-state can then be written as:

$$S_0 \approx \frac{\Gamma \tau_p}{\alpha} \left(I_0 - I_{th} \right), \tag{2.59}$$

where I_{th} is the total (external) threshold current, including the internal and the leakage current, i.e., $I_{th} = I_{tA} + I_L$.

Taking the above approximations into account, the relaxation oscillation resonance frequency (f_r) can be approximated by:

$$f_r = \frac{1}{2\pi} \left[L_s \left(C_d - C_{sc} \right) \right]^{-1/2}, \tag{2.60}$$

and the damping time constant (τ_1) related to the relaxation oscillations can be expressed as:

$$\tau_1 = \frac{L_s}{R_{s1} + R_{s2}}. \tag{2.61}$$

Given the devices' similarities [31], most of the theoretical considerations presented in this chapter for lasers also apply to SOAs. Then, as will be detailed later, the equivalent circuit obtained here for lasers will be properly adapted for SOAs and the simulated results compared

to experimental data.

2.3 Semiconductor Optical Amplifiers

The semiconductor optical amplifier (SOA) is an optoelectronic device able to amplify an input light signal. The optical amplification occurs at the SOA's active region, where an external source of electric current provides the energy that enables the gain to takes place – when the stimulated emissions overcome absorption and spontaneous emission. The SOA's basic principles and structures are similar to those presented before for semiconductor lasers, with a few fundamental differences, as detailed in this section [31, 48].

SOAs can be divided into two types [48]:

- **FP-SOA**: the Fabry-Perot (FP)-SOA has significant values of residual reflectivity at its edges, forming a resonant cavity that amplifies the signal via repeated passes through the active region;
- **TW-SOA**: the traveling wave (TW)-SOA has negligible reflections at its edges and the incident signal is amplified in a single-pass in the amplifier.

The residual reflectivity on TW-SOAs needs to be below 0.1%. To do this, anti-reflection coatings are used with additional mechanisms to decrease the reflectivity, such as the inclination of the active region or the use of transparent regions between the active region and the anti-reflective coatings. Compared to FP-SOA, the TW-SOA is less sensitive to fluctuations in bias current, temperature and signal polarization, making this latter more suitable to be used in optical communication networks [28, 48–50]. The SOAs used in this work are TW devices. Thus, from this point on, the TW-SOA will be referred simply as SOA, with properly indications when other types of SOAs are mentioned.

Still regarding the structures of SOAs used in this work, the devices are "black-box" like, i.e., manufacturers do not provide details of their semiconductor structure or fabrication

process. Thus, some of the parameters used in this thesis – that could not be measured or estimated – are based on values found in the literature, properly referenced.

2.3.1 SOA gain

The basic definition of the SOA intrinsic gain (G) is simply the ratio of the optical signal power at SOA's input facet (S_{in}) to the signal power at the output facet (S_{out}). This amplification factor is expressed by:

$$G = \frac{S_{out}}{S_{in}}. \tag{2.62}$$

The SOA gain is affected by its input signal power and also by the internal noise generated during the amplification process. The increase in power depletes the carriers in the active region, which leads to a decrease in the amplifier gain. In other words, the gain may be higher for low optical powers than for high optical powers. This gain saturation can cause signal distortion and it can also limit the gain when multichannels are applied to SOAs [48, 51].

Furthermore, the carrier density changes induced by the amplifier input signals are the major factor of SOAs nonlinearities. Generally, this nonlinear behavior cause problems such as frequency chirping and generation of inter-modulation products. Nevertheless, SOAs nonlinearities can be useful for functional applications, such as wavelength converter, logic gate, pulse generator, etc. [48].

The next subsection will explore a SOA functional application of great importance to today's high-speed optical networks, namely electro-optical switching based on SOAs. This application, which is not necessarily based on nonlinear behavior, is a fundamental object of study of this thesis.

2.3.2 Electro-optical switching based on SOA

Optical switches (or gates) based on SOAs can either be optically or electrically controlled and they meet desirable characteristics like fast switching speed, high contrast ratio, ability to be integrated and cascaded [48].

Several configurations for SOA switches are possible. The simplest one consists of a single SOA with the switch state electrically controlled: an electrical drive current set the amplifier gain, switching the device on/off – its operation is represented at Fig. 2.10,

The intrinsic SOA switching time is dependent on the carrier lifetime [48], which is not a constant value since it changes with the population density [25, 27]. Therefore, the PISIC technique – a single step combined to a narrow pre-impulse [8] – can be used to quickly increase the carrier population, decreasing the SOA's carrier lifetime and so achieving faster switching times. In this thesis results using the PISIC technique will be compared to a new technique (MISIC), which presents higher optical contrast ratios and smaller power overshoots, keeping fast switching times.

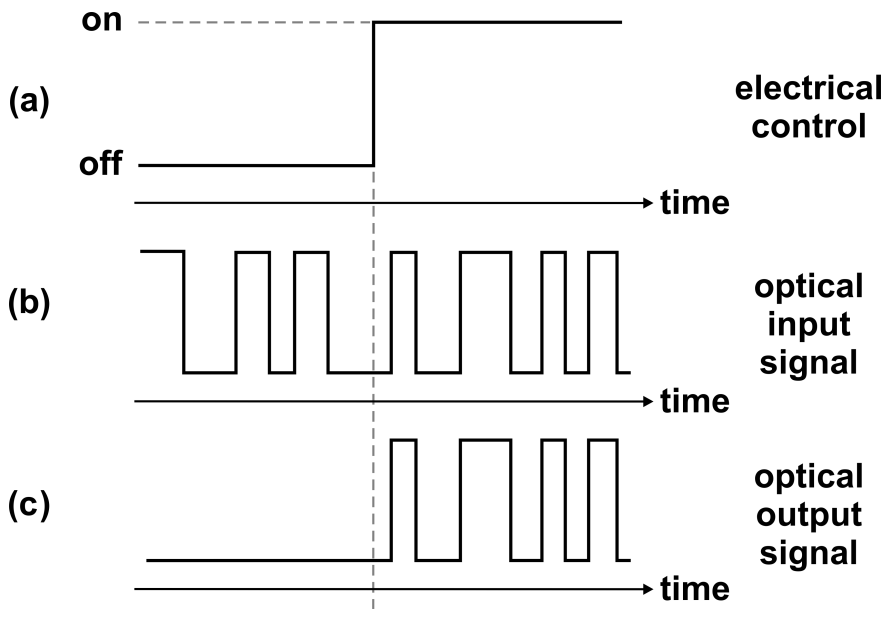

Figure 2.10: Operation of a basic electrically controlled SOA switch (adapted from [48]): an electrical bias current (a) sets the SOA's gain, and the optical input signal (b) resulting in a gated output (c).

2.3.3 Considerations about SOA circuit modeling

As stated before, the SOA is basically a semiconductor laser with non-reflective covers in the edges, so the equivalent electrical circuits modeling can be derived from previous models developed for EMBH lasers [22–24]. While for a semiconductor laser the optical output is mainly composed by stimulated emission – after the population inversion condition is satisfied – for a SOA the output is composed by the amplified signal at the input carrier wavelength (S_C) added to a forward noise (S_A), due the amplified spontaneous emission (ASE), as illustrated at Fig. 2.11.

The evolution in time of the average carrier density (N) inside the SOA active cavity, assuming N nearly uniform in the transverse direction, can be described as [52]:

$$\frac{\partial N}{\partial t} \simeq \frac{I}{qV} - \frac{N}{\tau_n} - GS, \tag{2.63}$$

where I is the injected current, q is the electron charge, V is the volume of the active region, τ_n is the charge carrier lifetime, $S = S_A + S_{in}$ is the total optical power, and the net optical gain G can be expressed as [52]:

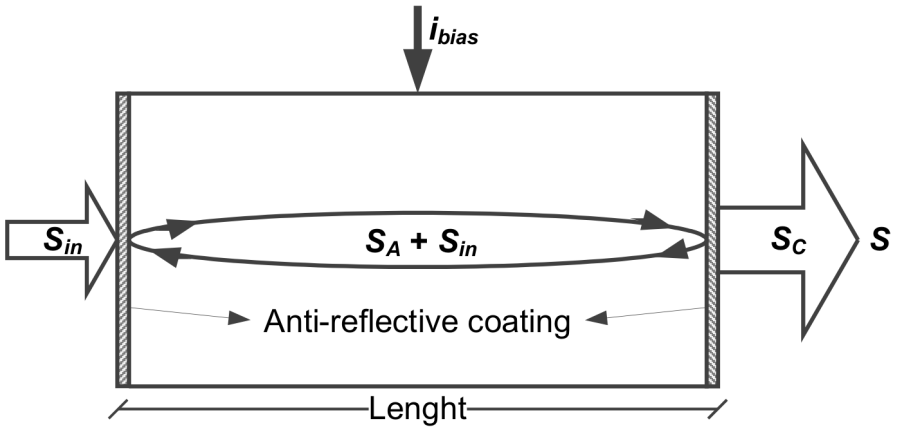

Figure 2.11: SOA simplified schematic model fed by bias current, with the optical signal components: input power (S_{in}), ASE noise (S_A) and output (S_C).

$$G = \gamma(N - N_{tr}), \tag{2.64}$$

where N_{tr} is the transparency carrier density.

The evolution of the optical signal can be described as $S_C = GS_{in}$, and the ASE noise (S_A) can be expressed as:

$$\frac{\partial S_A}{\partial t} \simeq GS_A - \frac{S_A}{\tau_p} + \beta\frac{N}{\tau_n}, \tag{2.65}$$

where τ_p is the photon lifetime and β is the fraction of spontaneous emission coupled into the guided mode. Therefore, the time evolution of the total optical signal intensity ($S = S_A + S_C$) is described as:

$$\frac{\partial S}{\partial t} \simeq G(S_A + S_{in}) - \frac{S_A}{\tau_p} + \beta\frac{N}{\tau_n}, \tag{2.66}$$

which, together with Eq. (2.63), are similar to the basic rate equations used for single-mode semiconductor lasers (see Eq. (2.3) and Eq. (2.5)). Therefore, previous models developed for semiconductor lasers [22–24] are adapted for SOAs, whose results will be described in Chapter 5.

Chapter 3

Comparative Switching

This chapter presents the comparative performance of electro-optical switching based on SOAs, using four devices with distinct physical features and different pulse formats for the current injection. Such analyses might be useful in selecting the best devices for a particular application, and also to propose improvements in SOAs' fabrication, reducing parasitic elements from the package wires, for instance. Furthermore, the experimental results obtained will be used for comparison with simulation results afterward. [1]

3.1 Material and methods

Initially, this section presents the description and characteristics of the SOAs used in this work. Next, the electro-optical switching measurement, results and discussion are presented.

[1] This chapter is based on the results presented in the following article:
R. C. Figueiredo, N. S. Ribeiro, C. M. Gallep, E. Conforti. "Comparison of Electro-Optical Switching Performances of Dissimilar Semiconductor Optical Amplifiers", accepted for publication in *Microw. Opt. Technol. Lett.*, 2015.

3.1.1 SOAs' descriptions

The four tested SOAs, one chip-on-carrier and three packaged devices, are listed below:

- InPhenix: model *IPSAD1503*, with cavity length of 650 μm, maximum drive current of 350 mA, saturation output power of 5 dBm, maximum gain of 16 dB;
- CIP-NL: non linear model *NL-OEC-1550*, cavity length of 2 mm, maximum drive current of 400 mA, saturation output power of 6 dBm, maximum gain of 34 dB;
- CIP-COC: the unpackaged (chip-on-carrier – COC) version of CIP-NL, i.e. the same SOA described above without its encapsulation.
- CIP-XN: ultra non-linear model *XN-OEC-1550*, cavity length of 2 mm, maximum drive current of 600 mA, saturation output power of 12 dBm, maximum gain of 25 dB.

Fig. 3.1 illustrates the CIP-NL and the encapsulated SOAs microwave connections inside the butterfly package are shown schematically (not to scale) in Fig. 3.2. Both butterfly pins enters the enclosure and are connected to the SOA using gold wires in a series of steps. Those steps of wires and metallic plates increase the parasitic inductances and capacitances when comparing with the CIP-COC mount. To provide a precise temperature control, a Peltier element is attached close to the SOA chip, also increasing parasitic. The microwave connection (not shown here) is provided by a 50 mm length of 0.085" diameter PTFE semi rigid coaxial cable in series with a 47 Ω, low inductance resistor and a 5 mm length strip line soldered to the butterfly outside pin (shortened to 2 mm). Therefore, both the butterfly internal connections and the external connections contribute to a higher parasitic for the encapsulated devices.

Reduction of electrical parasitics is achieved using a microstrip directly coupled to the CIP-COC, therefore excluding the standard butterfly encapsulation, as illustrated in Fig. 3.3. The COC mounting, shown in Fig. 3.4 (not to scale), uses a microstrip line (16 mm length with alumina substrate) connected in series to a low inductance 50 Ω resistor. The other resistor terminal is attached directly to a SOA chip-on-carrier constructed on silicon (10×2×1

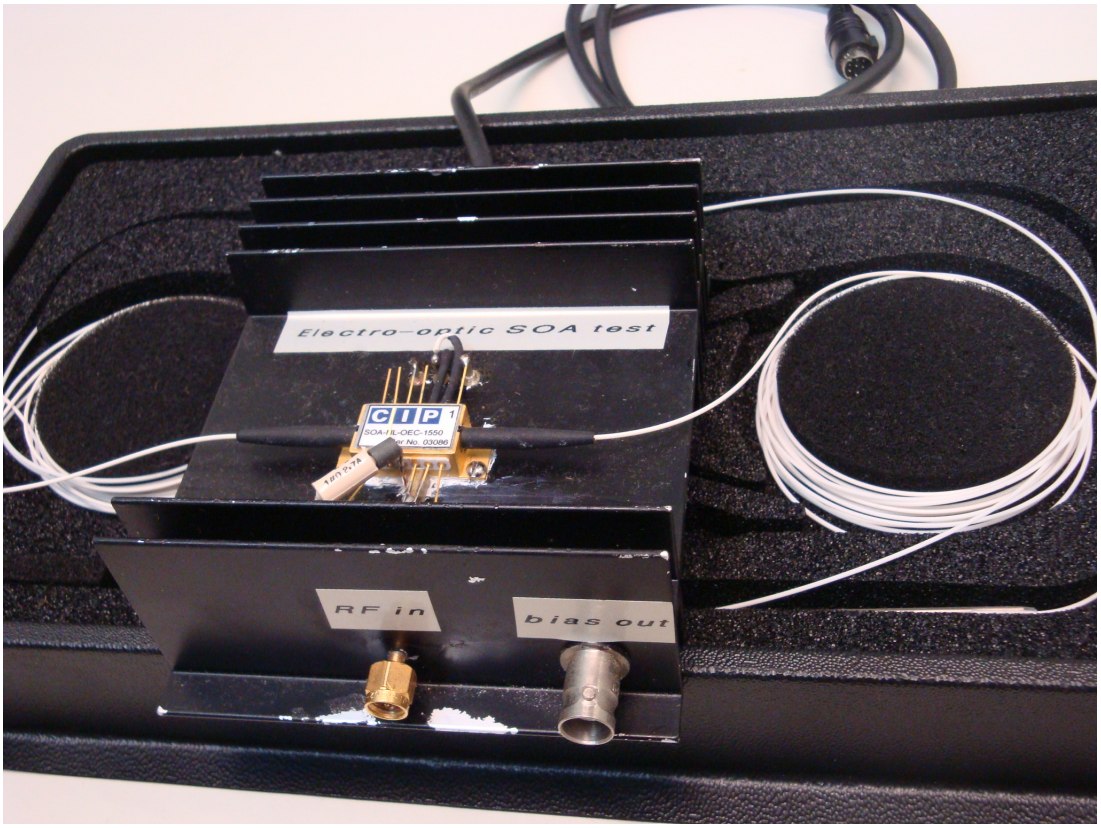

Figure 3.1: Picture of the CIP-NL SOA.

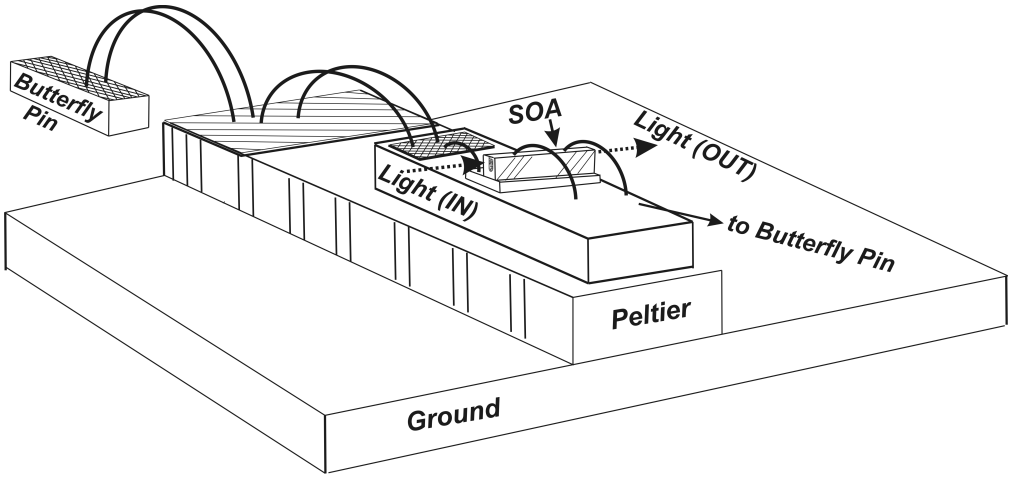

Figure 3.2: Schematic of packaged SOAs connections (not to scale).

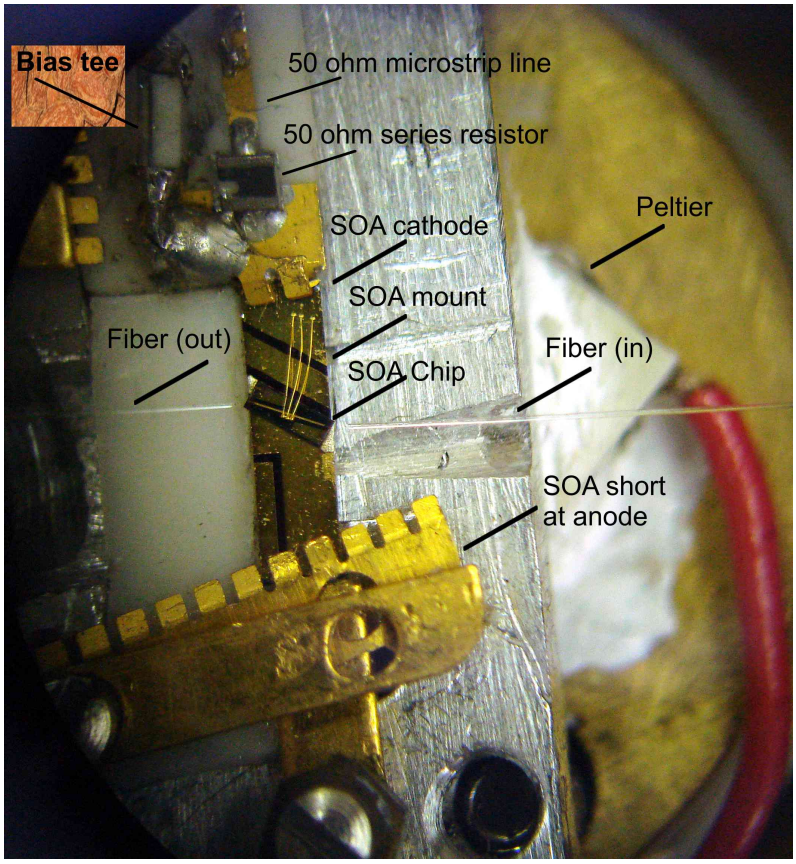

Figure 3.3: Picture of the CIP-COC.

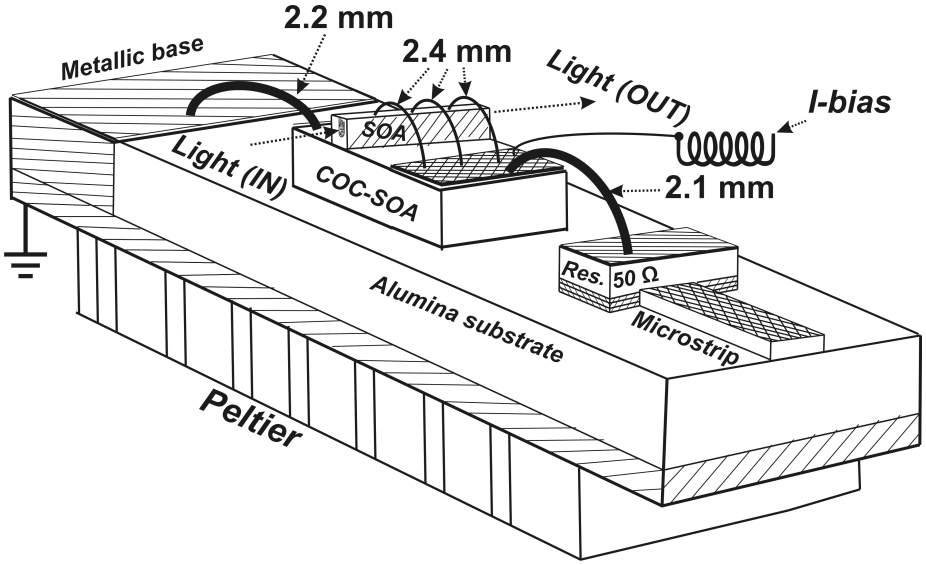

Figure 3.4: CIP-COC in series with a low inductance resistor (50 Ω) and a microstrip line (not to scale).

mm^3). The SOA electrical terminals are connected on both sides of the carrier by gold wires over gold plates, the ground plane is bounded directly over one of these plates. The Peltier element is a 10 W device able to control temperature for the whole microwave metallic enclosure ($40\times15\times20$ mm^3). The input (output) light is coupled into (from) the COC-SOA using fiber lenses positioned by 5-axis piezo actuators, all stabilized in an optical table [53], with an optical insertion loss of $\approx$ 9 dB at input plus $\approx$ 9 dB at output. The bias tee is constructed inside the microwave enclosure.

3.1.2 SOAs' characteristics

Before performing the EO switching, some characteristics of the above SOAs were observed: the SOAs' gain as a function of the injected bias current and their spectral response.

Gain

The SOAs' output power as function of injected bias current (I-bias) are illustrated in Fig. 3.5 for a laser input power (@1550 nm) of -5 dBm for packaged SOAs, and +10 dBm for CIP-COC. Such power difference is needed to compensate the higher coupling losses of the chip-on-carrier SOA.

Bandwidth

Each device bandwidth was obtained by EO responses as function of frequency, using the experimental setup illustrated in Fig. 3.6.

The optical part of the setup is composed by a tunable laser (fixed at 1550 nm), an optical isolator, a variable optical attenuator (VOA), and a PIN photodiode (*Discovery Semiconductors – DSC-R410*, up to 30 GHz). The microwave elements comprises a sinusoidal generator (*Agilent – E8257D*, up to 40 GHz, output power of 4 dBm), a radio-frequency (RF) amplifier (*SHF 810* – up to 40 GHz), and the electrical spectrum analyzer (*Agilent – E4408B*, up to 26

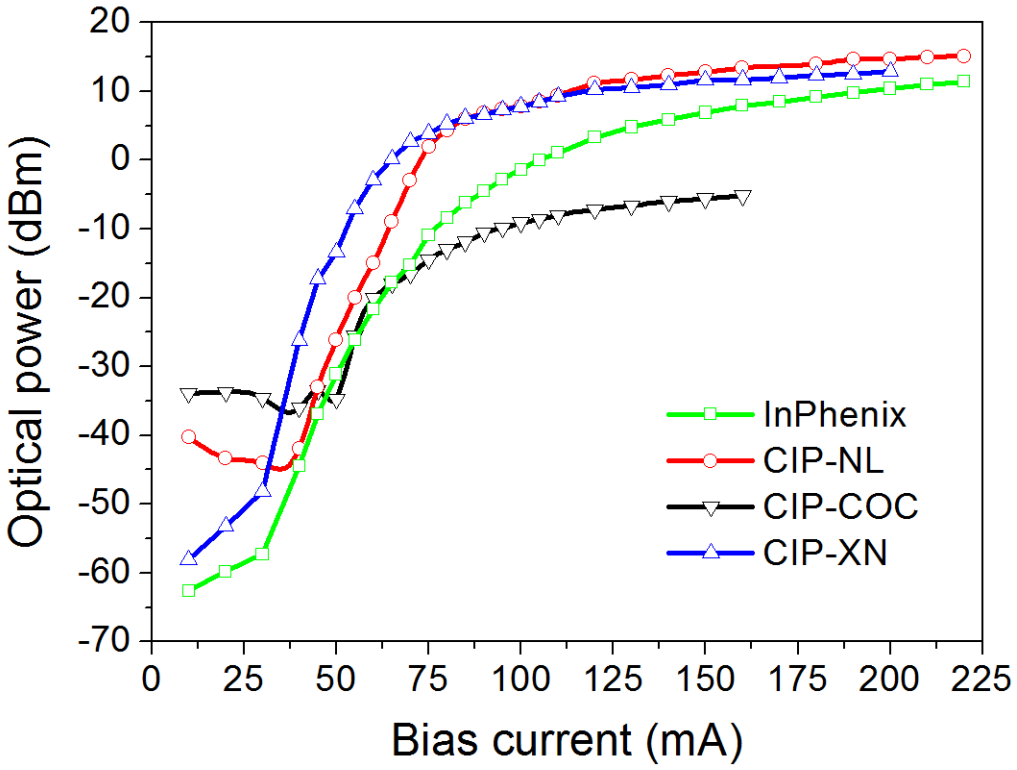

Figure 3.5: Experimental optical output power as function of I-bias, for four SOAs.

GHz). The DC I-bias was 100 mA; the input optical power was +4 dBm for the packaged SOAs and +12 dBm for CIP-COC.

Sinusoidal waveforms from the generator are amplified, added to I-bias, and injected in the SOAs' RF input. The change in the injection current causes variations in SOAs' carrier density, which in turn modifies the devices' gain observed in the optical output signal. This

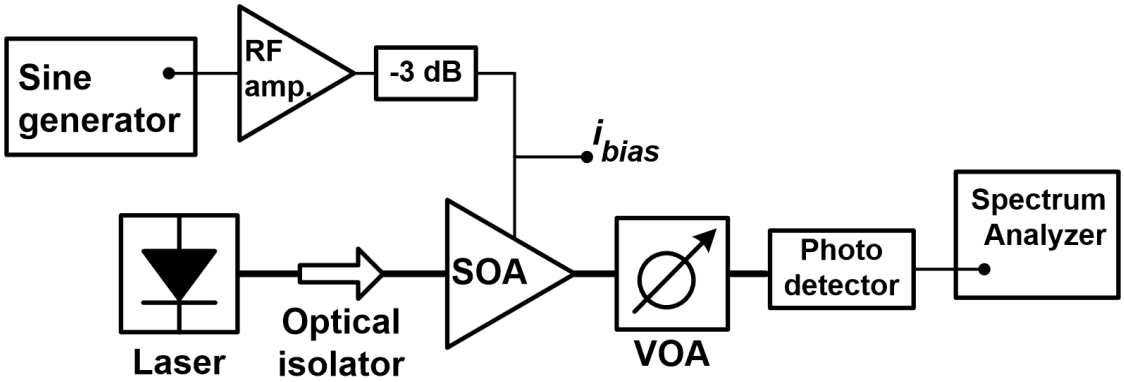

Figure 3.6: Experimental setup for the electro-optical conversion analysis.

signal is converted to the electrical domain and the peak value of spectral components as a function of frequency are extracted. A program developed (by Prof. Adriano Toazza) using LabVIEW software was used to optimize the frequency scan up to 26 GHz.

The measured data include responses from all components (generator, RF amplifier and SOA). Therefore, it was necessary to subtract (in dB) the signal generator's RF output from the total result in order to know the real responses of electro-optic conversion from SOAs. Such responses indicate the devices' bandwidth, shown in Fig. 3.7.

3.1.3 Switching procedure

The electro-optical switching behavior was investigated by injecting different electrical pulses at the SOAs, using the experimental setup illustrated in Fig. 3.8 and detailed in Fig. 3.9. The setup is composed by a 14 Gbit/s pulse generator (*Agilent – J-BERT N4903B*), followed

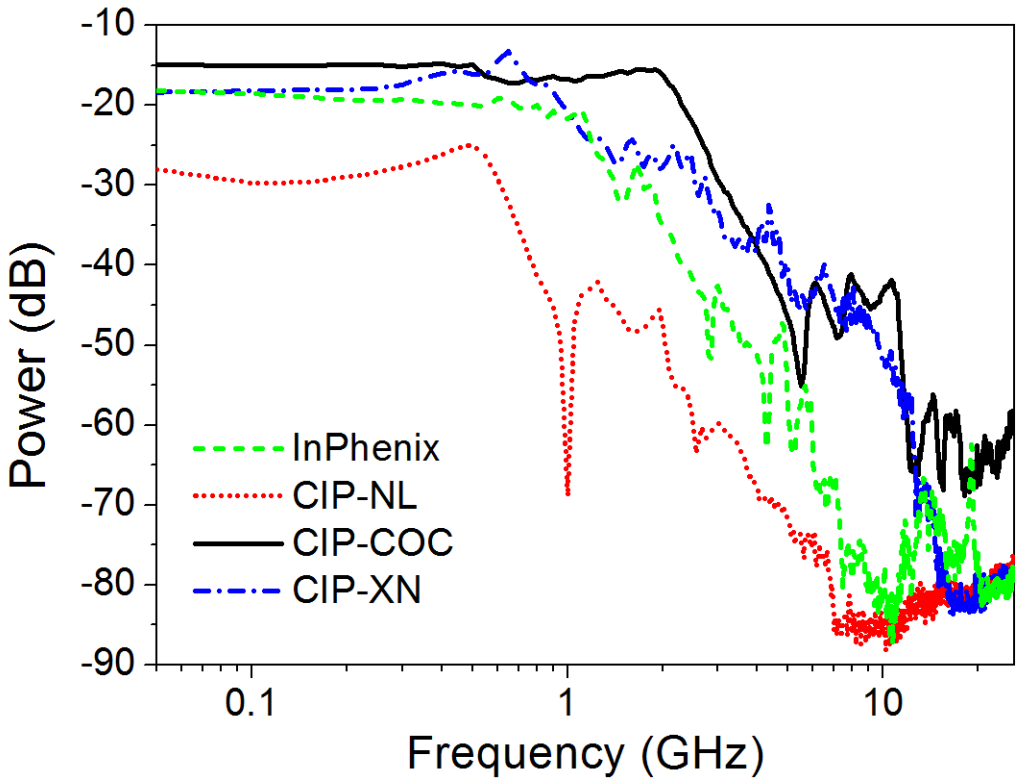

Figure 3.7: SOAs experimental EO response for a sinusoidal input up to 26 GHz.

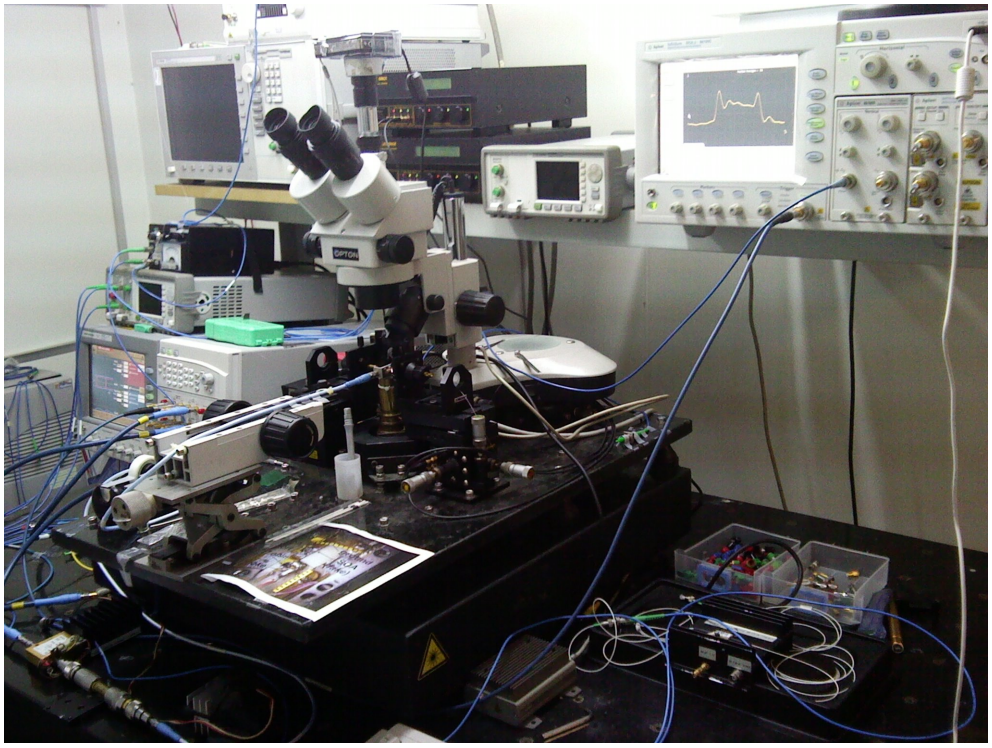

Figure 3.8: Photo of the setup showing the pulse generator (bottom left), the optical table with CIP-COC (middle), and the oscilloscope (top right).

by a microwave combiner (-6 dB), a RF amplifier (*SHF-810*), a continuous-wave (CW) tunable laser (@1550 nm, *Santec TSL-210*), the SOA under test, an oscilloscope (*Agilent – 86100C*), RF attenuators and a variable optical attenuator (VOA). The attenuators were included to reduce back-and-forth reflections and protect setup's components. All components' bandwidths are higher than 35 GHz.

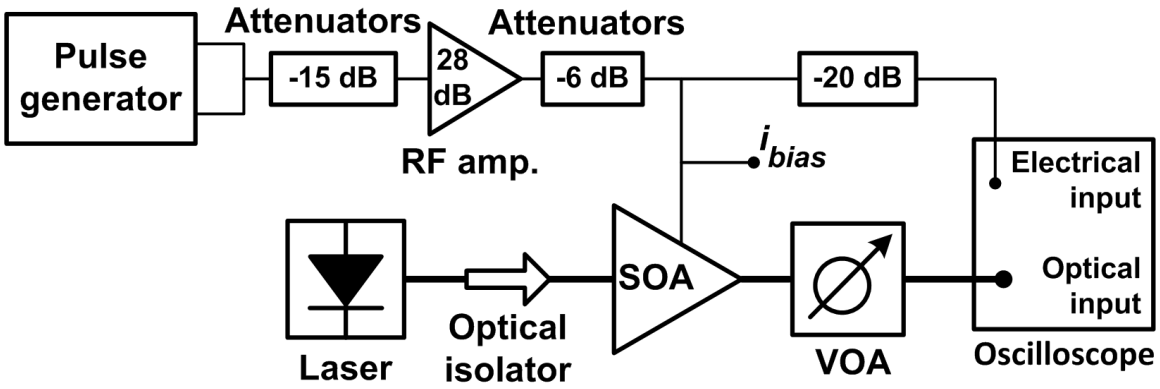

Figure 3.9: Experimental setup for electro-optical switching.

Electro-optical (EO) switching was tested with step duration of 8 ns (100 bits), followed by another 8 ns at the lower level, giving so enough time for the active cavity to be filled up by the injected current and to stabilize in steady-state condition. The PISIC technique was used also: single step combined to a narrow pre-impulse, achieving faster switching times [8].

Many parameters were adjusted to evaluate the EO switching performance for different pulse formats: injected bias current (ranging from 40 mA up to 120 mA for CIP-COC and up to 160 mA for packaged SOAs); step amplitude (1.35 V, 1.8 V, and 2.25 V), for a fixed duration of 8 ns; pre-impulse duration (from 0.32 ns to 0.96 ns) and its amplitude (from 0.3 V to 0.6 V), as illustrated in Fig. 3.10. The indicated voltage values always refer to the SOA RF input, after the attenuators and amplifier. Additionally, the influences of pre-impulse delay and optical input power were analyzed for selected I-bias pulse formats.

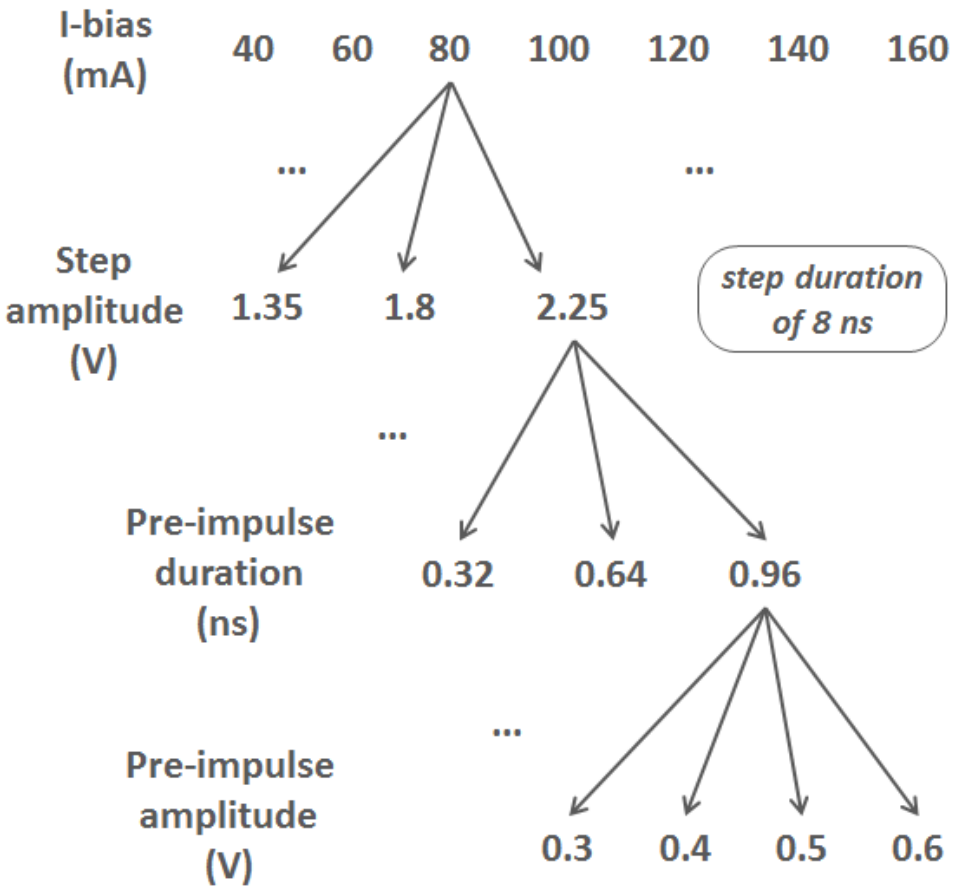

Figure 3.10: Measurements' roadmap.

3.2 Results and discussions

Large data amount was obtained for each SOA due to the variety of parameters involved in such measurements. Therefore, some selected main results are presented here, starting with few general observations, followed by highlighted results for each SOA and finally presenting a comparison of switching performances.

For the comparison, the parameters considered were the *off-on* switching time, the overshoot, and the optical contrast from SOAs' outputs, as indicated in Fig. 3.11. The switching time was calculated considering 90%–10% of the optical power output, the overshoot was calculated as the percentage extrapolating the high-level steady-state of the optical signal, and the optical contrast was calculated by the difference between the high and low levels of optical output.

We observed a common behavior to all SOAs:

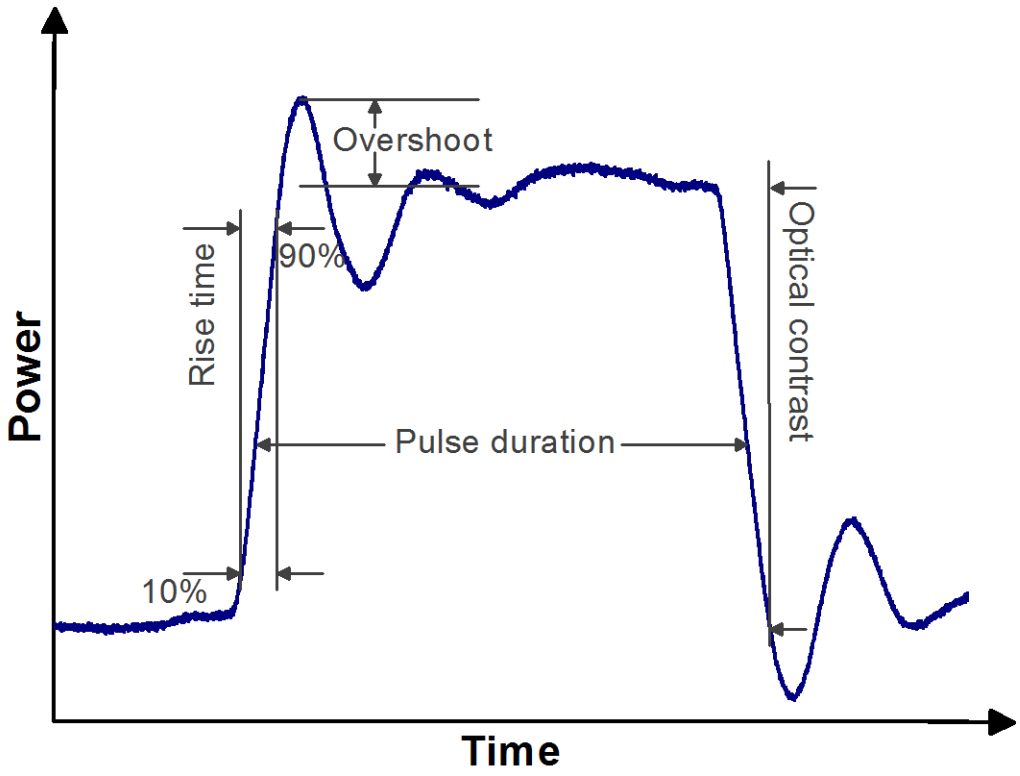

Figure 3.11: Representative pulse waveform.

- pre-impulses larger than 0.96 ns present little improvement on rise time and cause very high overshoots, which can induce errors in the receiver;
- faster rise times are achieved without pre-impulse delay, i.e., when it starts together with the step.

The SOA input power was increased up to +10 dBm for CIP-COC and of -5 dBm for encapsulated SOAs, and it was noted that the higher the power the faster the switching transition, but with intrinsic overshoots increase. After an optimum I-bias value (≈100 mA), typical dynamic gain compression limits improvements in overshoots and rise times, leading even to some deterioration for certain cases (CIP-NL).

To highlight main results from each SOA, we selected some outcomes and separated them into two categories: the highest optical contrast and the shortest rise time. The best optical contrasts for most of tests were achieved for I-bias = 80 mA, except for the CIP-XN (60 mA), by using a step of 2.25 V added to a pre-impulse with 0.6 V and 0.96 ns. For this setting, we seek the best rise time for each SOA without worrying about the other parameters (overshoot and optical contrast). The results are shown in Table 3.1, which lists the best optical contrast for each SOA, and the respective rise time and overshoot.

The shortest rise times occurred for the lowest step (1.35 V) added to the largest pre-impulse (0.6 V and 0.96 ns), I-bias current changes for each SOA. Results are indicated in Table 3.2, which lists the best rise time for each SOA, followed by the correspondent overshoot, optical contrast, and I-bias.

Table 3.1: Highest optical contrast for each SOA and correspondent rise time and overshoot.

SOA	Optical contrast	Rise time	Overshoot
InPhenix	14 dB	324 ps	45%
CIP-NL	17 dB	330 ps	80%
CIP-COC	14 dB	132 ps	72%
CIP-XN	15 dB	153 ps	223%

Table 3.2: Shortest rise time for each SOA and correspondent overshoot, optical contrast, and I-bias.

SOA	Rise time	Overshoot	Optical contrast	I-bias
InPhenix	163 ps	67%	3 dB	160 mA
CIP-NL	240 ps	480%	10 dB	60 mA
CIP-COC	100 ps	80%	5 dB	100 mA
CIP-XN	107 ps	36%	1.5 dB	160 mA

Most of the results presented so far have impractical overshoots and/or low optical contrasts. Moreover, the different configurations used for each device make an adequate comparison impractical. Therefore, we set some parameters for a fair performance analysis of the SOA-based electro-optical switches under test: a similar optical contrast for all SOAs (≈14 dB) and an optimized pulse format – composed by a step of 2.25 V added to a pre-impulse with duration of 0.32 ns, with small rise times and moderate overshoots, whose values vary according to the SOA, as will be detailed below. By using such selected pulse the trade-off between rise time and overshoot as a function of pre-impulse amplitude (0.3 V – 0.6 V) was studied. The applied electrical pulse with the maximum pre-impulse (0.6 V) is illustrated in Fig. 3.12.

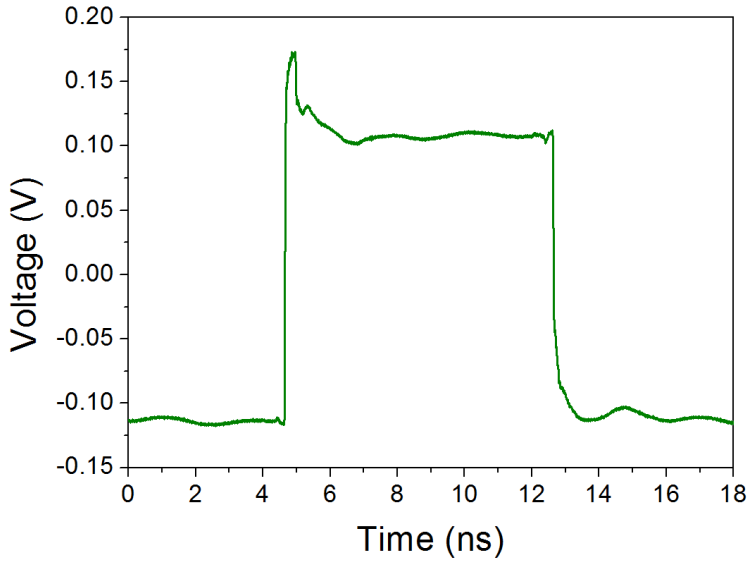

Figure 3.12: Electrical pulse applied to SOAs in the comparison: step of 8 ns and 2.25 V, pre-impulse of 0.32 ns and 0.6 V.

In order to compare the same pulse whilst maintaining similar optical contrast, the injected bias current was varied for each SOA: InPhenix = 100 mA; CIP-NL = 90 mA; CIP-COC = 80 mA; and CIP-XN = 70 mA. The optical input power is -5 dBm for packaged SOAs and +10 dBm for CIP-COC. The SOAs' responses for the pulse shown before (Fig. 3.12) are illustrated in Fig. 3.13, while the calculated rise times and overshoots as functions of pre-impulse amplitude are presented in Fig. 3.14.

The results show that the higher the amplitude the faster the rise time, but with inherent stronger overshoots. The InPhenix is the most linear device among the SOAs under test, presenting low overshoots and modest rise times. It is possible to see that the rise times

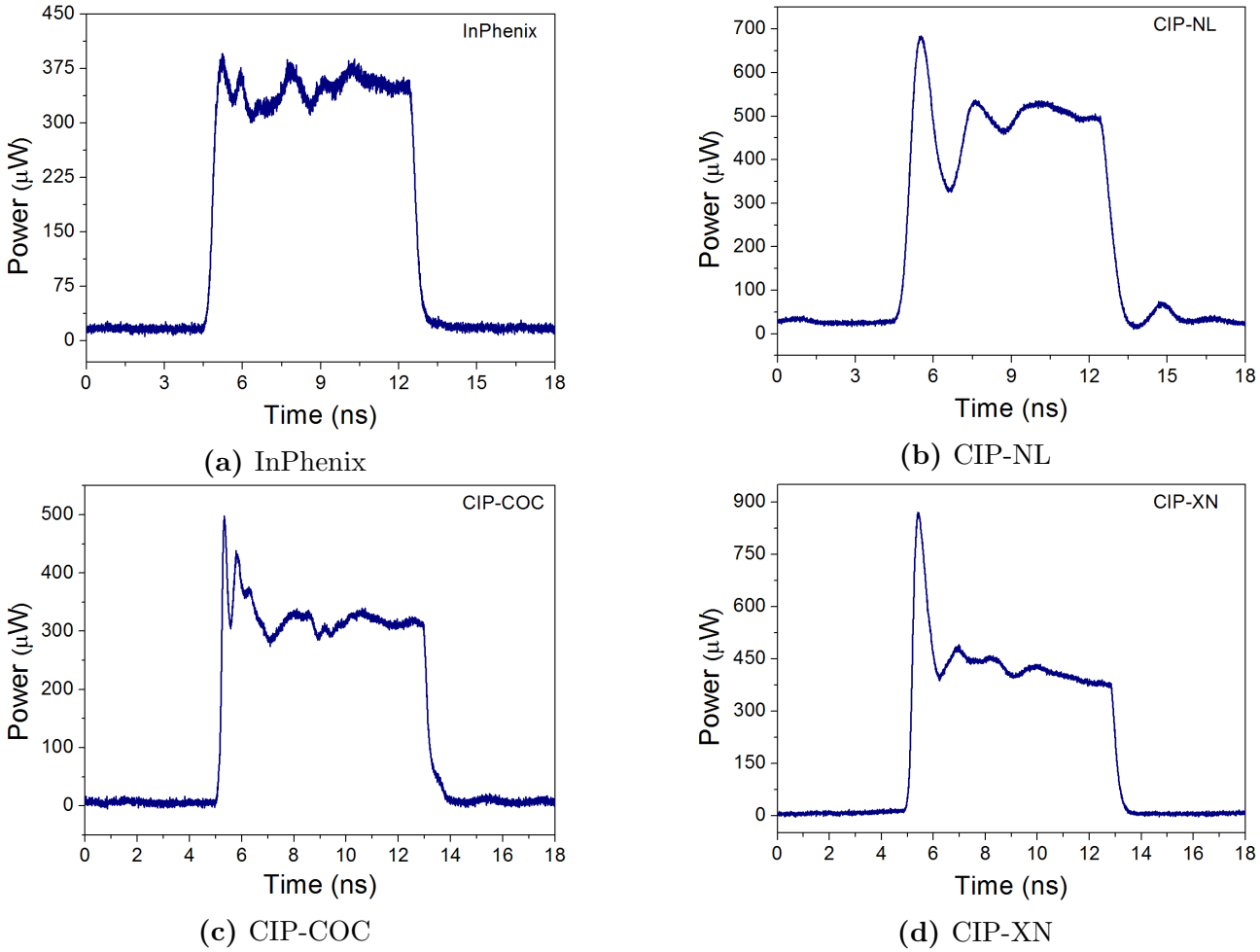

(a) InPhenix **(b)** CIP-NL

(c) CIP-COC **(d)** CIP-XN

Figure 3.13: Experimental SOAs optical outputs for a step of 8 ns and 2.25 V added to a pre-impulse of 0.32 ns and 0.6 V.

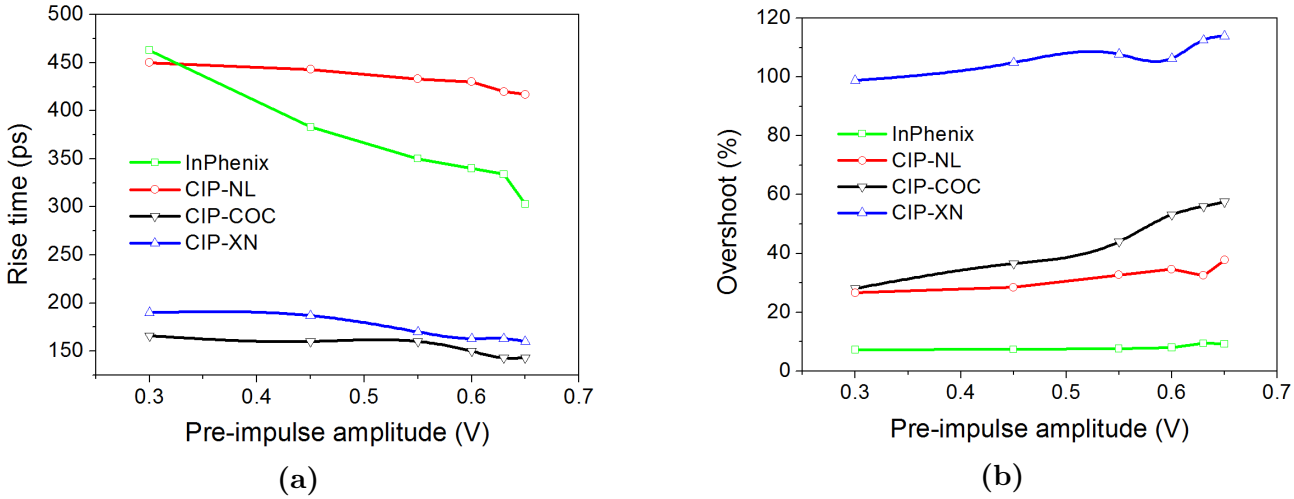

Figure 3.14: SOAs **(a)** rise time and **(b)** overshoot versus pre-impulse amplitude, for 2.25-V step and 0.32-ns pre-impulse.

have a significant variation, reducing in more than 150 ps with the increase of pre-impulse amplitude. The InPhenix's overshoots are the lowest among the tested SOAs, remaining below 10% with little variation.

The CIP-NL is a non-linear device, but with response times worse than that of the InPhenix, and with stronger overshoots (≈30%). The CIP-COC is the chip-on-carrier version of CIP-NL (with reduction of packaging parasitic elements) and it achieves the fastest *off-on* switching time (≈150 ps), but its overshoots have the strongest variation with increasing of pre-impulse amplitude. CIP-XN is an extremely non-linear SOA, also with short rise times, slightly bigger than those of the CIP-COC, but with the highest overshoot among all tested devices. In all cases, it is possible to notice the trade-off between rise time and overshoot, which is achieved close to pre-impulse amplitude of 0.5 V.

3.3 Concluding remarks

The comparative analysis of four SOA-based electro-optical switches was presented. Optical contrasts up to 17 dB (for CIP-NL) and ultrafast switching times (100 ps for CIP-COC) were observed. The analysis presented here may help in possible optimization to be

made in the fabrication of electro-optical switches based on SOAs. Devices with broad electrical bandwidth (CIP-COC and CIP-XN) showed the fastest switching times. The non-linear devices achieved faster response with lower I-bias current, while InPhenix (the linear one) presented the smallest overshoots. The chip-on-carrier SOA (CIP-COC) demonstrated the influence of parasitic elements, presenting faster response than its packaged version (CIP-NL).

Chapter 4

Multi-Impulse Step Injected Current Technique

From the results presented in Chapter 3, we can see that the pre-impulse considerably improves the rise time, but with inherent higher overshoot. Thus, on this chapter a new technique (patent pending) employing Multi-Impulse Step Injected Current (MISIC) is presented to reduce the output power overshoots, keeping fast rise times and high optical contrasts. [1]

Experimental results obtained for a SOA-based EO switch using the PISIC and the MISIC formats are presented, with analysis of the switching time improvement and the overshoot minimization. Using CIP-COC, switching times below 115 ps were achieved with high optical contrast ($\approx$ 30 dB) and overall optical overshoot reduction of 50%.

[1] This chapter is based on the results presented in the following article:
R. C. Figueiredo, N. S. Ribeiro, A. M. O. Ribeiro, C. M. Gallep, E. Conforti. "Hundred-Picoseconds Electro-Optical Switching with Semiconductor Optical Amplifiers using Multi-Impulse Step Injection Current", *J. Lightw. Technol.*, vol. 33, pp. 69–77, 2014. DOI: 10.1109/JLT.2014.2372893 (*open access*).
And in the required patent:
R. C. Figueiredo, N. S. Ribeiro, C. M. Gallep, E. Conforti. "*Método de chaveamento eletro-óptico empregando multi-impulsos e degrau de corrente via amplificadores ópticos a semicondutor, dispositivos para chaveamento eletro-óptico de portadoras ópticas, e uso dos dispositivos*", PCT/BR2012/000469. "Method for electro-optical keying using multiple pulses and current stepping via semiconductor optical amplifiers, devices for electro-optical keying of optical carriers, and use of the devices", registration number: WO2013142928A1, 2012.

4.1 Materials and methods

The experimental setup is shown in Fig. 4.1. The optical setup contains a CW tunable semiconductor laser, an optical isolator, a commercial chip-on-carrier SOA (CIP-COC – described before in Chapter 3), a variable optical attenuator, and a 40 GHz digital communication analyzer with optical input port.

In the electrical setup the pulse generator is the fundamental module, enabling different composite pulse formats that are further combined to switch the SOA. The generator (*Agilent J-BERT N4903B*) has two separate output channels for two independent pulse formatting: each one is constructed by different bit sequences (bit window of 80 ps). The two electrical outputs channels are combined (50 GHz bandwidth resistive combiner) and amplified. The resultant electrical pulses are injected into the CIP-COC using a 50 Ω low inductance series resistor, providing the impedance matching (SOA impedance ≈ 3.5 Ω), after injection of bias current (I-bias, by a 40 GHz bandwidth bias-tee). The microwave amplifier setup shown comprises a tap to visualize the electrical signal, amplifiers and matching circuits. A 3 dB attenuator was included between the amplifier output and the SOA gate to reduce back-and-forth reflections, and to protect the amplifier against variations of SOA impedance. The components have a

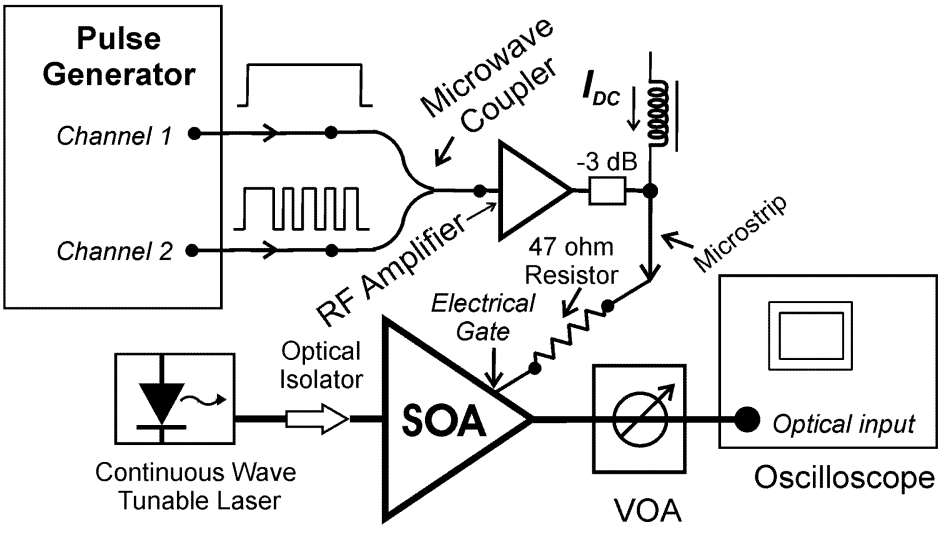

Figure 4.1: Experimental setup for electro-optical switching analysis.

minimum bandwidth of 35 GHz. The maximum applied signal to the SOA electrical gate is limited to 6.4 V_{pp}. Therefore the maximum current excursion is 120 mA – so, considering I-bias of 80 mA, the injected current will have an excursion from 20 mA to 140 mA. However, if the pre-impulse is also considered with the step, the current excursion will change from 120 mA to 90 mA (step: 4.7 V and impulse: 1.7 V) or 50 mA (step: 2.7 V and impulse: 3.7 V).

Typical PISIC and MISIC formats are illustrated in Fig. 4.2. Basically, three sectors are conformed to optimize the EO switching: the pre-impulse part 'A', the immediate sequence part 'B' and the final part 'C'. PISIC format is shown in the superior trace of Fig. 4.2: it has just an impulse in the 'A' section plus the normal step signal. The Misic1 and Misic3 are shown in the medium and inferior traces of Fig. 4.2. MISIC formats have an impulse in the part 'A' but also have impulses in parts 'B' and 'C'. Proper impulses duration and amplitudes used in part 'B' may minimize the initial output overshoot; part 'C' may counteract the relaxation oscillations during the switching window by injecting short current pulses. The MISIC formats are empirically adjusted and will be detailed next, in section 4.2.3.

The switch step response is shown in Fig. 4.3, where Fig. 4.3(a) illustrates a typical electrical 8 ns step pulse, using just one generator channel at maximum voltage (6.4 V), after RF amplification. The pulse rise time is 50 ps in this case. The CW laser provides maximum

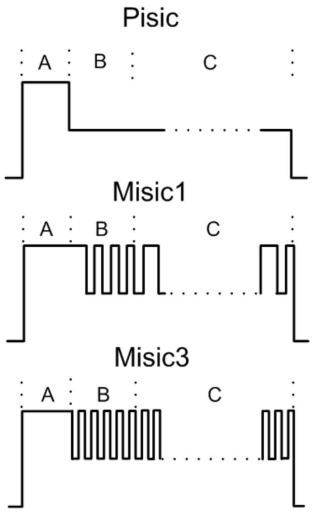

Figure 4.2: Examples of PISIC and MISIC formats.

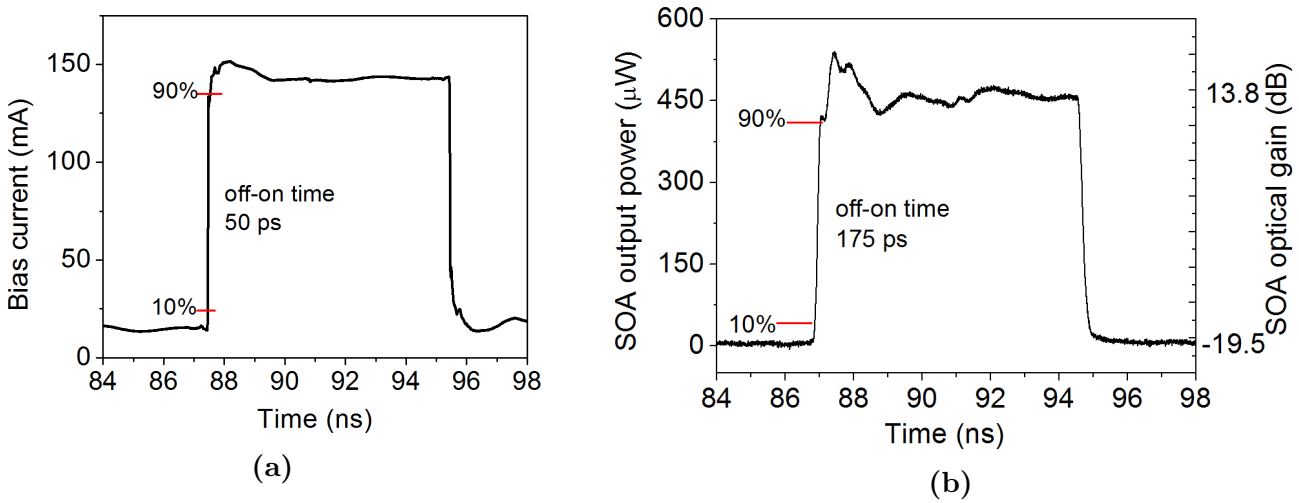

Figure 4.3: (a) Electrical step (I-bias: 80 mA); (b) CIP-COC optical response for electrical input of (a).

optical power of 5 dBm, leading to SOA P_{in} = -4 dBm, giving the best switching times. Tests for smaller P_{in} were performed as well (not shown here), with response speed decreased depending on format of composite pulse. For SOA P_{in} = -14 dBm, for example, switching time increases in 10% to 20% depending on pulse format. Fig. 4.3(b) shows the output optical signal (considering insertion losses) in response to the drive signal of Fig. 4.3(a), achieving optical contrast greater than 30 dB.

4.2 Results and discussions

The switching performance obtained for different pulse formats are presented in this section, starting with the most simple format – single step – whose results are compared to the ones obtained by composite pulses, always aiming to reduce switching times and fluctuations in the output power.

4.2.1 Step

The simplest version for the current injection format is a fast-rise step signal, as shown in Fig. 4.3(a). The step duration is 8 ns (100 bits), followed by another 8 ns at the lower level, giving so enough time for the active cavity to be filled up, by the injected current and to stabilize in steady-state condition. This time window is used for all results presented here.

The optical response to that, as in Fig. 4.3(b), presents an *off-on* rise time (10% – 90%) of 175 ps, an improvement of 3.7 times in relation to the results presented in previous works (650 ps) [10, 11]. This improvement can be obtained using the CIP-COC with a higher bandwidth ($\approx$ 40 GHz) microwave setup, and a higher optical gain due to the longer SOA (2 mm) used here; the previous results were achieved for encapsulated, 0.65-mm long SOAs [10,11]. This better performance of CIP-COC was also demonstrated in Chapter 3.

Despite the small switching time, the optical response shows power overshoot (16%) and spurious fluctuations following that. This overshoot arises in response to the huge current step and it is an intrinsic SOA response. For a step from 45 mA to 115 mA, a similar *off-on* time was noted (170 ps) but with higher overshoot (18%) and smaller optical contrast (21.5 dB).

4.2.2 Pre-Impulse Step Injected Current (PISIC)

There is a minimum time for the SOA to turn on since the active region, initially empty, must be populated by the injected current, and so the optical gain changes. The SOA's optical gain increases with a time constant comparable to that of electrical carrier lifetime, at the beginning of the current step rises. The so-called carrier lifetime is not really a constant value since it changes with the population density, both electrical and optical [12, 26, 54]. A high but short current pulse can be used to quickly increase the carrier population, decreasing the SOA carrier lifetime and enabling reduction in switching times. In this sense, the PISIC technique is demonstrated to decrease the *off-on* times.

Figure 4.4(a) shows the electrical pulse constructed with PISIC – a pre-impulse combined with the step. To do that, the two generator outputs are combined before the RF amplification. The electrical rise time (50 ps) is the same as before. However, the optical output power contrast is reduced to 29 dB (due the RF amplifier saturation), but the *off-on* rise time has almost 35% reduction, to 115 ps (Fig. 4.4(b)).

The pre-impulse has some features (width and amplitude) that can be modified in order to contribute to decrease the *off-on* times. Those width and amplitude choices were made by considering the better relation for *off-on* time versus overshoot and limiting the maximum overshoot in 30%. The best result obtained is presented here: a pulse of 6-bit width (0.48 ns) and maximum amplitude.

The PISIC reduces the rise time but increases the overshoot, as can be seen in Fig. 4.5, which illustrates the comparison between a single step and the PISIC technique – the rising time reduction is detailed in the inset zoom. Figure 4.5(a) shows the optical response for a simple step current and for PISIC format with step amplitude of 2.7 V and pre-impulse of 3.7 V. The overshoot increases to 63% with the PISIC technique. The overshoot value is excessive if compared with the established limit (30%), although the *off-on* time decreased. Therefore, it would be interesting to have a technique that could reduce the overshoot without increasing the *off-on* times, since high overshoots may disturb decision level to be chosen at the receiver

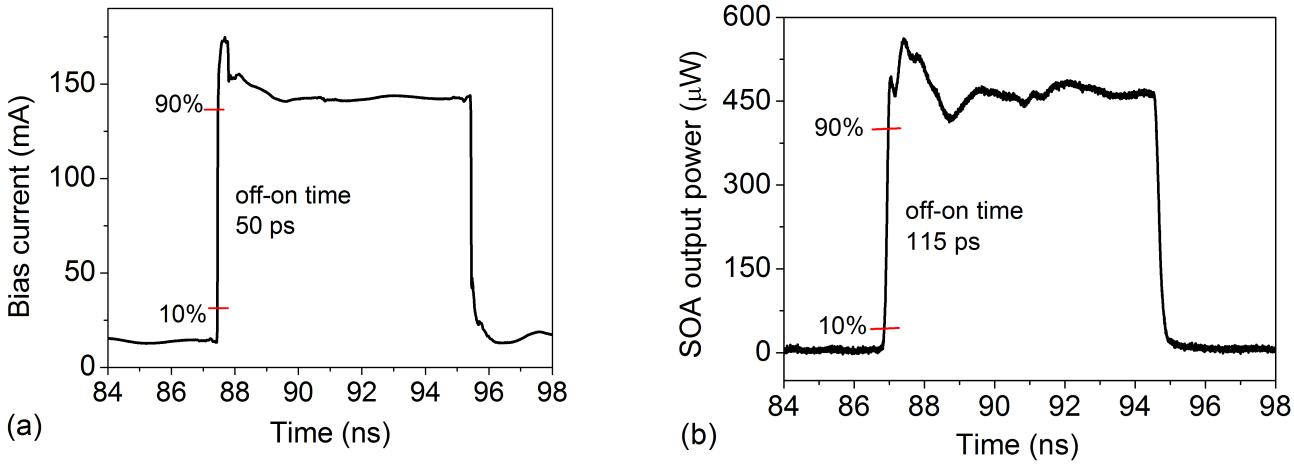

Figure 4.4: (a) PISIC format (I-bias: 80 mA), (b) CIP-COC optical response to (a).

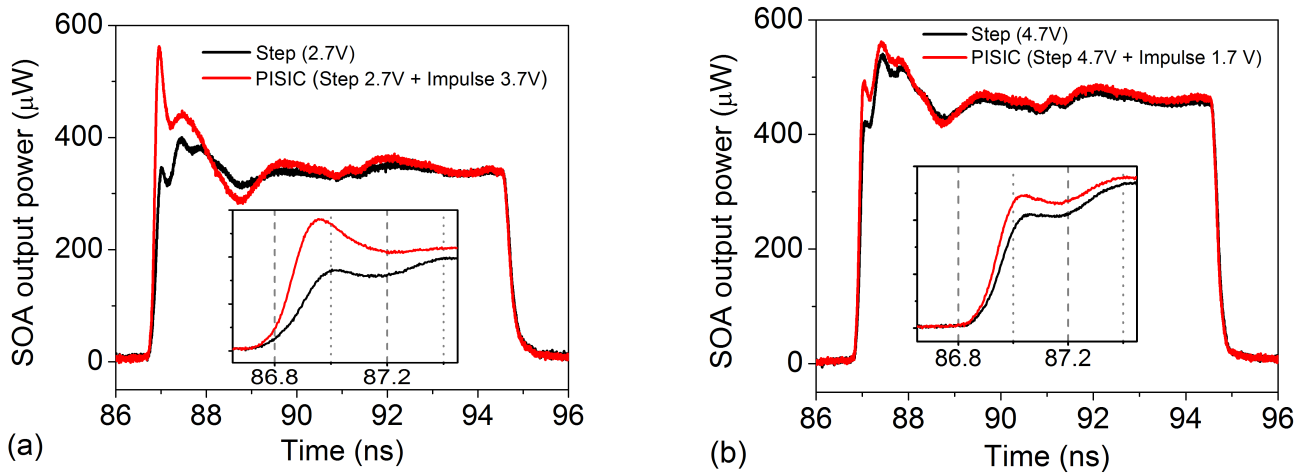

Figure 4.5: Optical response for single step and PISIC bias current formats (I-bias: 80 mA), (a) with impulse of 3.7 V and step of 2.7 V;(b) with impulse of 1.7 V and step of 4.7 V.

at the end of the optical link. Figure 4.5(b) illustrates the comparison between a simple step injected current and the PISIC with step amplitude of 2.7 V and pre-impulse of 3.7 V. In this case the CIP-COC gain is saturated due to high injected current and thus the overshoot is not too high.

4.2.3 Multi-Impulse Step Injected Current (MISIC)

By observing the optical response obtained by the PISIC format it is possible to analyze the effect of a proper sequence of pulses (i.e., bits in the signal generator) to reduce the initial overshoot and the fluctuations without increasing the *off-on* time. This was done by combining different bit sequences from the two independent electrical channels, as presented in Table 4.1.

Figure 4.6(a) illustrates one kind of MISIC (Misic1) built with a step followed by multiples impulses (see Table 4.1), in a total of 100 bits. Figure 4.6(b) shows the correspondent SOA optical output. The impulse sequence contributes to increase the bias current average level. However, due to the upper level (140 mA) being near to the gain saturation, higher bias currents modify only a little the optical contrast, from 29 dB (Step and PISIC) to 30 dB (Misic1). The optical response shows a slightly increase of the upper level (but not sufficient to modify the *off-on* time) and the overshoot is reduced to 12.5%. The price to pay is the higher power

Table 4.1: Bit sequences for different MISIC formats using bit windows of 80 ps.

	Sections (100 bits multi-impulses: 8 ns)		
	A	**B**	**C**
Misic1	111111	11010101	011 011 011 ... 011
Misic2	111111	01101101	1 011 011 011 ... 110
Misic3	111111	01010101	0101 0101 ... 0101
Misic4	010101	01010110	1 011 011 011 ... 011
Misic5	011011	01010110	11 011 011 ... 011
Misic6	111111	11111111	1111 1111 ... 1111

consumption, since the energy to switch the SOA increases from 9.1 nJ (Step and PISIC) to 10.4 nJ (Misic1), i.e., an increase of 15%. Those energy levels were estimated from the electrical power calculated using 8-ns-long composed pulses, used to switch the SOA (Fig. 4.4(a) and Fig. 4.6(a)). However, the MISIC impulses also increase the SOA gain.

Table 4.2 presents the optical contrasts obtained for all cases, with good performance (>25dB), with steps of 4.7 V. Figure 4.7 illustrates the *off-on* switching times and correspondent overshoot values (%) obtained for the MISIC formats. In both cases – 2.7 V and 4.7 V for the step signal – the Misic1 format has better results, reducing the overshoot and *off-on* times. Steps with 2.7 V promote lower bias currents, below the gain saturation levels and so contribute

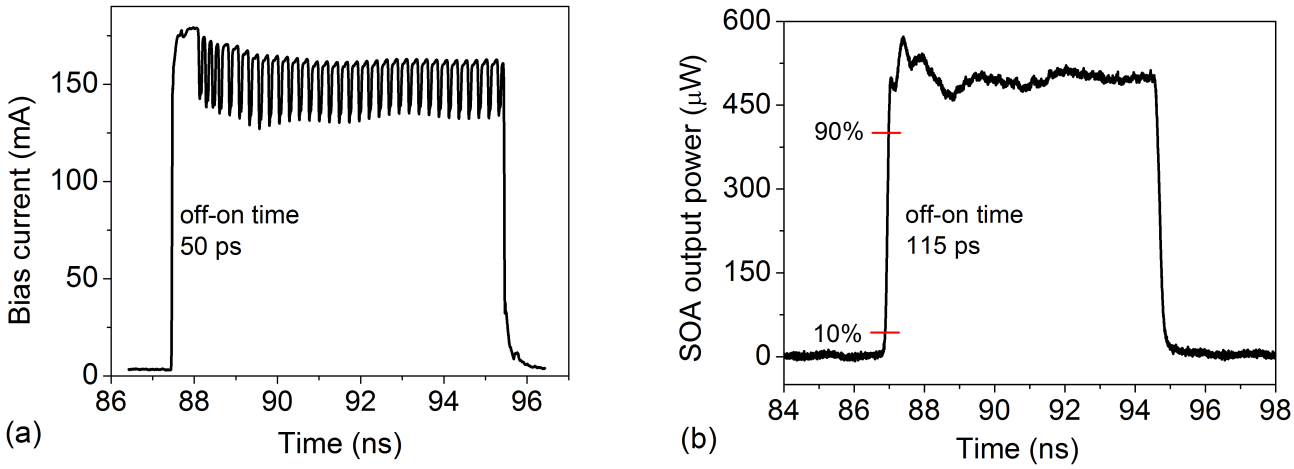

Figure 4.6: (a) Misic1 electrical pulse (I-bias: 80 mA); (b) CIP-COC optical response to (a).

Table 4.2: Optical contrasts.

	I-bias: 60 mA		**I-bias: 80 mA**	
Pulse	Step 2.7 V Impulse 3.7V	Step 4.7 V Impulse 1.7 V	Step 2.7 V Impulse 3.7 V	Step 4.7 V Impulse 1.7 V
Step only	29 dB	27 dB	27 dB	32 dB
PISIC	25 dB	31.5 dB	12.5 dB	29 dB
Misic1	27 dB	32 dB	17 dB	30 dB
Misic2	27 dB	32 dB	17 dB	30 dB
Misic3	27 dB	32 dB	17 dB	30 dB
Misic4	27 dB	32 dB	17 dB	30 dB
Misic5	27 dB	32 dB	17 dB	30 dB
Misic6	28.6 dB	33 dB	18 dB	32 dB

to enhance the technique efficiency.

The Misic4 format presented the worst result. Although it reduces the overshoot there is a large increase in the *off-on* time. Misic2, Misic5, and Misic6 reduce the overshoot but increase the switching times. The optical responses for the simple step, the PISIC and Misic1

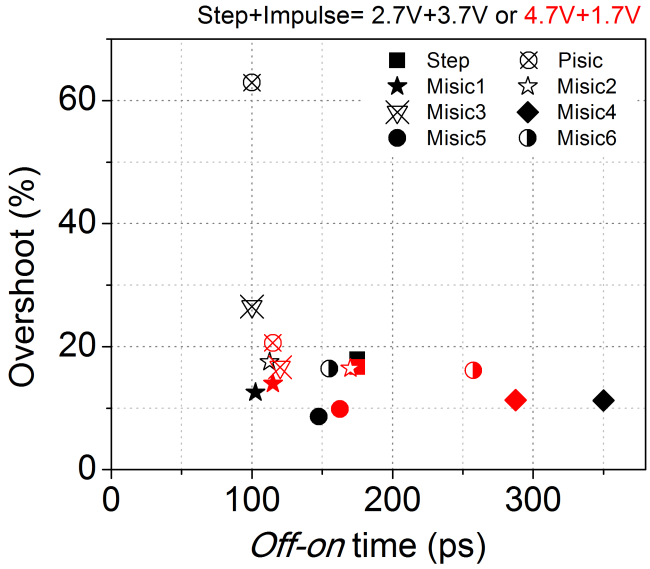

Figure 4.7: Measured overshoots and *off-on* times for different pulse formats (I-bias: 80 mA, pre-impulse of 3.7 V and step of 2.7 V or pre-impulse of 1.7 V and step of 4.7 V).

formats are shown in Fig. 4.8(a): for impulse of 3.7 V and step of 2.7V; and in Fig. 4.8(b): for impulse of 1.7 V and step of 4.7 V.

The advantage of MISIC is clearly seen in relation to PISIC (reduction of overshoot), and in relation to step (reduction of rise time). The upper level of MISIC presents small fluctuations and this might be a consequence of the interaction between MISIC impulses and SOA carriers relaxation, since the impulses of Misic1 shown in Fig. 4.6(a) repeat every 240 ps (4.16 Gbit/s) with first harmonic around 2 GHz that is close to the SOA relaxation oscillation frequency. In addition, the SOA response also presents undershoot that is more pronounced just after the rise time. In those cases MISIC has advantage over PISIC as shown in Fig. 4.8(a), for example.

Experimental results for I-bias of 60 mA are shown in Fig. 4.9, with best performance for Misic6. The Misic5 format has the worst switch time although presents great overshoot reduction. The Misic1 format presents a good performance but not the best as before, showing that the best format is also dependent on the I-bias.

Figure 4.10 shows the optical response for the single step, the PISIC and the Misic6 formats, for impulse of 3.7 V and step of 2.7 V (a) and impulse of 1.7 V and step of 4.7 V (b) (for

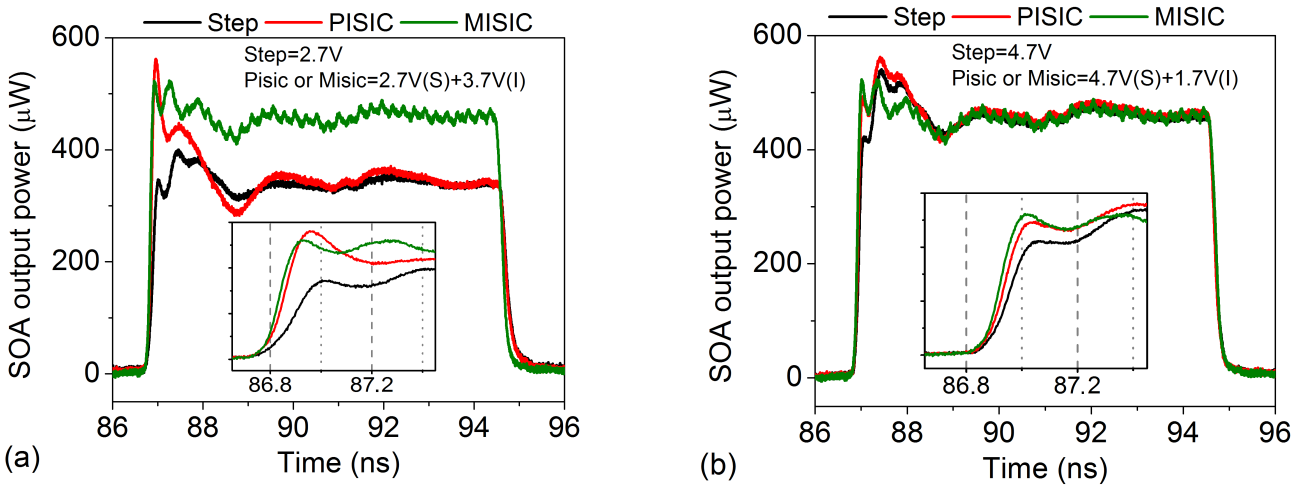

Figure 4.8: Optical responses for a single step bias current, PISIC, and Misic1 formats (I-bias: 80 mA), (a) with impulse of 3.7 V and step of 2.7 V; (b) with impulse of 1.7 V and step of 4.7 V.

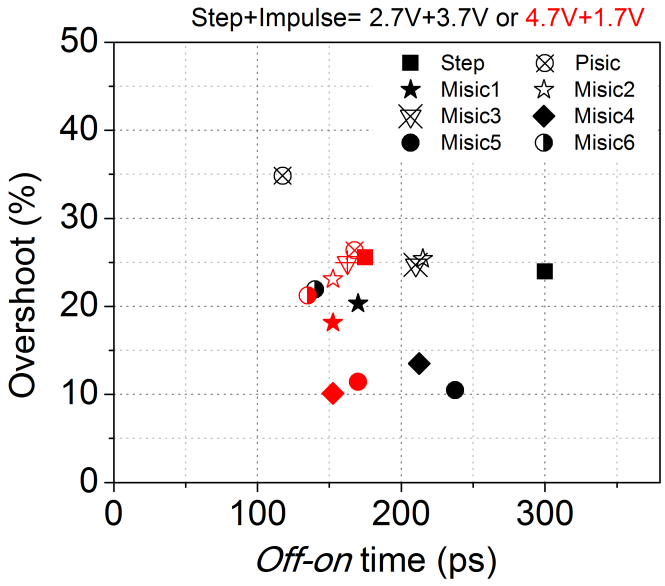

Figure 4.9: Measured overshoots and *off-on* times for different pulse formats (I-bias: 60 mA, pre-impulse of 3.7 V and step of 2.7 V or pre-impulse of 1.7 V and step of 4.7 V).

I-bias: 60 mA). The increase in optical contrast is clear, with reduction of relative overshoot incidence. The *off-on* time is similar for Misic6 and PISIC formats, much shorter than the obtained for simple step format with 2.7 V (300 ps).

The comparison between pulses with different bias currents shows that the MISIC technique works for all cases, although the best formats have a dependence of how close the

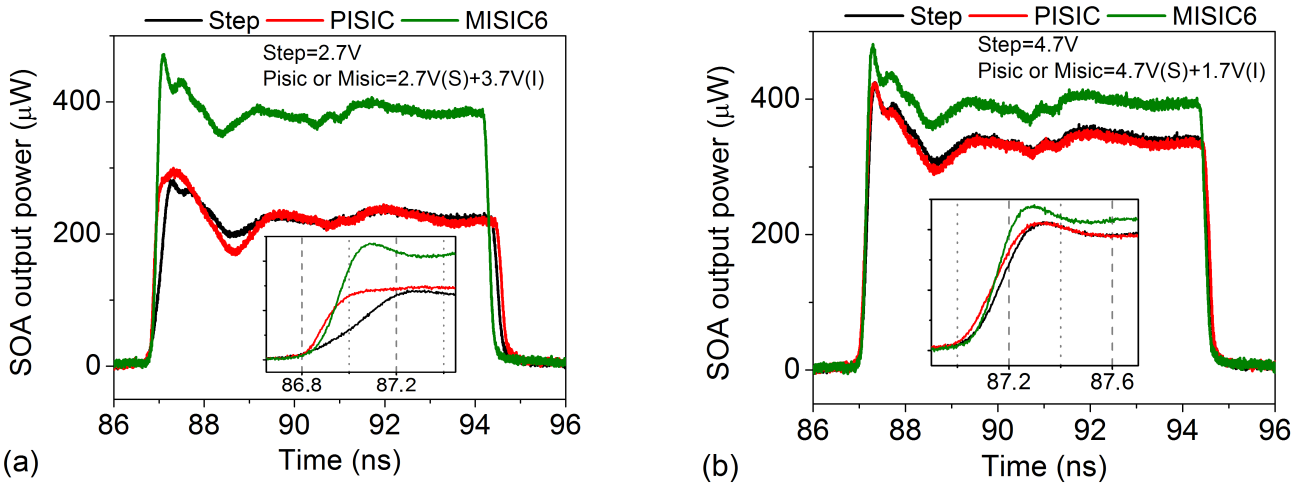

Figure 4.10: Optical response for a step injected current, Pisic, and Misic6 formats (I-bias: 60 mA), (a) with impulse of 3.7 V for step of 2.7 V; (b) impulse of 1.7 V for step of 4.7 V.

total signal is to the gain saturation level. The overshoot reductions enable a relative decrease around 50% (while the *off-on* times are kept constant) in comparison to the simple step and the PISIC formats.

The fluctuations decrease is important to improve the signal reception quality, reducing bit errors. Other advantage of MISIC may be its flexibility, since the signal format can be constructed using adequate bit combinations for each desired I-bias. The MISIC also could be used in directly modulation of VCSELs, which are used in optical interconnects, increasing the modulation speed of those lasers. In future applications of recirculating buffers based on SOA-gate arrays [55, 56], a multi-level, phase-modulated optical carrier might be the choice and the SOA chirp during switching would be relevant. The SOA chirp would affect even amplitude-modulated signals when passing further by optical filters, therefore inducing frequency-to-amplitude conversion. It is interesting to note that the laser chirp is mostly relevant during the SOA gain rising, in the *off-on* electro-optical switching [57]. Therefore, the faster rise times obtained with the MISIC technique would present a smaller time interval of chirp occurrence.

It should be noted that during the *on-off* switching the SOA suffers a carrier depletion. Experimental results [11] shows that PISIC can decrease the *on-off* time by depleting the SOA faster than a single step down. However, the MISIC technique would not be necessary in this case since there is no gain fluctuation after the *on-off* time interval. A linear SOA must be provided in applications such as optical space switches to avoid inter-channel cross-talk. Those high-linear devices, with bigger active volume, generally would need higher bias currents, and the electro-optical switching would require a stronger microwave signal. Since very fast broadband microwave amplifiers hardly surpass 9 V_{pp}, the AC current excursion would be just 150 mA, not enough to provoke deep gain saturation for PISIC and MISIC techniques. However, the conclusions presented here about MISIC advantages can be applied to linear devices, as soon as SOA gain excursion from below transparency to deeply saturation is obtained using an electrical signal with a rise time (10% – 90%) faster than 50 ps.

4.3 Concluding remarks

Experimental results of electro-optical switching based on CIP-COC were presented. *Off-on* times of 175 ps with optical contrast of 32 dB were obtained by simple-step current applied to such nonlinear device, which tends to present fast switching times. Besides, the 2-mm-long active region and the high bias current can provide better input power dynamic range, enabling faster operation [58]. By using the PISIC format, the switching times are reduced to 115 ps but with high overshoots and fluctuations, issues minimized using MISIC formats. MISIC provides fast switching times due to the first, stronger impulse added to the single step, as for the PISIC format, but its further sequence of short pulses counteracts the output power fluctuations inherent to the gain relaxation, and at the same time increases the average injected current, improving the desired optical contrast.

MISIC is demonstrated as an efficient technique to reduce the residual fluctuations in the SOA output: *off-on* times of 115 ps with small overshoot and high optical contrast were achieved for the CIP-COC. The technique may improve the performance of others electro-optical switches, if SOAs similar to those used in this thesis were employed.

Chapter 5

Equivalent Circuit Modeling

This chapter presents the equivalent electrical circuit modeling for three different SOAs. Initially, the SOAs' active region modeling is presented, followed by their mount and chip parameters' extraction. Simulated results from the equivalent circuits (ECs) are then compared to experimental data. [1]

As seen before in Chapter 2 (page 30), given the devices similarities, the SOAs models here presented are based on previous models developed for semiconductor lasers [22–24]. However, while the laser active region models are separated into below and above threshold, the SOAs models are separated into high-gain and low-gain operation modes, according to their gains' profile (see Fig. 3.5 – page 38). For low-gain mode operation (I-bias < 70 mA for devices used here), when ASE level is still small and there is no gain compression, the active region model is simpler than for high-gain mode, as will be detailed next.

[1] This chapter is based on the results presented in the following articles:

R. C. Figueiredo, N. S. Ribeiro, C. M. Gallep, E. Conforti. "Bias Current Influence on Semiconductor Optical Amplifier's Equivalent Circuit", *Opt. Commun.*, vol. 336, pp. 153–159, 2015.

R. C. Figueiredo, N. S. Ribeiro, C. M. Gallep, E. Conforti. "*Frequency and Time-Domain Simulations of Semiconductor Optical Amplifiers using Equivalent Circuit Modeling*". Submitted for publication.

R. C. Figueiredo, N. S. Ribeiro, A. M. O. Ribeiro, C. M. Gallep, E. Conforti. "Hundred-Picoseconds Electro-Optical Switching with Semiconductor Optical Amplifiers using Multi-Impulse Step Injection Current", *J. Lightw. Technol.*, vol. 33, pp. 69–77, 2014. DOI: 10.1109/JLT.2014.2372893 (*open access*).

5.1 Active region modeling

For low-gain mode the model is composed by the space-charge capacitance (C_{sc}) in parallel with the diffusion capacitance (C_d) and the diffusion resistance (R_d). C_{sc} is related to the storage of charge carriers at the diode heterojunction, and C_d is related to their effective lifetime; R_d is the resistance associated to the heterojunction that turns to an effective resistance (R_1) in the high-gain mode model, which is completed by the inductance L_s – related to photons' storage, the gain compression resistance (R_{s1}) and the spontaneous emission's coupling factor resistance (R_{s2}). The total capacitance ($C_{sc} + C_d$) and the L_s represent the energy exchange between carriers and photons, while the resistances represent the resonance damping. The active region modeling, including elements for high and low-gain modes is illustrated in Fig. 5.1. Voltage on R_d and R_{s2} is proportional to the optical output power for low and high-gain, respectively.

The parameters are calculated as a function of the injected bias current (I-bias), according to the equations detailed in Chapter 2 and repeated here for convenience:

$$C_{sc} = C_{sc(0)} \left(1 - \frac{V_a}{V_{bi}}\right)^{-w}, \tag{5.1}$$

$$C_d = \frac{\tau_n}{R_d}, \tag{5.2}$$

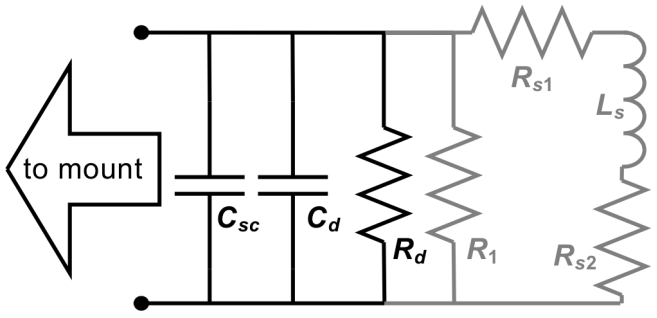

Figure 5.1: Active region elements – low-gain (black) and high-gain (black + gray) operation modes.

$$R_d = \frac{\eta kT}{I_s q} \frac{1}{e^{\left(\frac{qV_a}{\eta kT}\right)}}, \tag{5.3}$$

$$R_1 \approx \frac{R_d}{1 + \tau_n \gamma S_0}, \tag{5.4}$$

$$L_s \approx \frac{R_d \tau_p}{\gamma \tau_n S_0}, \tag{5.5}$$

$$R_{s1} \approx \frac{\varepsilon R_d}{\gamma \tau_n}, \tag{5.6}$$

$$R_{s2} \approx \frac{\beta \Gamma R_d \tau_p I_{tA}}{\alpha \gamma \tau_n S_0^2}. \tag{5.7}$$

As stated before, the SOAs used here are "black-box" devices, i.e., manufacturers do not provide details of their semiconductor structure or fabrication process. Therefore, many of the parameters used during calculations are approximations obtained from literature [23, 24], as listed in Table 5.1. Some parameters may be estimated or measured, like the ideality factor η that is empirically extracted from the current-voltage characteristics of the devices, more specifically from the slope of the I-V curve, which indicate a value of 1.3 for CIP-COC and CIP-NL, and 1.6 for InPhenix. The I-V curves also allow the extraction of the saturation current I_S, by extrapolating the curve in logarithmic scale – indicating a value of 1.5 pA for CIP-COC and CIP-NL, and 150 pA for InPhenix. The voltage V_a varies with the injected current bias, ranging from 0.65 V @1 mA to about 0.8 V @50 mA – affecting R_d, which starts with a high resistance ($\approx$ 80 Ω) at 1 mA and decreases to about 1 Ω at 50 mA.

The calculated values were used as approximated initial parameters for the active region elements. After, these elements were combined to electrical parasitics from mount, and a fine tuning were applied to their values – based on electrical reflection and electro-optical

Table 5.1: Parameters used in calculations.

Variable	CIP-COC	CIP-NL	InPhenix
α (cm^3)	6.4×10^{-35}	6.41×10^{-35}	7.5×10^{-35}
β (%)	0.01	0.01	0.01
Γ	0.4	0.4	0.4
γ ($s^{-1}m^3$)	2.4×10^{-12}	2.4×10^{-12}	2.4×10^{-12}
ε (m^3)	4.5×10^{-23}	4.5×10^{-23}	4.5×10^{-23}
τ_n (ns)	3	3	3
τ_p (ps)	1	1	1
I_L (mA)	15	15	15
k (J/K)	1.38×10^{-23}	1.38×10^{-23}	1.38×10^{-23}
N_{tr} (m^{-3})	1×10^{24}	1×10^{24}	1×10^{24}
q (C)	1.6×10^{-19}	1.6×10^{-19}	1.6×10^{-19}
T (K)	298	298	298

transmission data obtained for the three SOAs, as detailed hereinafter.

5.2 Cascaded parasitic elements

The cascade parasitic elements comprise electrical parasitics from mount, coupling, package, and chip, as illustrated in Fig. 5.2.

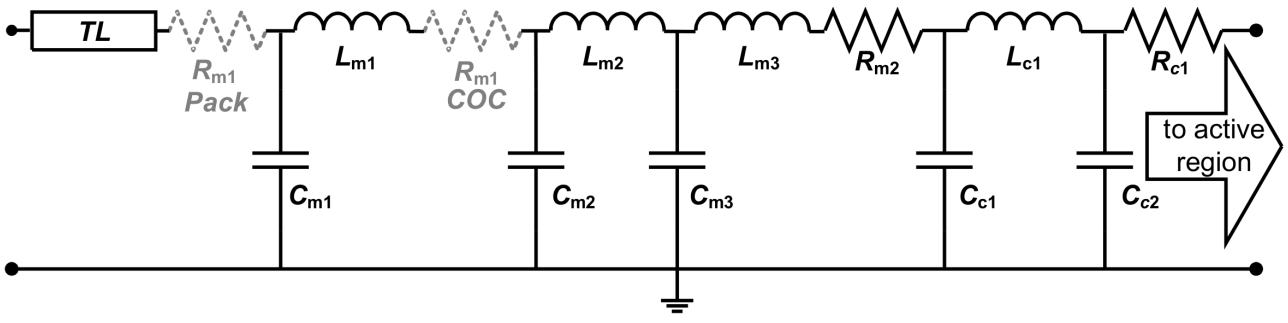

Figure 5.2: Equivalent circuit model with cascaded parasitic elements from mount, coupling and chip.

Such elements are related to the SOAs' physical structures detailed before in Chapter 3 (Fig. 3.2 – page 35, and Fig. 3.4 – page 36). The CIP-COC is connected to a 16-mm long microstrip line (TL) in series with a 47-Ω resistor (R_{m1}-COC) to match the 50-Ω impedance when added to SOA impedance (≈ 3.5 Ω); while the encapsulated SOAs are connected to 40-mm long semi-rigid coaxial cables (TL) and 47 Ω resistors (R_{m1}-$Pack$) mounted on a heat sink. Parasitic elements from bond-wire inductances, small loss resistance and standoff shunt capacitances are modeled respectively by L_{m1} – L_{m3}, R_{m2}, and C_{m1} – C_{m3}.

The elements appearing in the right part of Fig. 5.2 (C_{c1}, C_{c2}, L_{c1}, and R_{c1}) are related to parasitic elements from devices' chip and their origin can be described referring to the EMBH laser structure, as shown in Fig. 5.3: C_{c1} represents the chip effective capacitance distributed across the insulator (1) and the p-region (3), R_{c1} represents the total series resistance from the n-region (2) and from the metal contact (5), the active region and the substrate (4). All parasitic elements described so far do not vary with I-bias, but reflection and transmission measurements (in detail in the next subsections) pointed to the existence of an LC pair depending on I-bias, and so modeled by L_{c1} and C_{c2}. These parasitic elements might be linked to variations in the main path of the injected bias current, passing through the metal contact (5) and p-region (6) until reaching the active region.

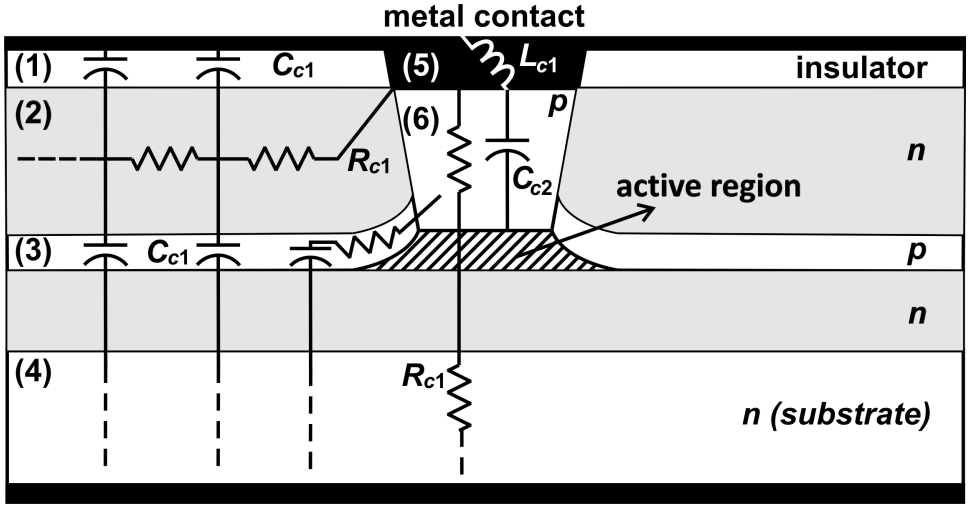

Figure 5.3: Cross-sectional view of an EMBH laser (not to scale – adapted from [24]).

Parameter extraction for all cascaded parasitic elements relied on reflection (impedance) and transmission (electro-optical conversion) measurements for the three SOAs, as presented below.

5.2.1 Reflection measurements

Impedance measurements were simply done by connecting the SOAs (including bias-tee and electrical bias current sources) to a 40 GHz-bandwidth microwave network analyzer (*Agilent N5230C PNA-L*). First, a low inductance gold contact was used to short-circuit the SOAs' electrical inputs, isolating the devices from microwave mounting during the impedance measurements and so enabling the acquisition only of mounting effects, without the SOA. Next, the measurements were repeated including the SOAs and changing the injected bias current (I-bias). Four different I-bias were used: two in low-gain (40 mA and 60 mA), and two in high-gain (80 mA and 100 mA) operation mode. However, the results for 40 mA are not shown here because the experimental data at this I-bias are very noisy, making difficult an accurate extraction of the ECs' parameters.

5.2.2 Transmission measurements

Transmission measurements were carried out by applying sinusoidal waveforms at the SOAs RF inputs and analyzing their electro-optical (EO) response using the experimental setup shown before in Chapter 3 (Fig. 3.6 – page 38) and repeated here (in Fig. 5.4) for convenience.

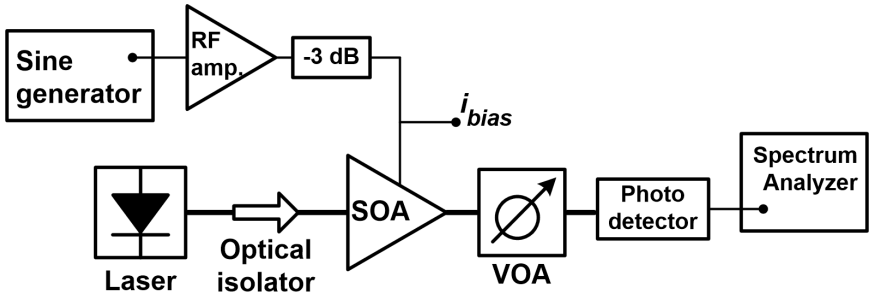

Figure 5.4: Experimental setup for electro-optical conversion analysis.

The signal generator (*Agilent E8257D*, 4 dBm) is connected to an RF amplifier (*SHF810*) and the modulated signal superimposed to the SOA bias current. A continuous wave (CW) tunable laser (@1550 nm, 4 dBm for packaged SOAs and 12 dBm for CIP-COC) is followed by an optical isolator and then coupled to the SOA under test; the optical output is measured by a PIN photodiode (*Discovery Semiconductors – DSC-R410*) after a variable optical attenuator (VOA). The electrical signal feeds the spectrum analyzer (*Agilent E4408B*), where the EO conversion is analyzed as function of bias current, in frequency range of few kHz up to 20 GHz. A program, developed in LabVIEW, automates the signal frequency sweeping and stores data for each frequency on ASCII files, from where the output from the generator is subtracted, therefore considering only the SOAs' response.

5.2.3 Experimental-simulation comparison

Once the experimental data were obtained, the ECs shown before (Fig. 5.1 and Fig. 5.2) were applied in simulations using the *Keysight ADS* software [59]. Experimental results from reflection and transmission measurements were compared to S(1,1) and S(2,1) simulations, respectively. Then, using *ADS* tuning resource, the elements' parameters were fitted in order to find the best matching between experimental and simulation results, as illustrated in Fig. 5.5.

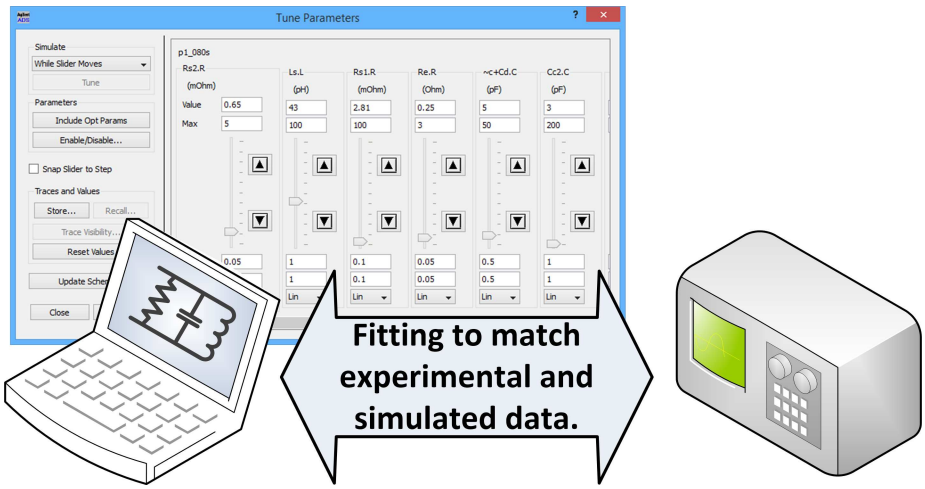

Figure 5.5: *ADS* tuning resource was used to match experimental and simulated results.

The parameters extracted for cascade parameters independent of I-bias are listed in Table 5.2. The values found for the chip elements L_{c1}, C_{c2}, and for active region elements – all dependent on I-bias – are presented in Table 5.3 for selected I-bias values.

The electrical reflection comparisons are shown in Fig. 5.6 and the EO response com-

Table 5.2: Parameters independent of I-bias.

Element	**CIP-COC**	**CIP-NL**	**InPhenix**
$\boldsymbol{C_{m1}}$ **(pF)**	0.25	0.15	0.15
$\boldsymbol{L_{m1}}$ **(nH)**	0.34	6	3.5
$\boldsymbol{C_{m2}}$ **(pF)**	0.81	0.9	3.8
$\boldsymbol{L_{m2}}$ **(nH)**	1.28	0.81	1
$\boldsymbol{C_{m3}}$ **(pF)**	1.2	29	0.2
$\boldsymbol{L_{m3}}$ **(nH)**	2.5	2.1	3.5
$\boldsymbol{R_{m2}}$ **(Ω)**	0.9	0.8	0.8
$\boldsymbol{C_{c1}}$ **(pF)**	30	20	15
$\boldsymbol{R_{c1}}$ **(Ω)**	2.65	2.9	2

Table 5.3: Parameters dependent of I-bias.

	CIP-COC			**CIP-NL**			**InPhenix**		
	60 mA	**80 mA**	**100 mA**	**60 mA**	**80 mA**	**100 mA**	**60 mA**	**80 mA**	**100 mA**
$\boldsymbol{L_{c1}}$ **(nH)**	1	0.15	0.11	1	0.15	0.11	2.5	0.35	0.15
$\boldsymbol{C_{c2}}$ **(pF)**	2	3	5	2	3	5	1.5	2	4
$\boldsymbol{C_{sc} + C_d}$ **(pF)**	2	5	7.5	2	4	7	2.5	4.2	6.5
$\boldsymbol{R_d}$ **(Ω)**	6.5	–	–	3	–	–	5	–	–
$\boldsymbol{R_1}$ **(Ω)**	–	0.25	0.2	–	0.25	0.2	–	0.15	0.11
$\boldsymbol{R_{s1}}$ **(mΩ)**	–	2.81	1.75	–	3	2	–	2.8	2
$\boldsymbol{L_s}$ **(pH)**	–	43	32	–	45	25	–	46	30
$\boldsymbol{R_{s2}}$ **(mΩ)**	–	0.65	0.35	–	0.15	0.1	–	0.13	0.09

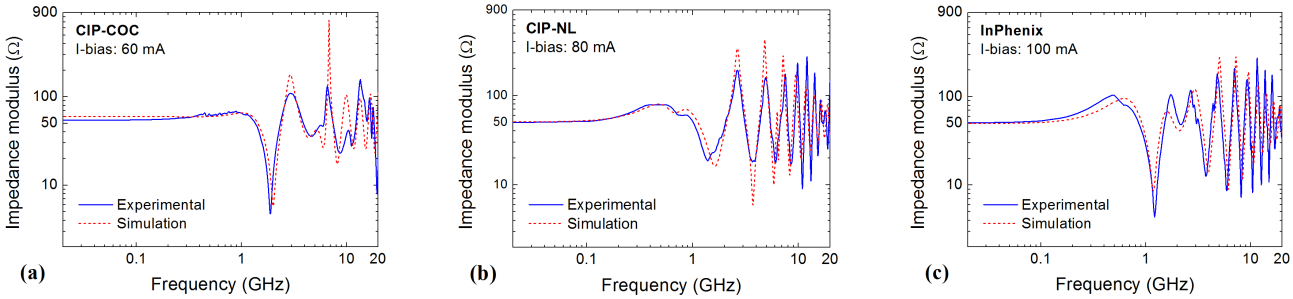

Figure 5.6: Comparison between experimental (solid lines) and numerical (dashed lines) results of electrical reflection for the (a) CIP-COC (60 mA), (b) CIP-NL (80 mA) and (c) InPhenix (100 mA).

parisons are shown in Fig. 5.7. To minimize repetition of graphs, we present the comparative results of one I-bias for each SOA: 60 mA for CIP-COC; 80 mA for CIP-NL, and 100 mA for InPhenix.

Experimental and numerical data show a good agreement up to 7 GHz for the three SOAs, which is reasonable considering that we are using a linear circuit. The obtained models enable the simulation of SOAs' behavior using any circuit analysis' facility. To illustrate, the models are employed in transient simulations and the results are compared with experimental data from SOAs working as high-speed switches, as presented in next section.

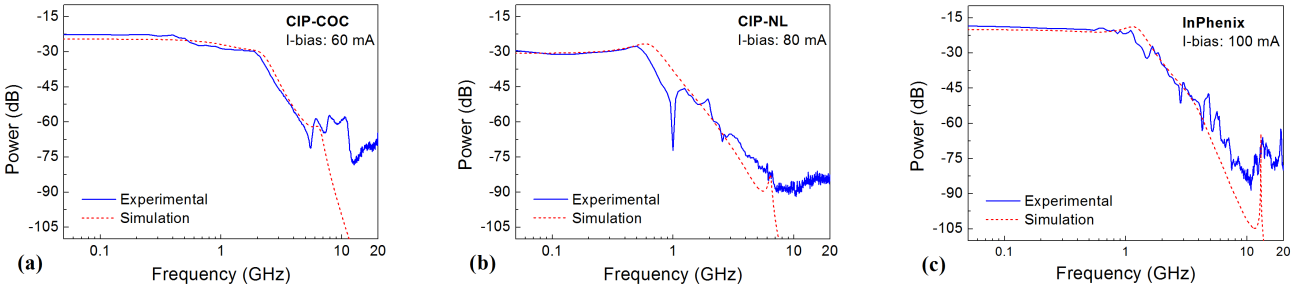

Figure 5.7: Comparison between experimental (solid lines) and numerical (dashed lines) EO response for the (a) CIP-COC (60 mA), (b) CIP-NL (80 mA) and (c) InPhenix (100 mA).

5.3 Transient results

The experimental setup is the same presented before in Chapter 3 (Fig. 3.9 – page 40) and repeated here for convenience (Fig. 5.8).

The RF part of the setup is composed of a pulse generator (*Agilent – J-BERT N4903B*), a microwave combiner (-6 dB), a RF amplifier (*SHF-810*), and RF attenuators to reduce back-and-forth reflections and protect setup's components. The optical part is composed by a continuous-wave (CW) tunable laser (*Santec TSL-210*), the SOA under test, and a variable optical attenuator (VOA) connected to the oscilloscope (*Agilent – 86100C*) optical input.

The optical input power for CIP-COC is +10 dBm, while for the encapsulated SOAs is -5 dBm, in order to compensate larger coupling losses in the chip-on-carrier device. For the three SOAs the optical carrier operates at 1550 nm. The EO switching was performed by modulating the SOAs using fast electrical pulses superposed to the DC I-bias, and the results were presented before in Chapter 3. At first, we select three different amplitudes of steps at different bias currents (60 mA, 80 mA, and 100 mA). Next, we applied the PISIC technique [8], adding a pre-impulse to the previous steps. Pulses were built using independent output channels of the pulse generator, combined by a 50 GHz bandwidth resistive combiner. The pulse formats are described in Table 5.4.

An example of an electrical pulse (*Pulse-B*) is shown in Fig.5.9, with and without PISIC.

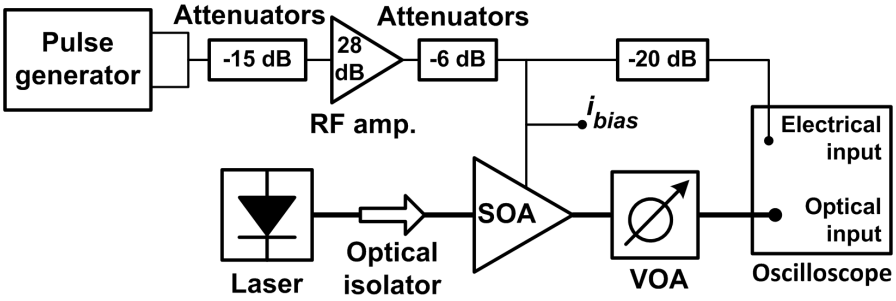

Figure 5.8: Experimental setup for electro-optical switching.

Table 5.4: Pulse formats for the current injection.

	Pulse A	***Pulse B***	***Pulse C***
Step duration	8 ns	8 ns	8 ns
Step amplitude	2.25 V	1.8 V	1.35 V
Step rise time	87 ps	113 ps	121 ps
PISIC duration	0.96 ns	0.64 ns	0.32 ns
PISIC amplitude	0.6 V	0.5 V	0.4 V
PISIC rise time	22 ps	22 ps	22 ps

The experimental optical responses from each SOA were compared to numerical results obtained with ECs in transient response from ADS software. The same electrical pulses used in experiments are applied to the EC and the simulated electrical current through the resistor R_{s2} (or R_d) corresponds to the SOAs' optical output power. Once again, in order to minimize repetition of graphs, selected results are presented for each SOA.

For CIP-COC, *Pulse-A* format results (I-bias: 60 mA) are shown in Fig. 5.10, comparing experimental and numerical data. Experimental rise times are 370 ps without and 186 ps with PISIC, while the simulated results are 207 ps and 156 ps, without/with PISIC respectively.

Results for CIP-NL with *Pulse-B* (80 mA) are shown in Fig. 5.11. Experimental rise

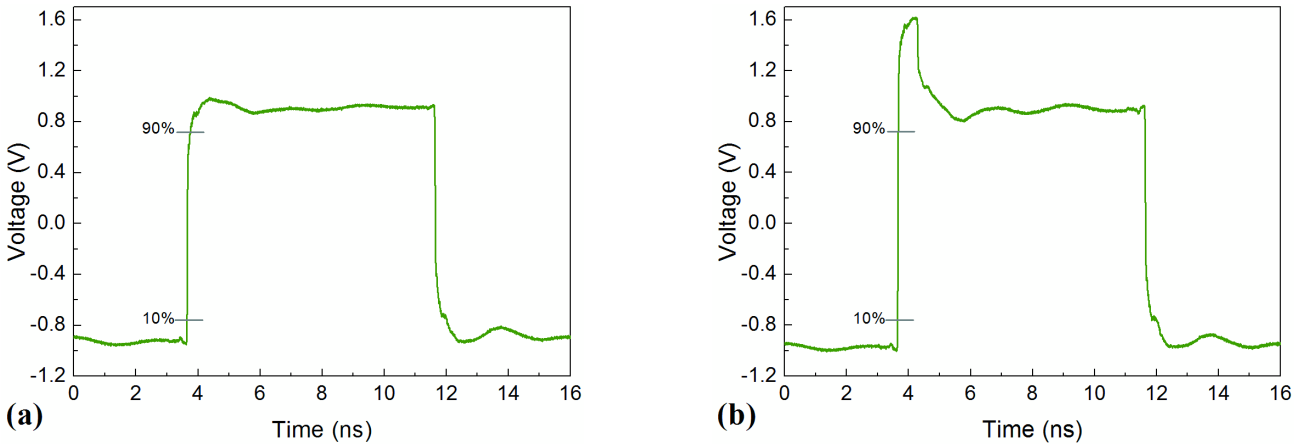

Figure 5.9: Electrical signal for *Pulse-B* extracted from the signal generator, (a) without and (b) with PISIC.

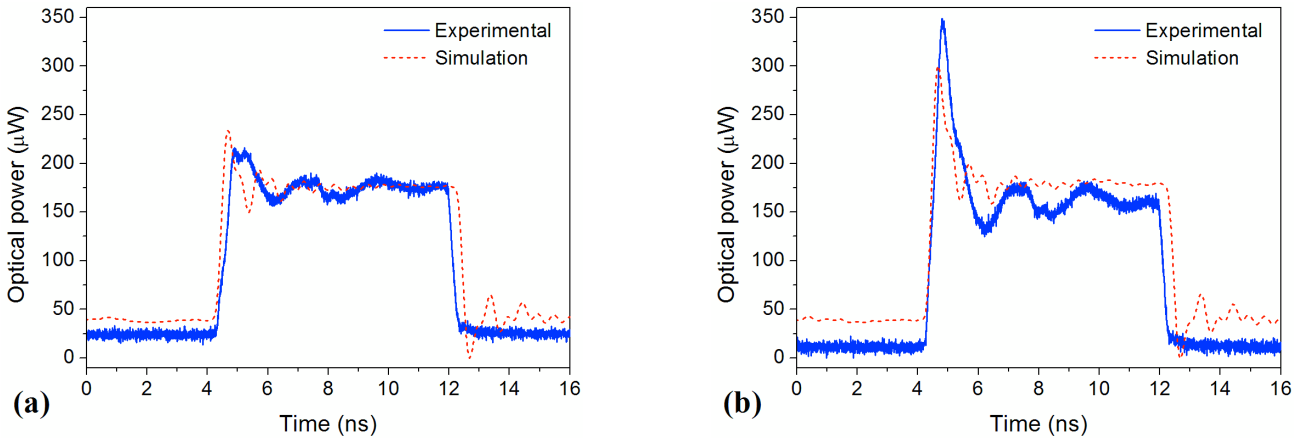

Figure 5.10: Experimental (solid line) and numerical (dashed line) optical response for *Pulse-A*, for CIP-COC, (a) without and (b) with PISIC, I-bias: 60 mA.

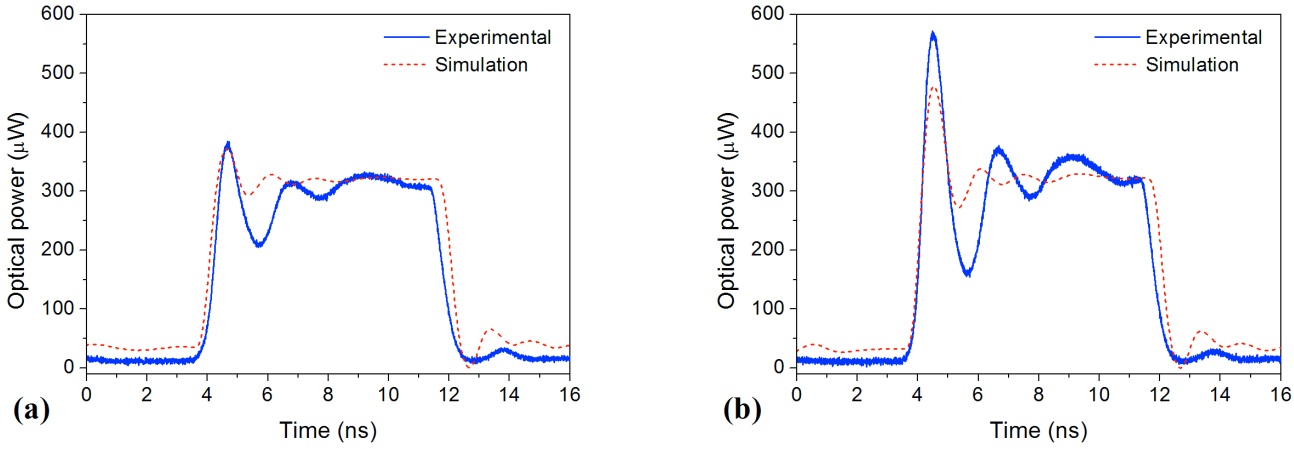

Figure 5.11: Experimental (solid line) and numerical (dashed line) optical response for CIP-NL, (a) without and (b) with PISIC, I-bias: 80 mA.

times are 497 ps and 360 ps, without and with PISIC, respectively, while simulated data were 429 ps and 323 ps.

Results for *Pulse-C* (100 mA) with InPhenix are shown in Fig. 5.12. Simulated results exhibit more pronounced oscillations than the experimental data, but it is possible to see common damped oscillations: 1.15 GHz for experimental and 1.19 GHz for numerical data. For the pulse without PISIC the first oscillation amplitude is lower than the second both for experimental (rise time of 663 ps) and simulated (260 ps) results. For pulse with PISIC the good agreement between experimental (rise time of 357 ps) and simulated (210 ps) remains.

Considering that those steps would provide a high current excursion, the SOA would

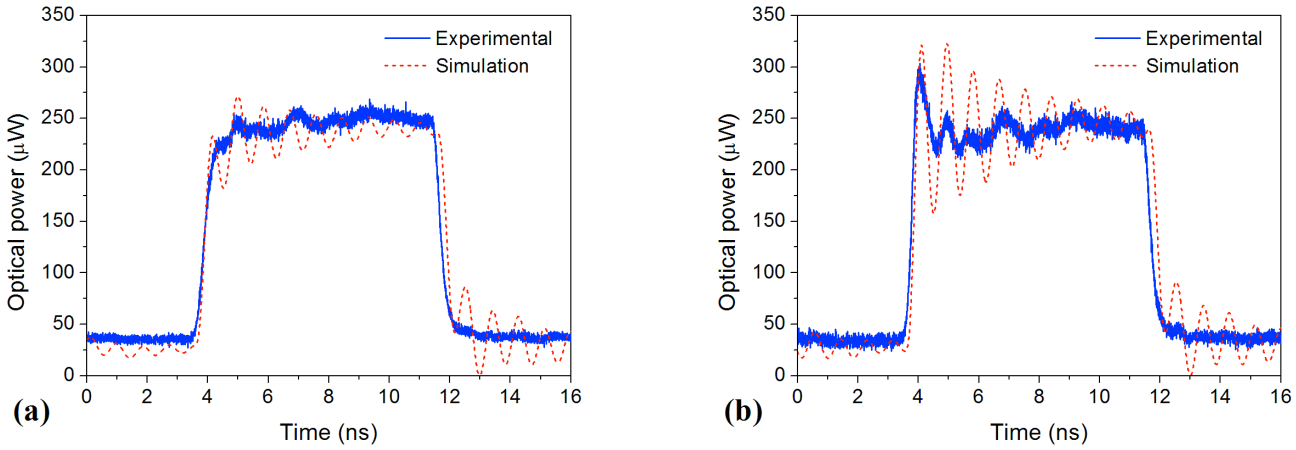

Figure 5.12: Experimental (solid line) and numerical (dashed line) optical response for InPhenix, (a) without and (b) with PISIC, I-bias: 100 mA.

be below transparency to gain saturation during the *off-on* excursion (see Fig. 3.5 – page 38). However, the equivalent circuit model based on small signal analysis cannot predict nonlinear behavior provoked by large signal as those, and the theoretical results are a first approximation. In addition, the InPhenix simulated results predict signal fluctuations with higher amplitude, corresponding to a damped harmonic oscillation around 2 GHz (see Fig. 5.6), related to the SOA relaxation and carrier lifetime. However, the dynamics of SOA switching are complex, and the measured fluctuations after the SOA gain rising have complex shapes and smaller amplitudes.

5.3.1 MISIC simulation

The model was also tested employing the Multi-Impulse Step Injected Current (MISIC) detailed in Chapter 4. Agreement between experimental and numerical data with a precision of 5% in rise times of about 150 ps was achieved, endorsing model validation.

An specific MISIC format (Misic1: 111111, 11010101, 011 011 011...011 – from Table 4.1, page 56) was applied in transient simulations using the EC model described before, using the parameters extracted for CIP-COC. The theoretical results are then compared to experimental data presented before in Chapter 4.

The comparative results are shown in Fig. 5.13, for the PISIC and the MISIC, with

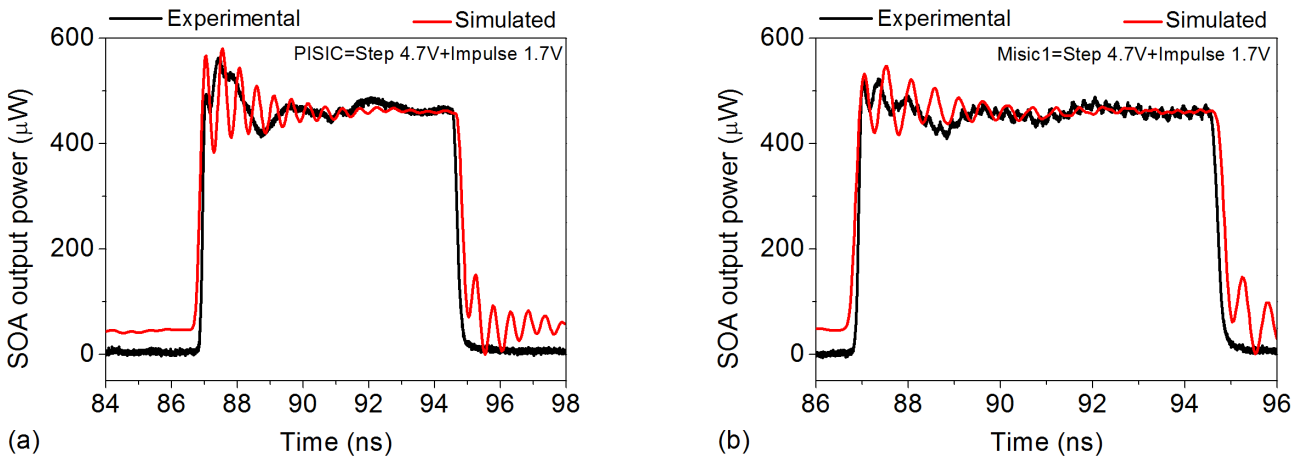

Figure 5.13: Experimental and simulated SOA optical response (I-bias = 80 mA), for impulse of 1.7 V and step of 4.7 V (a) PISIC e (b) Misic1.

step of 4.7 V added to a pre-impulse of 1.7 V, and I-bias of 80 mA. Differently from the previous results, simulations predict a slower rise time of 170 ps in relation to the experiment (115 ps). Besides, the simulated results predict and experiments confirm, the smaller fluctuation for the MISIC signals when compared to PISIC format, confirming that in a first approximation the SOA gain fluctuations can be estimated by simulation.

In order to present a more complete comparison, experimental and simulated results (including step, PISIC, and Misic1) for a pre-impulse of 3.7 V added to a step of 2.7 V with I-bias = 80 mA are shown in Fig. 5.14; and the same comparative for a impulse of 1.7 V added to a step of 4.7 V is illustrated in Fig. 5.15.

The same behavior seen in experimental results is repetead in simulations: reduction of the overshoot by the Misic1 format without worsening the *off-on* switching times.

5.4 Concluding remarks

Equivalent electrical circuits for three different SOAs were presented. The proposed models take into account parasitic elements from substrate and mounting parts. Models were applied to the study of SOA-based fast electro-optical switches, using three pulse formats and

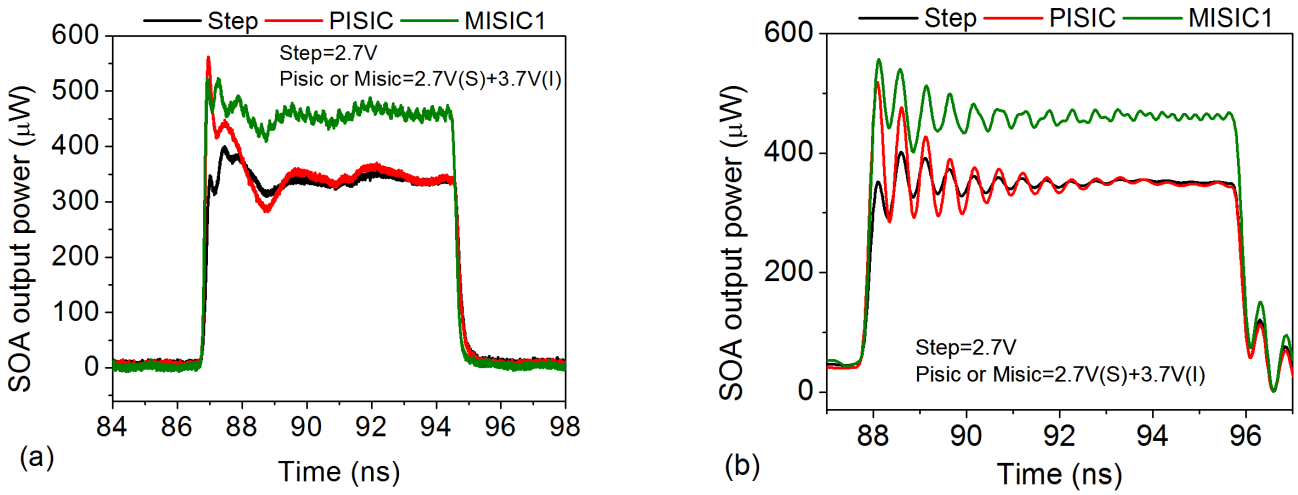

Figure 5.14: (a) Experimental and (b) simulated optical responses for a single step bias current, PISIC, and Misic1 formats (I-bias = 80 mA), for impulse of 3.7 V and step of 2.7 V.

the MISIC technique. Experimental and simulated data present good agreement both for EO response and electrical reflection parameters.

The equivalent circuit analysis may be used in SOAs manufacturing design in order to relate intrinsic SOA parameters with the switching behavior, as well as to study the better pulse formats to be applied in electrical-optical switches based on semiconductor gain media, contributing so to the design of faster SOA-based devices.

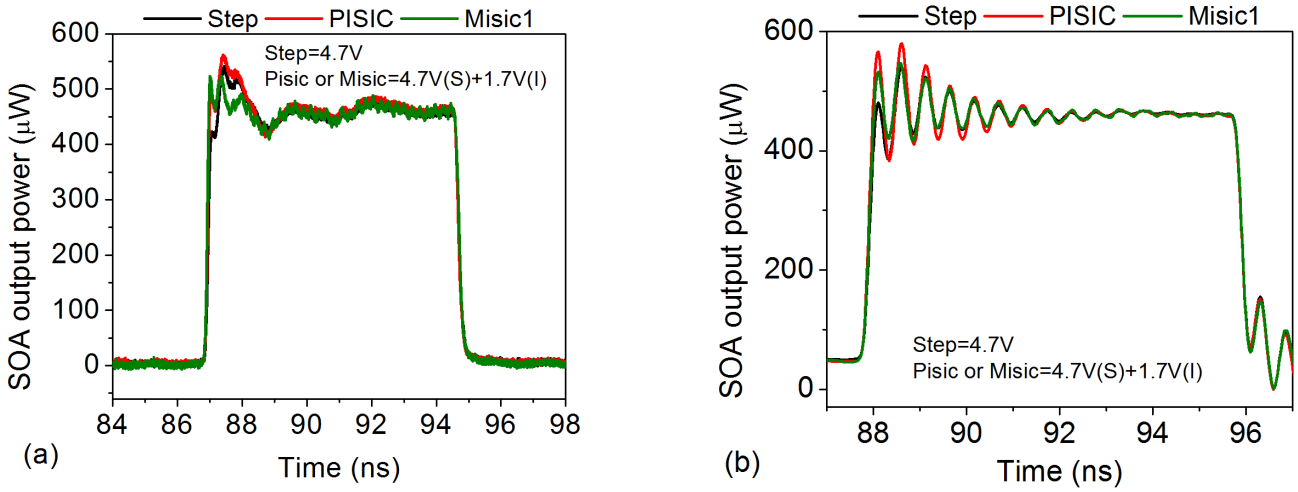

Figure 5.15: (a) Experimental and (b) simulated optical responses for a single step bias current, PISIC, and Misic1 formats (I-bias = 80 mA), for impulse of 1.7 V and step of 4.7 V.

Chapter 6

Conclusions

This thesis presents experiments and simulations in order to propose improvements in electro-optical switching based on SOAs, divided into three main topics:

- Chapter 3 presented a comparison using four dissimilar SOAs, and it showed that devices' geometry affects their responses and choosing the best type of SOA to be used depend on the application. Moreover, the different pulse formats applied to the devices demonstrated the trade-off between rise time and overshoot.

- Chapter 4 presented a new technique (patent pending) to switch the devices using Multi-Impulse Step Injection Current (MISIC). Fast switching with small overshoot and high optical contrast were achieved. Such technique might be employed in optical packet switching or in data centers, for example.

- Chapter 5 shows equivalent electrical circuit modeling for one chip-on-carrier and two butterfly-packaged semiconductor optical amplifiers. The proposed model includes parasitic elements from chip and mounting, and it allows estimation of the electrical current that actually reaches the SOA active region. The RF mounting injection current parameters were heuristically obtained by fitting the model to the experimental data. The active region parameters were analytically obtained as a function of injected bias current, fol-

lowed by a fine-tuning adjustment. Model was illustrated employing the SOAs as fast electro-optical switches; the comparison between experimental and simulated data show good agreement both for transmission and reflection results.

Therefore, the main contributions of this work can be summarized as follows:

1. The main characteristics of electro-optical switches based on four distinct SOAs were identified, and the influence of parasitic elements from device's encapsulation was quantified.

2. *Off-on* switching time of 100 ps was achieved using the SOA chip-on-carrier, with overshoot of 80% and optical contrast of 5 dB.

3. Fast rise time (115 ps) with high optical contrast (30 dB) and low overshoot (less than 30%) were achieved by using the MISIC technique.

4. Equivalent electrical circuits for three different SOAs were designed; and the proposed model can be easily adapted to other devices.

6.1 Future research

Results from this thesis provide insights for further studies that can be conducted by future works, as the possibilities listed below:

- Based on comparative results of switching, it is possible to analyze potential enhancements in SOAs' fabrication, by reducing parasitic elements from the package wires.

- The MISIC technique effects in an optical network can be explored by considering the benefits from low overshoot and high optical contrast versus the increase in power consumption.

- A nonlinear model of the equivalent electrical circuit can be designed, and might achieve greater accuracy in simulated outcomes.

- Improvement in electro-optical switches based on SOAs can be examined using the proposed model, by studying potential mounts with lower power dissipation and optimized pulse formats to switch the devices, for example.

6.2 Publications

List of publications made during the course of doctoral studies as first author or co-author:

Journal articles:

1. **R. C. Figueiredo**, N. S. Ribeiro, A. M. O. Ribeiro, C. M. Gallep, E. Conforti. "Hundred-Picoseconds Electro-Optical Switching with Semiconductor Optical Amplifiers using Multi-Impulse Step Injection Current", *J. Lightw. Technol.*, vol. 33, pp. 69–77, 2014. DOI: 10.1109/JLT.2014.2372893 (*open access*).

2. **R. C. Figueiredo**, N. S. Ribeiro, C. M. Gallep, E. Conforti. "Bias Current Influence on Semiconductor Optical Amplifier's Equivalent Circuit", *Opt. Commun.*, vol. 336, pp. 153–159, 2015.

3. **R. C. Figueiredo**, N. S. Ribeiro, C. M. Gallep, E. Conforti. "Comparison of Electro-Optical Switching Performances of Dissimilar Semiconductor Optical Amplifiers", accepted for publication in *Microw. Opt. Technol. Lett.*, 2015.

Patent requirement and software registration:

1. **R. C. Figueiredo**, N. S. Ribeiro, C. M. Gallep, E. Conforti. "*Método de chaveamento eletro-óptico empregando multi-impulsos e degrau de corrente via amplificadores ópticos a semicondutor, dispositivos para chaveamento eletro-óptico de portadoras ópticas, e uso dos dispositivos*", PCT/BR2012/000469. "Method for electro-optical keying using multiple pulses and current stepping via semiconductor optical amplifiers, devices for electro-optical

keying of optical carriers, and use of the devices", registration number: WO2013142928A1, 2012.

2. **R. C. Figueiredo**, A. M. O. Ribeiro, R. Arthur, E. Conforti. Software "ControleSMS", registration number: BR512014000363-9 at INPI - *Instituto Nacional da Propriedade Industrial*, 2014.

Article submission:

1. **R. C. Figueiredo**, N. S. Ribeiro, C. M. Gallep, E. Conforti. "*Frequency and Time-Domain Simulations of Semiconductor Optical Amplifiers using Equivalent Circuit Modeling*". Journal article submitted for publication.

Book chapter:

1. **R. C. Figueiredo**, A. M. O. Ribeiro, R. Arthur, E. Conforti. "Remote SMS Instrumentation Supervision and Control Using LabVIEW". Practical Applications and Solutions Using LabVIEW^{TM} Software, In-Tech, 2011.

Conference proceedings (international):

1. **R. C. Figueiredo**, N. S. Ribeiro, C. M. Gallep, E. Conforti. "Chip-on-carrier microwave mount for semiconductor optical amplifier measurements". In: 2013 SBMO/IEEE MTTS International Microwave and Optoelectronics Conference (IMOC), 2013, Rio de Janeiro. 2013 SBMO/IEEE MTT-S International Microwave & Optoelectronics Conference (IMOC), 2013. p. 1-3.

2. E. C. Magalhaes, **R. C. Figueiredo**, N. S. Ribeiro, E. Conforti ; A. C. Bordonalli. "System Characterization of a SOA-FWM Wavelength Converter". In: OSA Frontiers in Optics 2011/Laser Science XXVII, 2011, San Jose, California, USA. OSA Frontiers in Optics 2011/Laser Science XXVII Conference Digest, 2011.

3. **R. C. Figueiredo**, .E. C. Magalhaes, N. S. Ribeiro, C. M. Gallep, E. Conforti. "Equivalent Circuit of a Semiconductor Optical Amplifier Chip with the Bias Current Influence". In: Microwave & Optoelectronics Conference (IMOC), 2011 SBMO/IEEE MTT-S International, 2011, Natal, RN, Brasil. Microwave & Optoelectronics Conference (IMOC), 2011 SBMO/IEEE MTT-S International, 2011. p. 852-856.

Conference proceedings (national):

1. **R. C. Figueiredo**, N. S. Ribeiro, A. L. Toazza, C. M. Gallep, E. Conforti. "*Análise da Conversão Eletro-Óptica Harmônica de um Amplificador Óptico a Semicondutor*". In: MOMAG 2014 (16º SBMO Simpósio Brasileiro de Micro-ondas e Optoeletrônica e o 11º CBMag Congresso Brasileiro de Eletromagnetismo), 2014, Curitiba/PR. Anais do MOMAG 2014, 2014. (In portuguese)

2. A. Godoy, E. S. Silva, **R. C. Figueiredo**. "*Efeitos do Estágio Docente na Formação do Pós-Graduando*". In: WEI - XXI Workshop sobre Educação em Computação - Congresso da Sociedade Brasileira de Computação, 2013, Maceió. Anais do XXI Workshop sobre Educação em Computação (CSBC), 2013. p. 551-560. (In portuguese)

3. N. S. Ribeiro, **R. C. Figueiredo**, A. L. Tozza, C. M. Gallep, E. Conforti. "*Simulações com circuito equivalente de SOAs visando à redução do tempo de chaveamento*". In: MOMAG 2012 (15º SBMO Simpósio Brasileiro de Micro-ondas e Optoeletrônica e o 10º CBMag Congresso Brasileiro de Eletromagnetismo), 2012, João Pessoa/PB. Anais do MOMAG 2012, 2012. (In portuguese)

4. **R. C. Figueiredo**, N. S. Ribeiro, C. M. Gallep, E. Conforti. "*Modelagem e Aplicação do Circuito Equivalente de um Amplificador Óptico a Semicondutor*". In: MOMAG 2012 (15º SBMO Simpósio Brasileiro de Micro-ondas e Optoeletrônica e o 10º CBMag Congresso Brasileiro de Eletromagnetismo), 2012, João Pessoa/PB. Anais do MOMAG 2012, 2012. (In portuguese)

References

[1] A. Vahdat, H. Liu, X. Zhao, and C. Johnson, "The Emerging Optical Data Center," in *Optical Fiber Communication Conference/National Fiber Optic Engineers Conference 2011*, (Los Angeles, California), p. OTuH2, OSA, 2011.

[2] C. Kachris and I. Tomkos, "A Survey on Optical Interconnects for Data Centers," *IEEE Communications Surveys & Tutorials*, vol. 14, no. 4, pp. 1021–1036, 2012.

[3] S. Di Lucente, J. Luo, R. P. Centelles, A. Rohit, S. Zou, K. A. Williams, H. J. S. Dorren, and N. Calabretta, "Numerical and experimental study of a high port-density WDM optical packet switch architecture for data centers.," *Optics Express*, vol. 21, pp. 263–269, Jan. 2013.

[4] A. Shacham and K. Bergman, "An Experimental Validation of a Wavelength-Striped, Packet Switched, Optical Interconnection Network," *Journal of Lightwave Technology*, vol. 27, pp. 841–850, Apr. 2009.

[5] D. Brunina and K. Bergman, "An Energy-Efficient Optically Connected Memory Module for Hybrid Packet- and Circuit-Switched Optical Networks," *IEEE Journal of Selected Topics in Quantum Electronics*, vol. 19, p. 3700407, Mar. 2013.

[6] W. Miao, J. Luo, S. Di Lucente, H. Dorren, and N. Calabretta, "Novel flat datacenter network architecture based on scalable and flow-controlled optical switch system.," *Optics Express*, vol. 22, pp. 2465–2472, Feb. 2014.

[7] H. Wang, E. T. Aw, K. A. Williams, A. Wonfor, R. V. Penty, and I. H. White, "Lossless Multistage SOA Switch Fabric Using High Capacity Monolithic 4×4 SOA Circuits," in *Optical Fiber Communication Conference and National Fiber Optic Engineers Conference*, (San Diego, California), p. OWQ2, OSA, 2009.

[8] C. Gallep and E. Conforti, "Reduction of semiconductor optical amplifier switching times by preimpulse step-injected current technique," *IEEE Photonics Technology Letters*, vol. 14, pp. 902–904, July 2002.

[9] M. Ikeda, "Switching characteristics of laser diode switch," *IEEE Journal of Quantum Electronics*, vol. 19, pp. 157–164, Feb. 1983.

[10] E. Conforti and C. Gallep, "A Fast Electro-Optical Amplified Switch using a Resistive Combiner for Multi-Pulse Injection," in *2006 IEEE MTT-S International Microwave Symposium Digest*, pp. 1935–1938, IEEE, 2006.

[11] N. Ribeiro, A. Toazza, C. Gallep, and E. Conforti, "Rise Time and Gain Fluctuations of an Electrooptical Amplified Switch Based on Multipulse Injection in Semiconductor Optical Amplifiers," *IEEE Photonics Technology Letters*, vol. 21, pp. 769–771, June 2009.

[12] V. Francois and F. Laramee, "Multicore Fiber Optimization for Application to Chip-to-Chip Optical Interconnects," *Journal of Lightwave Technology*, vol. 31, pp. 4022–4028, Dec. 2013.

[13] A. R. Totovic, J. V. Crnjanski, M. M. Krstic, and D. M. Gvozdic, "An Efficient Semi-Analytical Method for Modeling of Traveling-Wave and Reflective SOAs," *Journal of Lightwave Technology*, vol. 32, pp. 2106–2112, June 2014.

[14] M. Connelly, "Wideband semiconductor optical amplifier steady-state numerical model," *IEEE Journal of Quantum Electronics*, vol. 37, pp. 439–447, Mar. 2001.

[15] A. Sharaiha and A. Hamie, "Comprehensive Analysis of Two Cascaded Semiconductor Optical Amplifiers for All-Optical Switching Operation," *J. Lightwave Technol.*, vol. 22, no. 3, pp. 850–858, 2004.

[16] W. Mathlouthi, P. Lemieux, M. Salsi, A. Vannucci, A. Bononi, and L. A. Rusch, "Fast and Efficient Dynamic WDM Semiconductor Optical Amplifier Model," *Journal of Lightwave Technology*, vol. 24, pp. 4353–4365, Nov. 2006.

[17] K. Hussain, S. Pratap Singh, and P. Kumar Datta, "Effect of input signal and filter parameters on patterning effect in a semiconductor optical amplifier," *Optics Communications*, vol. 308, pp. 197–203, Nov. 2013.

[18] A. Sharaiha and M. Guegan, "Equivalent circuit model for multi-electrode semiconductor optical amplifiers and analysis of inline photodetection in bidirectional transmissions," *Journal of Lightwave Technology*, vol. 18, pp. 700–707, May 2000.

[19] A. Das Barman, I. Sengupta, and P. K. Basu, "A simple spice model for traveling wave semiconductor laser amplifier," *Microwave and Optical Technology Letters*, vol. 49, pp. 1558–1561, July 2007.

[20] I. Sengupta, A. Das Barman, and P. K. Basu, "Circuit model for analysis of SOA-based photonic switch," *Optical and Quantum Electronics*, vol. 41, pp. 837–848, June 2009.

[21] S. B. Kuntze, B. Zhang, L. Pavel, and J. S. Aitchison, "Impact of Feedback Delay on Closed-Loop Stability in Semiconductor Optical Amplifier Control Circuits," *Journal of Lightwave Technology*, vol. 27, pp. 1095–1107, May 2009.

[22] R. Tucker and D. Pope, "Microwave Circuit Models of Semiconductor Injection Lasers," *IEEE Transactions on Microwave Theory and Techniques*, vol. 31, pp. 289–294, Mar. 1983.

[23] R. Tucker and D. J. Pope, "Circuit modeling of the effect of diffusion on damping in a narrow-stripe semiconductor laser," *IEEE Journal of Quantum Electronics*, vol. 19, pp. 1179–1183, July 1983.

[24] R. Tucker and I. Kaminow, "High-frequency characteristics of directly modulated InGaAsP ridge waveguide and buried heterostructure lasers," *Journal of Lightwave Technology*, vol. 2, pp. 385–393, Aug. 1984.

[25] H. Ghafouri-Shiraz, *The Principles of Semiconductor Laser Diodes and Amplifiers: Analysis and Transmission Line Laser Modeling*. Imperial College Press, 2004.

[26] R. C. Figueiredo, E. C. Magalhaes, N. S. Ribeiro, C. M. Gallep, and E. Conforti, "Equivalent circuit of a semiconductor optical amplifier chip with the bias current influence," in *2011 SBMO/IEEE MTT-S International Microwave and Optoelectronics Conference (IMOC 2011)*, pp. 852–856, IEEE, Oct. 2011.

[27] R. C. Figueiredo, N. S. Ribeiro, C. M. Gallep, and E. Conforti, "Bias current influence on semiconductor optical amplifier's equivalent circuit," *Optics Communications*, vol. 336, pp. 153–159, Feb. 2015.

[28] J. Mørk, M. L. Nielsen, and T. W. Berg, "The Dynamics of Semiconductor Optical Amplifiers: Modeling and Applications," *Optics and Photonics News*, vol. 14, p. 42, July 2003.

[29] R. Ramaswami and K. N. Sivarajan, *Optical Networks: A Practical Pespective*. San Francisco: Morgan Kaufmann Publishers, 2nd ed., 2002.

[30] G. P. Agrawal, *Fiber-Optic Communication Systems*. New York: John Wiley & Sons, 3rd ed., 2002.

[31] G. P. Agrawal and N. K. Dutta, *Semiconductor Lasers*. New York: Van Nostrand Reinold, 2nd ed., 1993.

[32] Nobelprize.org, "The Nobel Prize in Physics 2000," 2014.

[33] G. H. B. Thompson, *Physics of Semiconductor Laser Devices*. John Wiley & Sons, 1st ed., 1980.

[34] L. A. Coldren and S. W. Corzine, *Diode Lasers and Photonic Integrated Circuits*. John Wiley & Sons, 1995.

[35] R. Tucker, "Large-signal switching transients in index-guided semiconductor lasers," *Electronics Letters*, vol. 20, no. 19, pp. 802–803, 1984.

[36] K. Petermann, *Laser Diode Modulation and Noise*. Dordrecht: Springer Netherlands, 1st ed., 1988.

[37] J. Mørk, A. Mecozzi, and G. Eisenstein, "The modulation response of a semiconductor laser amplifier," *IEEE Journal of Selected Topics in Quantum Electronics*, vol. 5, no. 3, pp. 851–860, 1999.

[38] R. Tucker, "High-speed modulation of semiconductor lasers," *Journal of Lightwave Technology*, vol. 3, no. 6, pp. 1180–1192, 1985.

[39] R. S. Tucker, "Circuit model of double-heterojunction laser below threshold," *Solid-State and Electron Devices, IEE Proceedings I*, vol. 128, no. 3, p. 101, 1981.

[40] R. Tucker, "Large-signal circuit model for simulation of injection-laser modulation dynamics," *Solid-State and Electron Devices, IEE Proceedings I*, vol. 128, no. 5, p. 180, 1981.

[41] R. Tucker, J. Wiesenfeld, P. Downey, and J. Bowers, "Limitations on Switching Speed in Wideband Semiconductor Lasers," in *MTT-S International Microwave Symposium Digest*, vol. 86, (Baltimore, MD, USA), pp. 655–657, IEEE, 1986.

[42] S. M. Sze, *Physics of Semiconductor Devices*. John Wiley & Sons, 2nd ed., 1981.

[43] J. P. Colinge and C. A. Colinge, *Physics of Semiconductor Devices*. Boston: Kluwer Academic Publishers, 2002.

[44] D. Sands, *Diode Lasers*. Taylor & Francis, 2004.

[45] P. Van Halen and M. Habib, "A new model for the p-n junction space charge region capacitance," in *Proceedings of the Tenth Biennial University/Government/Industry Microelectronics Symposium*, pp. 126–130, IEEE, 1993.

[46] S. Nakamura, J. Umeda, and O. Nakada, "Response times of light-emitting diodes," *IEEE Transactions on Electron Devices*, vol. 19, pp. 995–997, Aug. 1972.

[47] T. P. Lee, "Effect of Junction Capacitance on the Rise Time of LED's and on the Turn-on Delay of Injection Lasers," *Bell System Technical Journal*, vol. 54, pp. 53–68, Jan. 1975.

[48] M. J. Connelly, *Semiconductor Optical Amplifiers*. Boston: Kluwer Academic Publishers, 2002.

[49] B. Mikkelsen, *Optical amplifiers and their system applications*. Phd thesis, Technical University of Denmark, 1994.

[50] L. Occhi, *Semiconductor optical amplifiers made of ridge waveguide bulk InGaAsP/Inp: experimental characterisation and numerical modelling of gain, phase, and noise*. Phd thesis, Swiss Federal Institute of Technology in Zurich, 2002.

[51] N. K. Dutta and Q. Wang, *Semiconductor Optical Amplifiers*. Singapore: World Scientific Publishing Company, 1st ed., 2006.

[52] G. Agrawal and N. Olsson, "Self-phase modulation and spectral broadening of optical pulses in semiconductor laser amplifiers," *IEEE Journal of Quantum Electronics*, vol. 25, no. 11, pp. 2297–2306, 1989.

[53] R. C. Figueiredo, N. S. Ribeiro, C. M. Gallep, and E. Conforti, "Chip-on-carrier microwave mount for semiconductor optical amplifier measurements," in *2013 SBMO/IEEE MTT-S International Microwave & Optoelectronics Conference (IMOC 2013)*, pp. 1–3, IEEE, Aug. 2013.

[54] H. Ghafouri-Shiraz, *Fundamentals of Laser Diode Amplifiers*. John Wiley & Sons, 1996.

[55] E. Burmeister, D. Blumenthal, and J. Bowers, "A comparison of optical buffering technologies," *Optical Switching and Networking*, vol. 5, pp. 10–18, Mar. 2008.

[56] E. F. Burmeister, J. P. Mack, H. N. Poulsen, J. Klamkin, L. A. Coldren, D. J. Blumenthal, and J. E. Bowers, "SOA gate array recirculating buffer with fiber delay loop," *Optics Express*, vol. 16, no. 12, pp. 8451–8456, 2008.

[57] M. Matsuura, N. Iwatsu, K. Kitamura, and N. Kishi, "Time-Resolved Chirp Properties of SOAs Measured With an Optical Bandpass Filter," *IEEE Photonics Technology Letters*, vol. 20, pp. 2001–2003, Dec. 2008.

[58] R. Bonk, T. Vallaitis, J. Guetlein, C. Meuer, H. Schmeckebier, D. Bimberg, C. Koos, W. Freude, and J. Leuthold, "The Input Power Dynamic Range of a Semiconductor Optical Amplifier and Its Relevance for Access Network Applications," *IEEE Photonics Journal*, vol. 3, pp. 1039–1053, Dec. 2011.

[59] Keysight Technologies, "Advanced Design System (ADS)."